Monitoring Fatigue Cracks in Steel Bridges using Advanced Structural Health Monitoring Technologies

By

Xiangxiong Kong
M.Eng., China Academy of Building Research, 2009
B.Eng., Zhejiang University, 2006

Submitted to the graduate degree program in Civil Engineering and the Graduate Faculty of the University of Kansas in partial fulfillment of the requirements for the degree of Doctor of Philosophy.

_____

Chair: Jian Li

_____

Caroline Bennett

_____

William Collins

_____

Simon Laflamme

_____

Matthew Fadden

_____

Huazhen Fang

Date Defended: 18 July 2018

The dissertation committee for Xiangxiong Kong certifies that this is the approved version of the following dissertation:

Monitoring Fatigue Cracks in Steel Bridges using Advanced Structural Health Monitoring Technologies

_____

Chair: Jian Li

Date Approved:

Abstract

Fatigue cracks that develop in steel highway bridges under repetitive traffic loads are one of the major mechanisms that degrades structural integrity. If bridges are not appropriately inspected and maintained, fatigue cracks can eventually lead to catastrophic failures, in particular for fracture-critical bridges. Despite various levels of success of crack monitoring methods over the past decades in the fields of structural health monitoring (SHM) and non-destructive evaluation (NDE), monitoring fatigue cracks in steel bridges is still challenging due to the complex structural joint layout and unpredictable crack propagation paths. In this dissertation, advanced SHM technologies are proposed for detecting and monitoring fatigue cracks in steel bridges. These technologies are categorized as: 1) a large-area strain sensing technology based on the soft elastomeric capacitor (SEC) sensor; and 2) non-contact vision-based fatigue crack detection approaches. In SEC-based fatigue crack sensing, the research focuses are placed on numerical prediction of the SEC's response under fatigue cracking and experimental validations of sensing algorithms for monitoring fatigue cracks over long-term. In vision-based fatigue crack detection approaches, two novel sensing methodologies are established through feature tracking and image overlapping, respectively. Laboratory test results verified that the proposed approaches can robustly identify the true fatigue crack from many non-crack edges. Overall, the proposed advanced SHM technologies show great promise for fatigue crack damage detection of steel bridges in laboratory configurations, hence form the basis for long-term fatigue sensing solutions in field applications.

Acknowledgments

This dissertation would not have been possible without the support and contributions of many people. Special appreciation is due to my advisor Dr. Jian Li and members of PhD committee including Drs. Caroline Bennett, William Collins, Simon Laflamme, Matthew Fadden, and Huazhen Fang for their willingness to be a part of this research. Several students should be recognized for their variety of supports in helping me complete this research including Danqing Yu, Duncan MacLachlan, Hayder Al-Salih, Sam Tankel, Wenju Xu, Parisa Asadollahi, and Sdiq Anwar Taher at the University of Kansas; Austin Downey, Sari Kharroub, and Hussam Saleem at Iowa State University; and Jong-Hyun Jeong at the University of Arizona. I also want to thank Dr. Hongki Jo at the University of Arizona, Dr. Guanghui (Richard) Wang at the University of Kansas, and Dr. Jian Xu at Wuhan Polytechnic University for their valuable inputs to this research. In addition, I would like to thank technicians Kent Dye, Matt Maksimowicz, and David Woody for their invaluable assistance in the laboratory.

I also want to express gratitude for the funding support provided by the Transportation Pooled Fund Study, TPF-5(328), which includes the following participating state Departments of Transportation (DOTs): Kansas, Iowa, Minnesota, North Carolina, Pennsylvania, Texas, and Oklahoma.

Several chapters of this dissertation were modified from pervious-published journal manuscripts that I co-authored. I want to thank IOP publishing, American Society of Civil Engineers (ASCE), and Wiley for offering permissions to reproduce these manuscripts. As the first and the only student author, I have made major contributions to each of these publications.

Finally, I would like to thank my family members for their unconditional encouragement and support.

Table of Contents

List of Figures

List of Tables

Chapter 1: Introduction

1.1 Fatigue cracks in steel bridges

Fatigue cracks that develop in steel highway bridges under repetitive traffic loads are one of the major mechanisms that degrades structural integrity. Stress concentration due to small defects in material leads to accumulation and nucleation of the defects, which ultimately result in fatigue cracks. Fatigue cracks in their initial phases are usually small in size and hence are difficult to be detected. Moreover, depending on loading conditions and structural layouts, these cracks may develop rapidly and weaken structural integrity (Fisher, 1984). If bridges are not appropriately inspected and maintained, fatigue cracks can eventually lead to catastrophic failures, in particular for fracture-critical bridges (Haghani et al., 2012).

1.2 Challenges for fatigue cracks detection and monitoring

Detecting fatigue cracks at an early stage is critical so that appropriate maintenance actions can be taken. Currently, visual inspection is the most common approach for fatigue inspection in highway bridges in the United Sates (Phares et al., 2001). However, this method is costly, labor intensive, and prone to errors due to the tiny crack sizes and extra low contrast between the crack and its adjacent metallic surface (Zhao and Haldar, 1996). For instance, a study by the Federal Highway Administration (FHWA) reported that only 2 of 49 bridge inspectors across the United States correctly identified fatigue cracks in steel bridges in Virginia and Pennsylvania (Holusha and Chang, 2007). Many advanced crack detection technologies have been proposed for monitoring fatigue crack initiation and/or propagation, including: acoustic emission (Roberts and Talebzadeh, 2003), piezoelectric sensor (Ihn and Chang, 2004), lamb wave (Staszewski et al., 2007), and vibration analysis (Blunt and Keller, 2006). Nevertheless, complex setups, data

processing algorithms, and noise sensitivity are among the challenges associated with use of these methods.

1.3 Research objectives

The overall objectives of research work in this dissertation are to apply advanced structural health monitoring (SHM) technologies for detecting and monitoring fatigue cracks in steel bridges. In particular, these technologies are categorized as: 1) a large-area strain sensing technology based on the soft elastomeric capacitor sensor; and 2) non-contact vision-based fatigue crack detection approaches.

1.3.1 Soft elastomeric capacitor

The soft elastomeric capacitor (SEC) sensor is a highly scalable sensor due to its ease of fabrication and low cost materials. It is also highly stretchable, enabling a wide strain measurement range; the linearity of the SEC signal has been demonstrated for up to 20% strain (Laflamme et al., 2013). The SEC technology has been engineered to be deployed in sensing skin-type configurations. Analogous to biological skin, it would be able to measure local strain over a mesoscale area. In this dissertation, the SEC is equipped to multiple specimens for evaluating its capability of fatigue crack monitoring including: small-scale compact, C(T), specimen and large-scale bridge girder to cross frame specimen. The research focuses are placed on a finite element (FE) analysis to simulate SEC's response under fatigue cracking numerically, experimental validations of a single SEC's crack sensing ability under different fatigue loading characteristics, and experimental investigation of fatigue damage detection over a large fatigue-susceptible region through an SEC array.

1.3.2 Non-contact vision-based fatigue crack detection approaches

Two novel vision-based approaches are proposed for fatigue crack detection in this dissertation. The first approach can track the surface motion of a crack-prone area in a video stream, and detect fatigue cracks by identifying discontinuities induced by the opening and closing of fatigue cracks under repetitive service loads. The second approach is based on image overlapping technologies to compare, enhance, and visualize the differential image features caused by crack breathing behavior. The effectiveness of these two approaches have been validated through two experiment setups: 1) a steel C(T) specimen with an in-plane fatigue crack; and 2) a bridge girder to cross frame connection subjected to a distortion-induced out-of-plane fatigue crack. Results indicate that the proposed approaches can robustly identify the fatigue crack with high reliability, even when the true crack is surrounded by other non-crack edges.

1.4 Organization of the dissertation

This dissertation is organized in the following order: chapter 2 provides a literature review; chapter 3 investigates a numerical approach to simulate SEC's response under fatigue cracking; chapter 4 illustrates and experimentally validates a crack monitoring algorithm for monitoring fatigue crack growth through small-scale C(T) specimens; chapter 5 further investigates the SEC-based crack detection in the context of a large-scale bridge girder to cross frame connection; chapter 6 and chapter 7 demonstrate two non-contact vision-based fatigue crack detection methods based on video feature tracking and image overlapping, respectively; chapter 8 concludes the dissertation.

Chapter 2: Literature Review

2.1 Fatigue inspection of steel bridges in the United States

Civil infrastructures are critical for maintaining vital societal functions. Many old bridges in the United States are prone to structural damage due to carrying significant amount of service loads over long periods of time. According to the recent infrastructure report (ASCE, 2017) issued by the American Society of Civil Engineers (ASCE) in early 2017, the overall score for American bridges is a C+ with over 9% of the nation's bridges rated structurally deficient. These bridges require significant investments in maintenance, rehabilitation, or replacement. Otherwise, structural damage (e.g. cracks, corrosion, or excessive deformation) in critical structural members could impair structural integrity and lead to catastrophic failures (Biezma and Schanack, 2007).

Among the various damage mechanisms in steel bridges, fatigue cracks are extremely common (Fisher, 1984). In the United States, the dominant type of cracking in steel bridges is called distortion-induced fatigue cracks, which are caused by out-of-plane loading in the web gap region under differential movement between adjacent girders (Connor and Fisher, 2006). Due to the lack of consideration in early bridge design specifications, distortion-induced fatigue cracks are a common issue in many steel bridges built prior to the mid-1980s in the United States (Zhao and Roddis, 2004).

Bridge owners, such as state departments of transportation (DOTs) in the United States, typically rely on trained bridge inspectors to visually inspect steel bridges for fatigue cracking (FHWA, 2004) so that appropriate repairs can be applied before cracks reach critical sizes. However, visual inspections can be prone to error due to inconsistent skills and interpretation of results among inspectors (Zhao and Haldar, 1996). For instance, a study performed by the

Federal Highway Administration (FHWA) reported that only 2 out of 49 bridge inspectors across the United States correctly identified fatigue cracks in steel bridges in Virginia and Pennsylvania (Holusha and Chang, 2007).

Advanced approaches for detecting and/or monitoring of fatigue cracks have been investigated in both the structural health monitoring (SHM) and nondestructive testing (NDT) communities. As a result, both the accuracy and robustness of crack detection can be improved by using sensing technologies. In the context of distortion-induced fatigue crack detection, Yu et al. (2013) reported an acoustic emission approach for identifying fatigue damage at the fillet weld in representative cruciform joints of steel bridges; and Alavi et al. (2017) demonstrated a self-powered sensing approach based on a piezo-floating-gate (PFG) sensor for detecting distortion-induced fatigue cracks. An important challenge with these methods is their reliance on extensive human operations to collect critical measurements (acoustic emission data, voltage, or digital videos) in the field, making it challenging to implement long-term continuous crack monitoring of steel bridges.

2.2 Strain-based fatigue sensing technologies

Direct strain sensing technologies has the potential to be very effective for crack detection since crack opening leads to abrupt strain change in the localized area. For this reason, both traditional metal foil gages (Tikka et al., 2003) and fiber optic sensors (Glisic and Inaudi, 2011) have been evaluated for crack detection. One general agreement is that cracks can be effectively detected using direct strain measurement if they are in direct contact with or close proximity to the sensor. Since the location of fatigue cracks are not known as *a priori*, to effectively detect cracks, a large number of foil gages would be needed. Fiber optic sensors are able to monitor strain over a long distance, but may still be limited considering cracks can occur randomly over a large two-

dimensional surface. In addition, the limited ductility of the sensing materials leads to breakage of the sensors under cracking, which prevents monitoring of further crack activities.

In the context of fatigue crack detection in steel bridges, Ghahremani et al. (2013) adopted strain gauge measurements on a large-scale bridge girder to evaluate the depth characteristics of distortion-induced fatigue cracks, and Bennett et al. (2014) successfully used strain gages to detect the initiation of distortion-induced fatigue cracks in a test of a scaled bridge. However, a general limitation of traditional metal foil strain gauges is their relatively small footprint, making them less cost-effective when attempting to monitor fatigue damage over a large structural surface.

Recently, novel strain sensors which measure strains over a large area have shown their potential in crack detection. These sensors, often referred to as sensing skins, share one common feature of large size but operate under a wide variety of principles. Examples include carbon nanotube based sensors (Loh et al., 2008; Dai et al., 2015), resistive sensor sheets (Yao and Glisic, 2015), printable conductive polymer (Loh et al., 2007), patch antenna sensors (Mohammad and Huang, 2010; Yi et al., 2013), and soft elastomeric capacitive (SEC) sensors (Laflamme et al., 2014; Laflamme et al., 2012).

In particular, the SEC sensor is a highly scalable sensor due to its ease of fabrication and low cost materials. It is also highly stretchable, enabling a wide strain measurement range; the linearity of the SEC signal has been demonstrated for up to 20% strain (Laflamme et al., 2013). Additionally, SECs are mechanically robust, making them suitable for long-term monitoring. Prior studies have demonstrated that SECs are able to monitor static (Laflamme et al., 2012) and dynamic (Saleem et al., 2015) strain in various civil structural components and can monitor strain maps under in-plane stress conditions (Downey et al., 2016).

2.3 Vision-based fatigue sensing technologies

2.3.1 Vision-based structural health monitoring

Computer vision-based technologies have received significant attention in the SHM community due to the benefits of being low-cost, easy-to-deploy, and contactless. Several vision-based approaches have been reported for monitoring health conditions of civil structures at both global and local scales. Some of the recent applications of vision-based SHM include: structural system identification (Yang et al., 2017; Chen et al., 2015; Khuc and Catbas, 2017), displacement monitoring (Feng and Feng, 2016; Abdelbarr et al. 2017), post-disaster structural classification (Yeum and Dyke, 2018), damage detection (Cha et al., 2017; Kong and Li, 2018a; 2018d), and fatigue crack identification (Yeum and Dyke, 2015). Furthermore, when equipped with autonomous platforms such as unmanned aerial vehicles (UAV), vision-based SHM could bring higher flexibility and cost-effectiveness to structural inspection. Recently, UAVs have been applied in structural system identification (Yoon et al., 2017), structural inspection of buildings (Kim et al., 2017), water treatment plants (Ong et al., 2017), bridges (Escobar-Wolf et al., 2017), and so forth. A state-of-the-art review of vision-based SHM in civil structures can be found in (Xu, Y and Brownjohn, 2017).

2.3.2 Vision-based crack detection methods

Computer vision-based crack detection methods have shown great potential over the past decades as a contactless, easy-to-deploy, and low-cost sensing method. In particular, image processing technique (IPT) is the most common approach, since it can efficiently search localized edge features of a crack in an image. Some early IPT-based methods include edge detection (Abdel-Qader et al., 2003), image segmentation (Iyer and Sinha, 2006), percolation processing (Yamaguchi et al., 2008), sequential image filtering (Nishikawa et al., 2012), and so

forth. However, these methods mainly rely on finding the edge features of a crack, hence it could be challenging to distinguish true cracks from crack-like edges such as structural boundaries, wires, or corrosion marks (Yeum and Dyke, 2015).

To address these challenges, advanced IPT-based methods have been developed for extracting additional features of cracks beyond the edge feature. Mokhtari et al. (2017) proposed a statistical approach based on multiple features of cracks including crack length, width, orientation, and so forth, enabling a more robust identification of pavement cracks. Jahanshahi and Masri (2012) applied a 3D reconstruction technology to create a 3D point cloud of a concrete crack to extract the crack penetration depth. Yeum and Dyke (2015) proposed an automated vision-based approach using prior knowledge of approximate crack locations to eliminate unnecessary crack-like edges from images of a steel girder so that true fatigue cracks can be identified. Nevertheless, false positive detection results may still exist in these studies. For example, Yeum and Dyke (2015) reported a false positive result in distinguishing a true fatigue crack from a crack-like edge on the surface of a steel girder scratched by a machine tool.

2.3.3 Vision-based fatigue crack detection methods

One of the early studies on vision-based fatigue crack detection was performed by Yeum and Dyke (2015). In this study, an effective crack detection methodology was established using the prior knowledge about approximate locations of the cracks. As a result, unnecessary non-crack edges can be successfully eliminated in images of a steel girder so that true fatigue cracks can be identified. However, the proposed method was only suitable for a particular type of fatigue cracks that were initiated around the structural bolts. The crack detection ability for other types of fatigue cracks remains unknown.

Later on, Chen et al. (2017) established a comprehensive metallic crack detection approach based on local binary patterns (LBP), support vector machine (SVM), and Bayesian decision theory. Such an approach was further enhanced and validated for detecting cracks in a nuclear power plant (Chen and Jahanshahi, 2017). Xu et al. (2018) proposed a deep learning-based fatigue crack detection framework, which can accurately detect the fatigue cracks, handwriting, and background (i.e. non-crack region) from the digital images in a steel box girder bridge. Nevertheless, a large amount of input images would be needed in these methods for training the classifier. In addition, prior human knowledge about the crack definition is required for labeling small image patches as crack or non-crack regions. The human labeling work is labor intensive and prone to error as sometimes the true fatigue crack is even difficult to be identified by human eyes due to extra low contrast on the metallic surface.

One commonality of the above work is only static features of the crack were utilized. For metallic fatigue cracks in civil infrastructures, they are subjected to tiny cyclic movement perpendicular to the crack length under repetitive service load. Such a movement pattern, termed crack opening or crack breathing, is a driven source for fatigue crack propagation, offering more robust strategies for crack identification. For example, Patel and Darpe (2008) reported that crack breathing in a rotor can induce nonlinear dynamic behavior, serving as a good approach for crack detection. Similarly, Chondros et al. (2001) investigated the crack breathing behavior of a simply supported beam. Results indicated that the natural frequency changes due to crack breathing could potentially be applied for crack identification.

Crack breathing is also a great candidate in the context of vision-based fatigue crack detection. For instance, digital image correlation (DIC) technologies have been widely applied for fatigue crack detection by tracking the discontinuous displacement filed caused by crack

breathing. Despite their high detection accuracies, DIC-based approaches usually require expensive equipment (e.g. macro lens (Rupil et al., 2011), microscopes (Polák et al., 2005), and special light sources (Vanlanduit et al., 2009; Man and Chang, 2016), or surface treatment prior to tests (Hutt and Cawley, 2009; Dias-da-Costa et al., 2016). These extra requirements would limit their capabilities for cost-effective sensing of a large number of fatigue-susceptible regions in civil infrastructures.

Chapter 3: Numerical Simulation of Soft Elastomeric Capacitors under Fatigue Cracking

This chapter is modified based on the following journal publication:

Kong, X., Li, J., Bennett, C., Collins, W., & Laflamme, S. (2016). Numerical simulation and experimental validation of a large-area capacitive strain sensor for fatigue crack monitoring. *Measurement Science and Technology*, 27(12), 124009.

3.1 Overview

In order to deploy soft elastomeric capacitor (SEC) in steel bridges for monitoring of fatigue cracks, it is critical to develop numerical models capable of linking the sensor's signal to fatigue crack geometry. This would directly map a sensor network's response to a damage quantification, which information could easily be interpreted by infrastructure operators and managers to conduct condition-based maintenance procedures. Such numerical models could also be used in the design of a dense sensor network of SECs or similar skin-type sensors for the selection and placement of different sensor geometries throughout the network. In this chapter, a numerical method based on finite element (FE) analysis is developed to simulate the SEC's capacitance response under fatigue cracks. An element removal technique in conjunction with a damage evolution model is adopted to simulate fatigue crack propagation in structural components. The SEC sensor is not explicitly included in the FE model. Instead, the FE model of the structural component is meshed in a way such that the deformation of the SEC sensor can be obtained directly from the FE model. A numerical algorithm is proposed to convert the deformation into capacitance response of the SEC sensor. The proposed numerical method is then validated based

on experimental data from a C(T) specimen. Finally, a parametric study is performed to investigate the effect of changing the size of SEC sensor on its ability to detect fatigue cracks. The main contribution of this chapter is the efficient and reliable numerical method for investigating the SEC sensor's performance under fatigue cracks generated under different structural configurations, boundary conditions, and loading conditions. The proposed method extends to other measurement devices of similar sensing principle.

3.2 Soft elastomeric capacitor

This section provides a brief background on the SEC technology. Its sensing principle is first described, followed by the presentation of typical results on its fatigue crack sensing capability. These results will later be used in the development of the numerical model.

3.2.1 Sensing principle

The SEC sensor is a flexible capacitor transducing a material elongation into a measurement change in capacitance. A detailed description on the sensor's fabrication procedure can be found in Laflamme et al. (2013). Briefly, its dielectric is composed of a styrene-ethylene/butylene-styrene (SEBS) block co-polymer filled with titania, and is sandwiched between two conductive plates fabricated from SEBS filled with carbon black (Figure 1). The SEC sensor can be fabricated with different sizes. In this chapter, the sensor dimension is 76 mm by 76 mm (3 in by 3 in), with the effective sensing area 63.5 mm by 63.5 mm (2.5 in by 2.5 in). Figure 1(c) is a picture of the SEC sensor used in this chapter, in which two copper tapes are embedded in the top and bottom electrodes (conductive plates) for connecting to the data acquisition system.

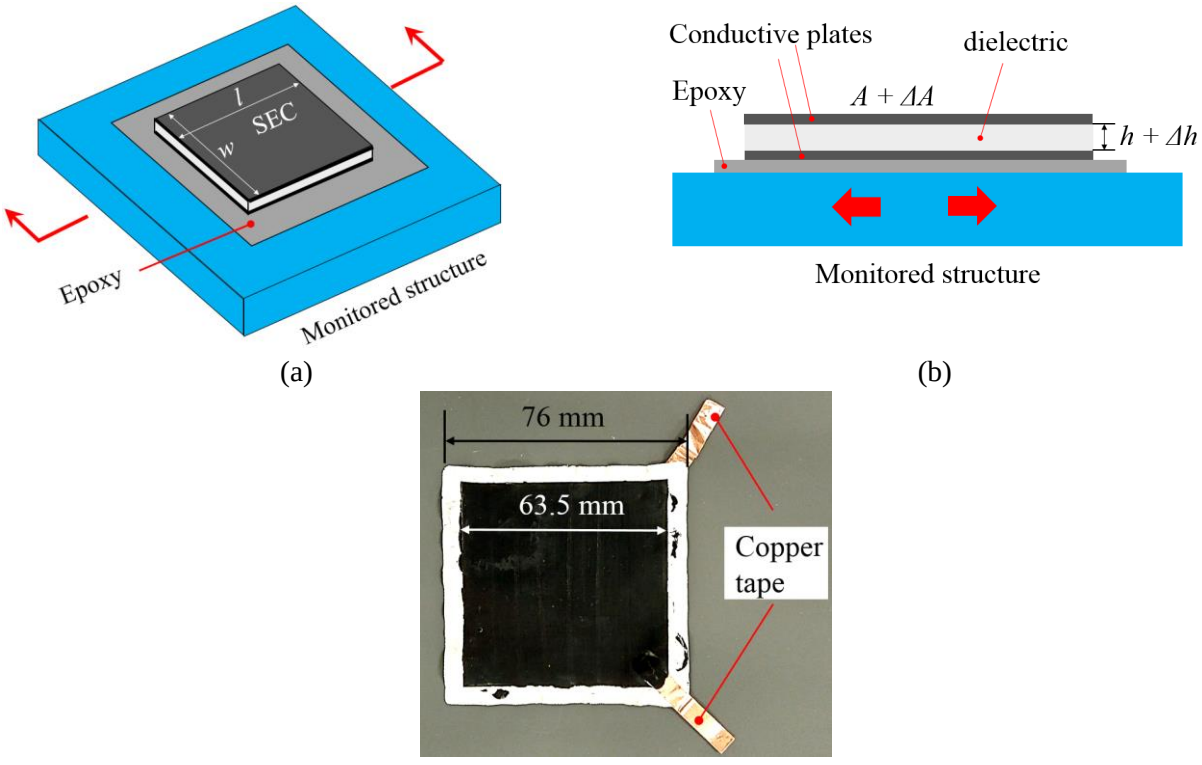

Figure 1. (a) Schematic of the SEC sensor; (b) SEC sensor under a tensile strain; and (c) a picture of the SEC sensor

The SEC can be attached to a structural surface using bonding agents such as epoxy. As illustrated in Figure 1(b), when the structure deforms, the surface strain provokes a change in the SEC's geometry by altering its area A and thickness h. This change in geometry yields a change in the sensor's capacitance C

$$C = \frac{e_0 e_r A}{h} \tag{1}$$

where e_0 is the permittivity of air, e_r is the permittivity of the dielectric, $A = w \cdot l$ is the sensing area of width w and length l, and h is the thickness of the dielectric.

3.2.2 Experimental validation for crack detection

Previously, the SEC sensor has been verified for fatigue crack detection through experimental tests of C(T) specimens (Kharroub et al., 2015; Kong et al., 2015a; 2015b; 2016b). The C(T) specimens were made by A36 steel with a thickness of 6.35 mm. The dimensions of the

specimen are shown in Figure 2(a). To generate a fatigue crack, the specimen was connected to a pair of clevises which were mounted to a uniaxial load frame (Figure 2b). One SEC sensor was attached to one side of the specimen by epoxy, as shown in Figure 2(c). A commercial off-the-shelf data acquisition board (ACAM Pcap02) was connected to the top and bottom plates of the sensor to measure capacitance change of the sensor. A 2 Hz cyclic load with a constant load range from 2.89 kN (0.65 kip) to 28.9 kN (6.5 kip) was applied to the specimen. Capacitance measurements were sampled at 25 Hz.

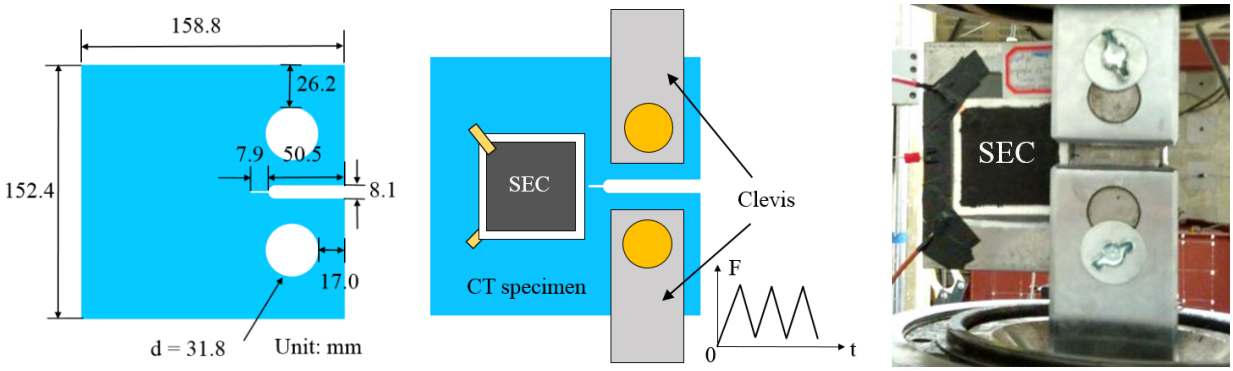

(a) (b) (c)

Figure 2. (a) Dimensions of the C(T) specimen; (b) schematic of test setup; and (c) picture of the test setup

Figure 3(a) shows a crack generated during the test. Figure 3(b) shows the sensor's response in terms of the peak-to-peak percentage change of capacitance ($PP\ C/C_0$), corresponding to different crack lengths with 1.59 mm (1/16 in.) increments. The crack length is taken as the distance measured between the tip of the crack and the edge of the sensing area, as illustrated in Figure 4. This distance reflects the length of the crack covered by the sensing area, which is about 7.9 mm (5/16 in) away from the notch of the specimen. The peak-to-peak amplitude is selected because it provides a more robust measure of capacitance change over long-term monitoring, since the absolute capacitance of the SEC sensor may be subject to drift

due to humidity and temperature changes. The result indicates that the SEC sensor is capable of detecting crack growth by showing an increasing change in *PP C/C₀* with increasing crack length.

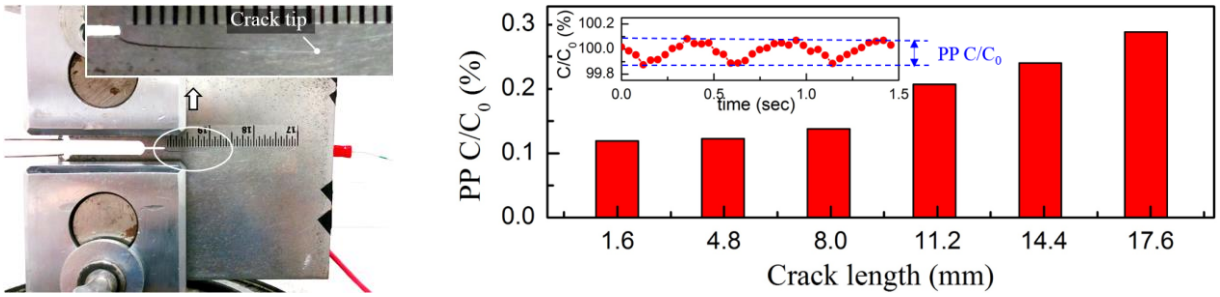

(a) (b)

Figure 3. (a) Crack growth in the C(T) specimen; and (b) percentage change of capacitance versus crack length

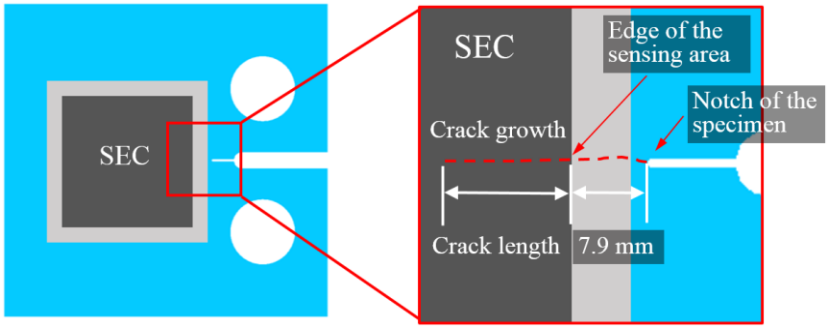

Figure 4. Illustration of crack length definition

3.3. Methodology for numerical simulation

This section presents the methodology used for the numerical simulations. First, the numerical approach is described. It is followed by a description of the procedure used in simulating crack growth. Lastly, the model of the SEC's electrical response is derived.

3.3.1 Numerical approach

Figure 5 illustrates the overall procedure of the proposed numerical method using a C(T) specimen as an example. A four-step procedure is established: 1) identify crack-prone region of the structural member to determine the location for the SEC sensor; 2) create an FE model of the structural member to simulate the crack growth based on the element deletion method discussed in Section 3.3.2 and collect deformation results from the analysis of all elements within the

location of the sensor; 4) compute the capacitance response of the SEC using the algorithm derived in Section 3.3.3. With this procedure, the SEC sensor is assumed to be perfectly bonded to the structure, and its deformation taken as identical to the deformation of the structural member. The proposed numerical method is not limited to small scale C(T) specimens. It can be implemented on more complex structures of different scales, geometric configurations, and boundary conditions.

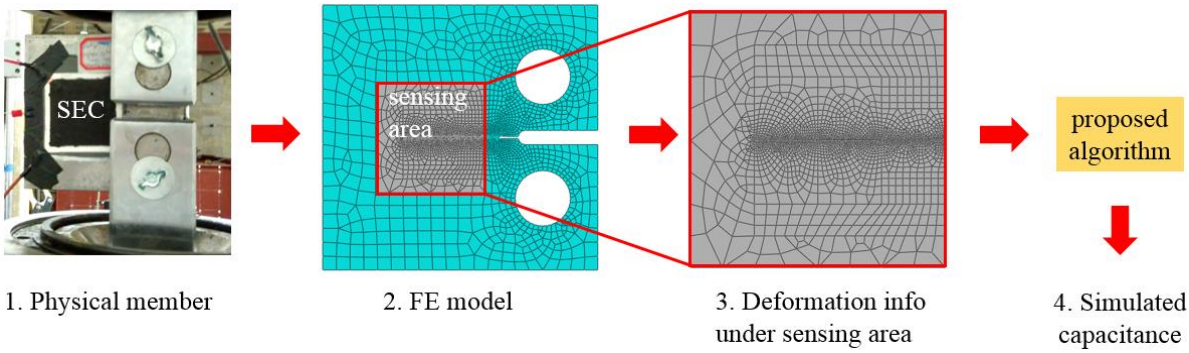

Figure 5. Procedure of the numerical approach

3.3.2 Crack growth simulation

In this chapter, finite element software package Abaqus 6.13 (Dassault Systems, 2013) is selected to simulate crack growth. In particular, the element deletion method is adopted to generate cracks in the model, which requires a damage evolution law defined in the material property so that the elements can accumulate damage and be removed from the model once they reach failure point. Several case studies in the literature indicate that the element deletion method can be applied in various applications such as the prediction of crack growth in structural components (Song et al., 2008; Simonsen and Törnqvist, 2014), simulation of metal cutting process (Movahhedy et al., 2000) and progressive collapse of building structures (Bao et al., 2008; Kong et al., 2014) and so on.

The principle of the element deletion method is illustrated in Figure 6. The material is initially defined as a bilinear model. Then, a damage evolution mechanism is added to the model

by defining an initial damage point and a failure point. Under such a damage mechanism, the element starts to accumulate damage once it passes the initial damage point, and it becomes completed damaged after reaching the failure point. Then, the failure elements are completely deleted by the Abaqus program automatically using an element removal technique. By continuously removing the damaged elements, crack propagation can be numerically simulated, as shown in Figure 6(b).

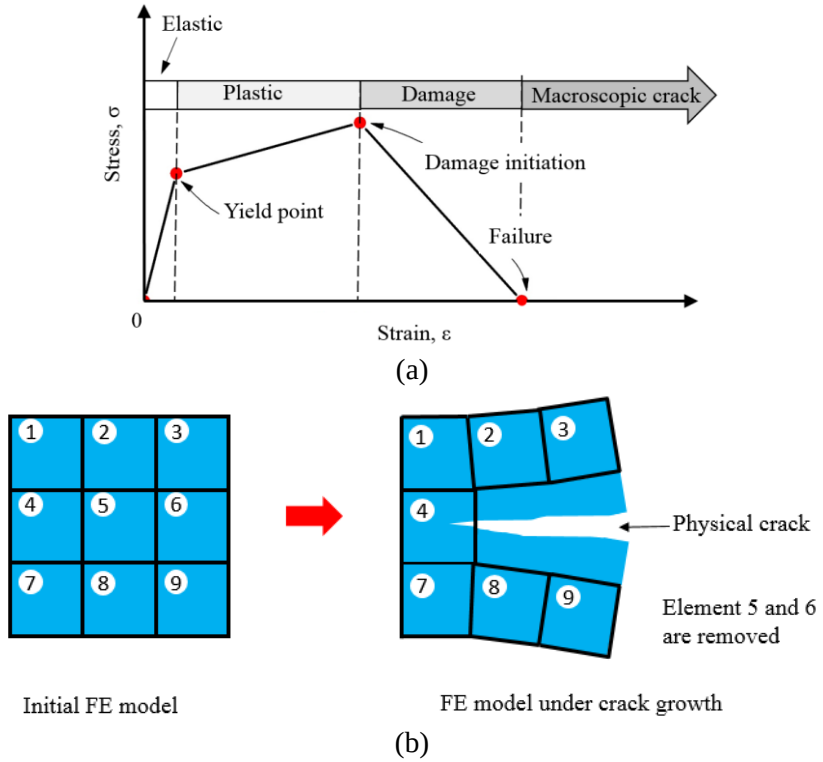

Figure 6. Crack simulation through the element deletion method: (a) damage evolution model; and (b) simulation of crack growth by deleting elements where each numbered square is an element

3.3.3 Proposed algorithm for capacitance calculation

An algorithm is required to convert FE analysis results into sensor's response. Eq. (1) is the sensing principle of the SEC sensor, by which the capacitance can be computed once the sensing area *A* and sensor's thickness *h* are known. However, because the SEC sensor is not physically modeled, this equation cannot be applied directly since *h* is not available. Eq. (2) (Laflamme et

al., 2013) and Eq. (3) (Kharroub et al., 2014) describe the relationships between capacitance change and strain change for uniaxial and biaxial strain fields, respectively, where C_0 is the initial capacitance, ε_x and ε_y are the two principle strains, v is the Poisson's ratio of the sensing material with a typical value of 0.49.

$$\frac{\Delta C}{C_0} = 2\varepsilon \tag{2}$$

$$\frac{\Delta C}{C_0} = \frac{1}{1-v}\left(\varepsilon_x + \varepsilon_y\right) \tag{3}$$

However, both equations are still difficult to be implemented in the FE analysis, because the strain result in FE analysis is commonly reported as the average strain of the element, while the true strain is difficult to obtain. Furthermore, the strain level highly relies on the mesh distribution, which may affect the accuracy of computation results. To overcome these challenges, a modified equation is proposed as follows.

The proposed equation for capacitance calculation directly builds a relationship between sensor's capacitance response and change of the sensing area. From Eq. (1), the capacitance change of the SEC sensor under deformation can be expressed as:

$$\frac{\Delta C}{C_0} = \frac{C_1 - C_0}{C_0} = \frac{e_0 e_r \left(\frac{A_1}{h_1} - \frac{A_0}{h_0}\right)}{e_0 e_r \frac{A_0}{h_0}} = \frac{A_1 h_0}{A_0 h_1} - 1 \tag{4}$$

where C_0, A_0, h_0 are the initial capacitance, sensing area, and thickness of the SEC sensor, respectively. C_1, A_1, h_1 are the corresponding values after the sensing skin deforms. As mentioned previously, the Poisson's ratio of the sensing material is 0.49. The sensing skin can therefore be assumed as incompressible under deformation ($A_0 h_0 = A_1 h_1$). The thickness terms can be eliminated using:

$$h_0 = \frac{A_1 h_1}{A_0} \tag{5}$$

Substituting Eq. (5) into Eq. (4), the capacitance change of the sensing skin becomes:

$$\frac{\Delta C}{C_0} = \frac{A_1^2}{A_0^2} - 1 \tag{6}$$

Eq. (6) is under the assumption that the sensor deforms uniformly within the area *A*. In practice, however, the SEC sensor is likely to experience highly nonuniform deformation or strain under fatigue cracks. To accommodate nonuniform deformation, the sensing area is discretized using finite element meshes. Assuming each element of the sensing area experiences uniform deformation, Eq. (6) can be applied to each individual element. Within the sensing area *A*, the capacitance change of the i^{th} element can be expressed as:

$$\frac{\Delta C_i}{C_{0i}} = (\frac{A_{1i}^2}{A_{0i}^2} - 1) \tag{7}$$

The initial capacitance for each individual element C_{0i} is proportional to the area of the element A_{0i}:

$$C_{0i} = \frac{A_{0i}}{A_0} C_0 \tag{8}$$

Substituting Eq. (8) into Eq. (7), the capacitance change of the i^{th} element becomes:

$$\Delta C_i = \frac{A_{0i}}{A_0} C_0 (\frac{A_{1i}^2}{A_{0i}^2} - 1) \tag{9}$$

The total capacitance change ΔC of the sensing area *A* is the summation of the capacitance change from all *n* elements, which can be expressed as:

$$\Delta C = \sum_{i=1}^{n} \Delta C_i = \frac{C_0}{A_0} \sum_{i=1}^{n} A_{0i} (\frac{A_{1i}^2}{A_{0i}^2} - 1) \tag{10}$$

Finally, the relative capacitance change becomes:

$$\frac{\Delta C}{C_0} = \frac{1}{A_0} \sum_{i=1}^{n} A_{0i} (\frac{A_{1i}^2}{A_{0i}^2} - 1) \tag{11}$$

The advantage of Eq. (11) is two-fold. First, it requires knowledge of only the areas of each element before and after deformation, which can be obtained directly from displacements of the nodes from the FE model. Second, a physical FE model of the SEC sensor is not required because the thickness of the sensor h is eliminated in the equation.

Based on Eq. (11), the proposed procedure for capacitance simulation can be established based on FE results. As illustrated in Figure 6, the initial area A_{0i} and deformed area A_{1i} of each individual element can be collected from the FE model, which are then substituted into Eq. (11) to compute capacitance change. Additionally, since the SEC sensor remains uncracked even though the underneath substrate has cracked, the area change of all deleted elements during crack propagation (i.e. element 5 and 6 as illustrated in Figure 6) are included in the computation. This is done to take into account sensor's measurement over the crack path even though they are physically removed from the model for crack simulation.

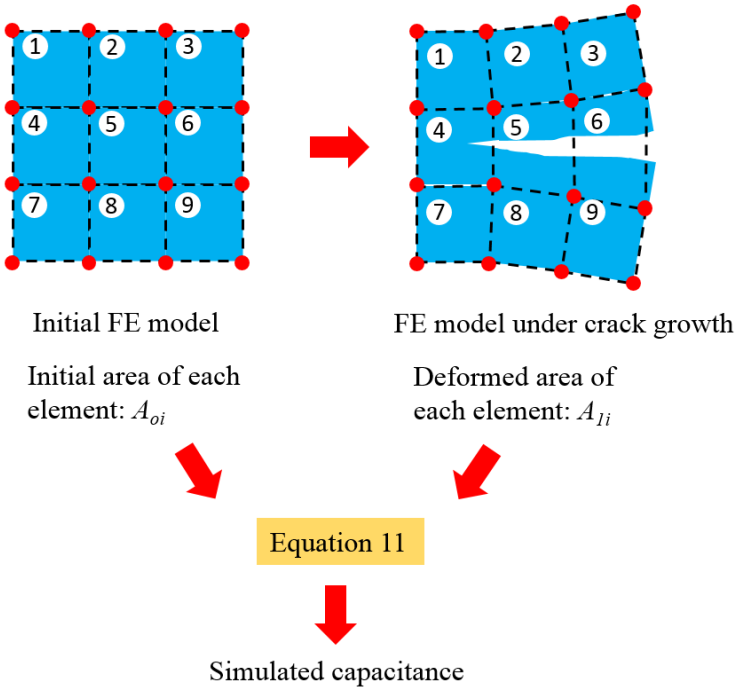

Figure 7. Proposed procedure for simulating capacitance response of the SEC sensor based on FE analysis

3.4. Validation of the numerical approach

In this section, the proposed numerical approach is validated through an experimental test with a small scale C(T) specimen. Since the accuracy of the simulated response of the SEC sensor is highly related to the accuracy of the size of the simulated crack, i.e. crack length and crack width, a two-stage validation is necessary. It includes 1) validation of the crack growth simulation method by verifying the capability of the FE model to predict the crack growth in the tested C(T) specimen; 2) validation of the capacitance calculation method using the experimentally measured capacitance. In what follows, the FE analysis is first introduced, followed by the presentation of the two-stage validation.

Table 1. Definition of material properties in the FE model

Material property	**Value**
Young's modulus	2.0×10^5 N/mm^2 (29,000 ksi)
Poisson's ratio	0.26
Yield stress	414 N/mm^2 (60 ksi)
Stress at initial damage point (max tensile stress)	552 N/mm^2 (80 ksi)
Strain at initial damage point	20%
Stress at failure point	0 N/mm^2 (0 ksi)
Strain at failure point	35%

An FE model of the C(T) specimen is created in Abaqus 6.13. The geometric dimensions of the FE model are the same as the test specimen, as shown in Figure 2(a). To simulate crack growth, material properties of A36 steel considering damage evolution theory are defined in

Table *1*. Physical meanings of some material properties are illustrated in Figure 6(a). The yield stress and maximum tensile stress of the material are determined by uniaxial tensile test of a coupon specimen.

Two types of shell elements are employed for the model including four-node (S4R) and three-node (S3) elements. Figure 8 shows the mesh distribution of the FE model, where a denser mesh is adopted along the crack path. The smallest element is at the tip of the notch (Figure 8a) with a size of 0.25 mm by 0.25 mm (0.01 in by 0.01 in), while elements at the corners have the largest size of 7.9 mm (0.31 in). The model contains a total of 4095 elements. To generate a fatigue crack, a cyclic load with a constant load range from 2.89 kN (0.65 kip) to 28.9 kN (6.5 kip) is applied to the FE model through the interior edges of both holes. The Abaqus/Standard module is selected as the solver for this analysis with variable step length.

Figure 8(b) shows a crack generated during the simulation, in which a series of elements are identified as failure elements and then removed automatically. Figure 8(c) shows the plastic strain at the tip of the crack. These results indicate that the crack growth is successfully simulated using the element deletion method.

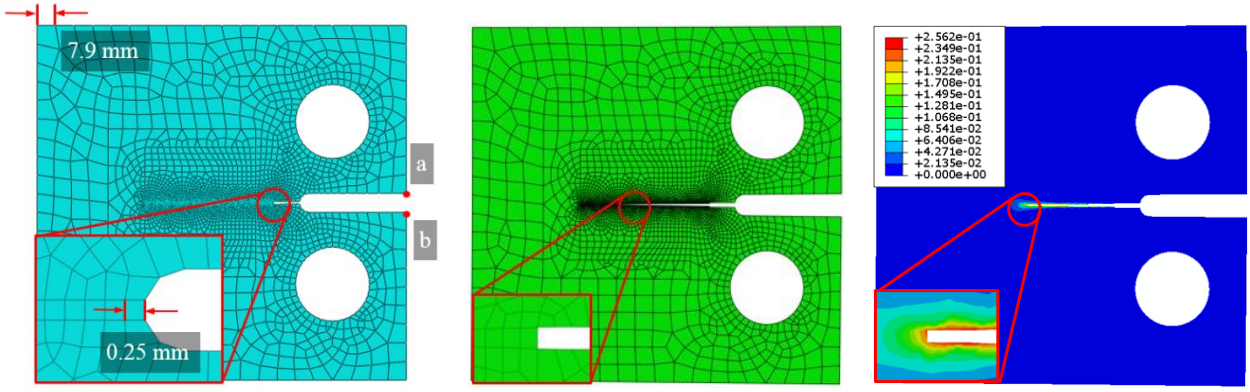

(a) (b) (c)

Figure 8. (a) Mesh distribution and typical element sizes; (b) simulation of crack growth; and (c) plastic strain at the crack tip

3.4.1 Stage 1 validation: accuracy of simulated crack

The purpose of this validation is to verify the capability of the FE model to predict crack size in the tested specimen. This validation procedure is conducted by comparing the compliance at the front face of the C(T) specimen when the crack reaches certain lengths. Figure 9(a) shows the

experimental setup, where a clip-on displacement gage (Epsilon model 3541) is mounted at the front face of the C(T) specimen through two knife edges to monitor the crack opening. Meanwhile, displacements at two points *a*, *b* at the same location in the FE model (Figure 8(a)) are collected for computing the crack opening in simulation. The compliance (Saxena and Hudak, 1978) at the front face of the C(T) specimen is defined as the ratio between the increment of crack opening ΔU measured by the clip gage and the increment of the applied load ΔF applied on the specimen (Figure 9(a)). Figure 9(b) shows a comparison of the FE model and the experimental dataset in terms of crack length vs. compliance. The crack lengths are measured by the adhesive measuring tape, starting from the tip of the notch (Figure 9(a)). The comparison shows a close match between test and FE model, indicating that the FE model can accurately predict the size of crack during crack growth.

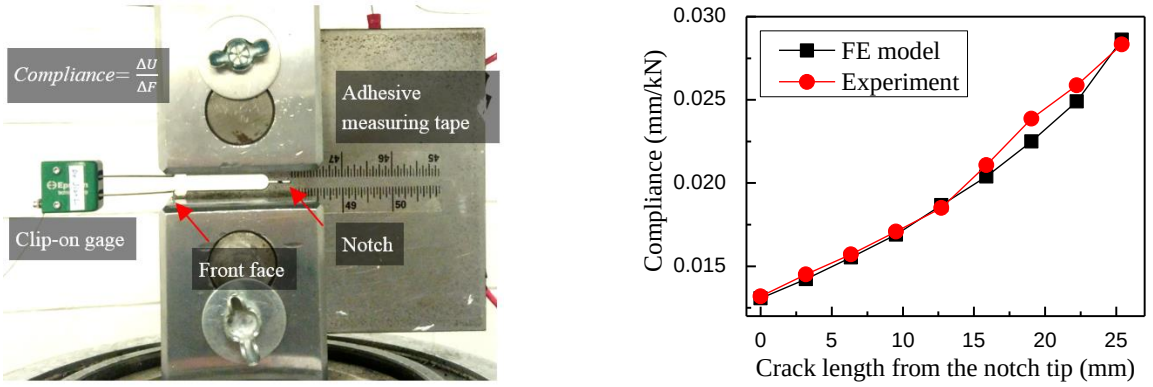

(a) (b)

Figure 9. (a) Installation of the clip-on displacement gage (the SEC sensor is attached to the back side of the specimen); and (b) compliance comparison between numerical and test results

3.4.2 Stage 2 validation: accuracy of sensor's capacitance response

Once the mechanical behavior of the FE model has been validated, the simulated sensor's capacitance response can be evaluated. The experimental data presented in Section 3.2.2 is used for this validation.

As mentioned in Section 3.2.2, the peak-to-peak percentage change of capacitance (*PP C/C₀*) is selected as a measure for detecting crack growth. The reason is that the absolute capacitance of the SEC sensor is prone to drift due to environmental factors such as temperature and humidity change during long-term monitoring. Figure 10 shows the comparison between simulation results and raw experimental data when the crack grows for each 3.2 mm (1/8 in) increments in length. The crack length in these plots is taken as the distance measured between the tip of the crack and the edge of the sensing area (Figure 4). Comparison in Figure 10 shows substantial agreement between test data and simulation in both amplitude and phase. It demonstrates also that the crack growth can be monitored by the steady increment of *PP C/C₀*. For instance, a 0.1% capacitance change can be observed at 1.6 mm (1/16 in) crack length, while the capacitance change increases by 3 times when the crack length reaches 17.5 mm (11/16 in).

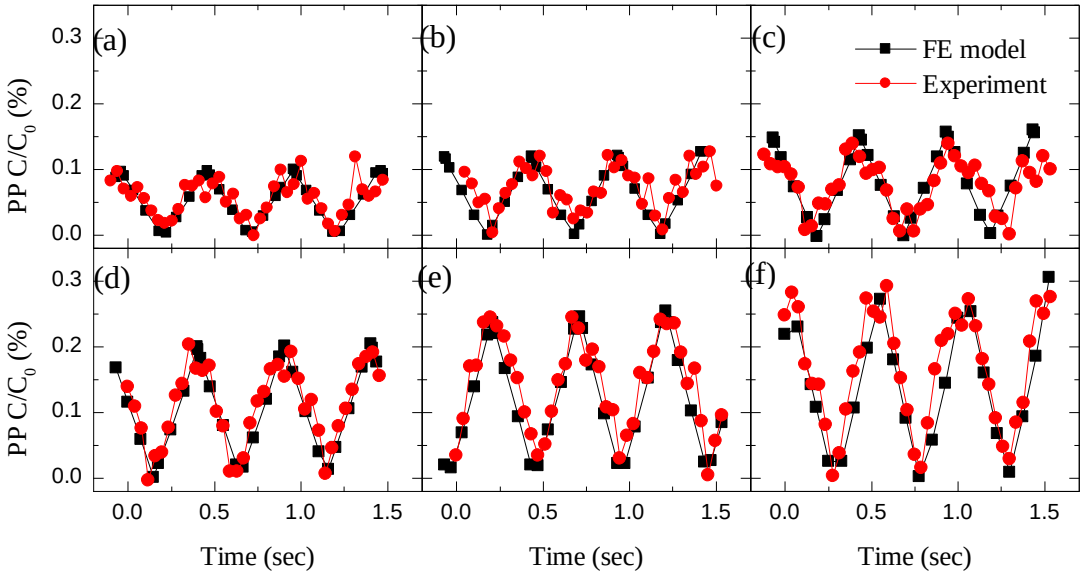

Figure 10. Comparison of the peak-to-peak percentage change of capacitance between simulation results and experimental data when the crack length reaches: (a) 1.6 mm; (b) 4.8 mm; (c) 7.9 mm; (d) 11.1 mm; (e) 14.3 mm; and (f) 17.5 mm

The comparison is further investigated in Figure 11 in terms of the *PP C/C₀* during the crack growth. The result indicates that the proposed numerical approach can predict a steady increment of capacitance change as the crack grows. This is in agreement with the experimental

data also showing a similar trend, despite a smaller increment observable over short crack sizes (from 1.6 mm (1/16 in) to 8.0 mm (5/16 in)). This feature can be attributed to the noise content in the raw capacitance measurements, which challenges the identification of changes in the electrical signal under low strain.

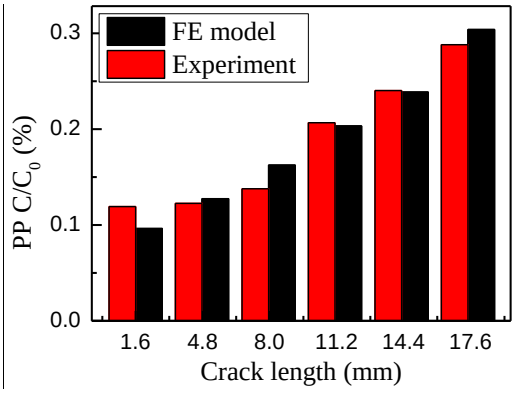

Figure 11. Comparison of the peak-to-peak percentage change of capacitance between simulation and experiment during the crack growth

Through the two-stage validation, the proposed methodology for numerical simulation has been verified for its ability to accurately predict sizes of the crack during propagation and the associated capacitance response of the SEC sensor. Following this validation, the methodology is applied to perform a parametric study to evaluate the effect of changing the size of the SEC sensor on its ability to detect fatigue cracks.

3.5 Crack monitoring with different sensor sizes

The SEC sensor can be fabricated or cut into different sizes to accommodate various application needs. Sensors with larger size can monitor larger structural surfaces prone to cracking; however, the electrical sensitivity of the sensor ($\frac{\Delta C}{(\varepsilon_x+\varepsilon_y)} = \frac{C}{1-\nu}$) against crack growth decreases with increasing sensor size. In addition, the data acquisition (DAQ) system may be optimized for capacitance measurement when customized to a specific measurement range which is directly related to the sensor size. The motivation of this parametric study is to quantitatively evaluate the

effect of the size of SEC sensors on the effectiveness of crack detection, and to provide guidance for dense sensor network optimization for practical applications.

Figure 12 shows four FE models of the C(T) specimen with different sizes of SEC sensor, which include 63.5 mm by 63.5 mm (2.50 in by 2.50 in) (full size), 47.6 mm by 47.6 mm (1.87 in by 1.87 in) (56% size), 31.8 mm by 31.8 mm (1.25 in by 1.25 in) (25% size), and 15.9 mm by 15.9 mm (0.63 in by 0.63 in) (6% size). Based on the geometric dimensions and material properties of the SEC sensor, the initial capacitance of the full size SEC sensor is 900 pF from Eq. (1), which is a typical value of the full size SEC sensor. Since the initial capacitance of the SEC sensor is proportional to the sensing area, initial capacitances of the 56% size, 25% size, and 6% size SEC sensors are computed as 506.3 pF, 225 pF, and 56.3 pF, respectively. The FE models are loaded with the same loading protocol described in Section 3.4. The capacitance responses of the SEC sensor are computed through the proposed algorithm.

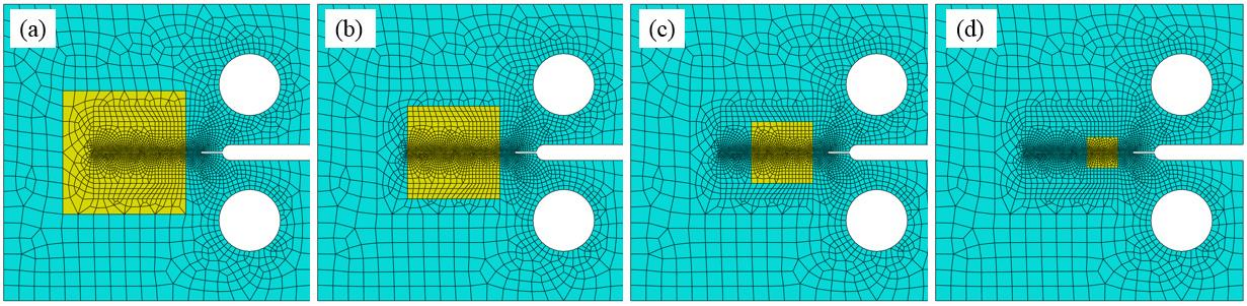

Figure 12. FE models with different sizes of sensing area, including (a) 63.5 mm by 63.5 mm (full size); (b) 47.6 mm by 47.6 mm (56% size); (c) 31.8 mm by 31.8 mm (25% size); and (d) 15.9 mm by 15.9 mm (6% size)

Results of this parametric study are shown in Figure 13. The crack length is measured as the distance between the tip of the crack and the edge of the sensing area (Figure 4). Both peak-to-peak percentage change ($PP\ C/C_0$) and peak-to-peak change of capacitance ($PP\ C$) are plotted in the figure against different sizes of the SEC sensor for three different crack lengths: 1.6 mm (1/16 in), 7.9 mm (5/16 in), and 14.3 mm (9/16 in). Results indicate that both $PP\ C/C_0$ and $PP\ C$

increase as the crack grows in length. Take the 6% size SEC sensor as an example, as the crack grows from 1.6 mm to 14.3 mm, *PP C/C₀* increases from approximately 0.5% to 2.0%, and *PP C* increases from approximately 0.25 pF to 1.1 pF. Moreover, when the sensor size decreases, the peak-to-peak change in capacitance (*PP C*) decreases as well. However, the peak-to peak percentage change of capacitance (*PP C/C₀*) increases, indicating that a smaller SEC sensor is more sensitive to cracking. For instance, for the 14.4 mm crack, the sensitivity of the 6% size sensor is approximately 8 times higher than the full size sensor. The tradeoff is that it covers only 6% of structural surface compared with the full size sensor. In practical applications, the optimal sensor size should be determined to achieve adequate sensitivity while maintaining as large coverage area as possible. A network may also be composed of several SECs of various size, depending on the required crack localization resolution. Figure 13 can also be used to predict the expected measurement range for detecting cracks under different lengths. The information can be used to optimize design of the DAQ system for capacitance measurement.

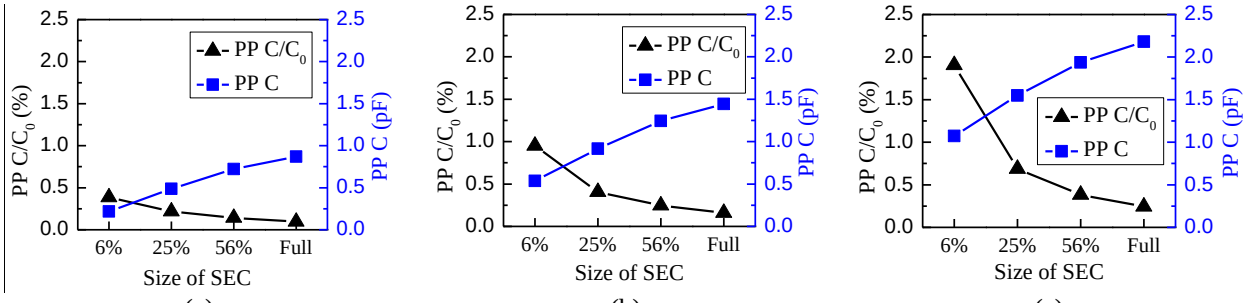

Figure 13. Capacitance change in terms of *PP C/C₀* and *PP C* for different sizes of sensor when crack reaches different length: (a) 1.6 mm, (b) 7.9 mm, and (c) 14.3 mm

3.6 Conclusions

This chapter furthers the understanding of a novel measurement method developed for detecting, localizing, and quantifying damage over mesosurfaces. This technology, the soft elastomeric capacitor (SEC), is a highly scalable strain gauge designed to be deployed in dense sensor

network configurations to mimic biological sensing skin. The contribution of this chapter is the development of a numerical approach to predict the SEC sensor's response under fatigue cracks.

The proposed approach consists of two parts: 1) simulating crack growth in the structure with FE analysis using an element deletion method, and 2) converting the FE analysis result into capacitance change of the SEC sensor. The numerical approach is validated by experimental data from a small scale C(T) specimen. The validation demonstrated that the numerical model of the C(T) specimen predicts accurate crack sizes during its propagation, and the proposed algorithm computes accurate capacitance response of the SEC sensor based on the FE result. The validated method is then applied to investigate the effect of changing the size of the SEC sensor on its ability to detect fatigue cracks. For the same crack size, smaller sensors are less sensitive in terms of peak-to-peak capacitance change, but more sensitive in terms of peak-to-peak percentage capacitance change. However, the coverage area may be greatly reduced by using a smaller sensor. The size of sensor therefore needs to be optimized to cover strategic areas at the desired resolution. The proposed approach enables dense sensor network applications of the SEC by linking the sensor's signal to a fatigue crack location and size. Being able to map a signal to engineering metrics is particularly helpful to infrastructure operators and managers by empowering them with the capacity to conduct condition-based maintenance.

Chapter 4: Small-Scale Experimental Investigation of Soft Elastomeric Capacitors for Fatigue Crack Monitoring

This chapter is modified based on the following journal publications:

Kong, X., Li, J., Collins, W., Bennett, C., Laflamme, S., & Jo, H. (2017). A large-area strain sensing technology for monitoring fatigue cracks in steel bridges. *Smart Materials and Structures*, 26(8).

Kong, X., Li, J., Collins, W., Bennett, C., Laflamme, S., & Jo, H. (2018). Thin-film sensor for fatigue crack sensing in steel bridges under varying crack propagation rate and random traffic load. *ASCE Journal of Aerospace Engineering*, In press.

4.1 Overview

The objective of this chapter is to determine whether soft elastomeric capacitors (SECs) are capable of being used as a fatigue monitoring device in common steel bridge applications. To accomplish this, the crack detection ability of the SEC was investigated in the context of high-cycle fatigue cracking, representative of cracking commonly encountered in steel bridges. Compared to low-cycle fatigue cracks, high-cycle fatigue cracks are generally subject to lower stress levels, are dominated by elastic deformation, and thus require a larger number of cycles to initiate and propagate. Importantly, crack openings under high-cycle fatigue are much smaller

than those generated by low-cycle fatigue. As a result, monitoring high-cycle fatigue cracking with the SEC can be expected to be a more challenging proposition than monitoring low-cycle fatigue cracking, since the sensor should produce smaller responses under smaller crack openings. Long-term robustness is also critical to deploying an effective crack monitoring strategy in order to ensure functionality over the life of the structure being monitored.

To address these challenges, it was hypothesized that peak-to-peak amplitude (pk-pk amplitude) could be used as an indicator for monitoring crack growth, which would exhibit low sensitivity to capacitance drift. A crack monitoring algorithm based on frequency analysis was developed for accurately identifying the pk-pk amplitude and then calculating the Crack Growth Index (*CGI*). The approach relies on measurements from the SEC's response as well as the applied fatigue loading. Load can either be directly measured when possible in a laboratory setting or indirectly measured via structural strain in the field. To experimentally evaluate the proposed algorithm, loading protocols were designed to generate high-cycle fatigue cracks in compact, *C(T)*, specimens that are similar to those one would see in full-scale steel bridges subject to traffic loading. The objective is to limit the plastic deformation at the crack tip throughout the fatigue testing. Finally, the hypodissertation, and the proposed algorithm, were experimentally evaluated using steel *C(T)* specimens instrumented with SECs for a series of high-cycle fatigue tests to examine whether crack growth could be successfully monitored based on the proposed approach.

4.2. Background

The SEC is a flexible capacitor formed by a dielectric layer sandwiched between to conductive layers acting as electrodes. The dielectric is composed of a styrene-ethylene/butylene-styrene (SEBS) block co-polymer filled with titania, and the conductive layers are fabricated by the same

SEBS, filled with carbon black (Figure 14b). The SEC is attached onto the surface to be monitored, typically using off-the-shelf bi-component epoxy. Strain produces a geometric change in the sensor, producing a corresponding change in capacitance. (Figure 14a). SECs can be fabricated in various sizes. A dimension of 76 mm by 76 mm (3 in by 3 in) was adopted in this chapter. The effective sensing area, or the area of the conductive layer, is 63.5 mm by 63.5 mm (2.5 in by 2.5 in). Figure 14c shows a picture of one SEC with two strips of copper tape embedded in the top and bottom conductive plates for connecting to the data acquisition (DAQ). A detailed description about the fabrication procedure of the sensor can be found in reference [16].

As illustrated in Figure 14b, when the monitored structures is under a tensile (or compressive) force, the surface strain provokes a change in the SEC's area A and thickness h, leading to a change ΔC in capacitance C. Starting with the approximation of the SEC as a pure capacitor

$$C = \frac{e_0 e_r A}{h} \tag{1}$$

where e_0 is the permittivity of air, e_r is the permittivity of the dielectric, $A = w \cdot l$ is the sensing area of width w and length l, and h is the thickness of the dielectric. It can be shown that, under uniaxial strain ε, the change in capacitance is given by (Kharroub et al., 2015):

$$\frac{\Delta C}{C} = \frac{1}{1-\nu}\varepsilon \tag{2}$$

where ν is the SEC's Poisson ratio (ν approx. 0.49, with 1/(1-ν) approx. 2).

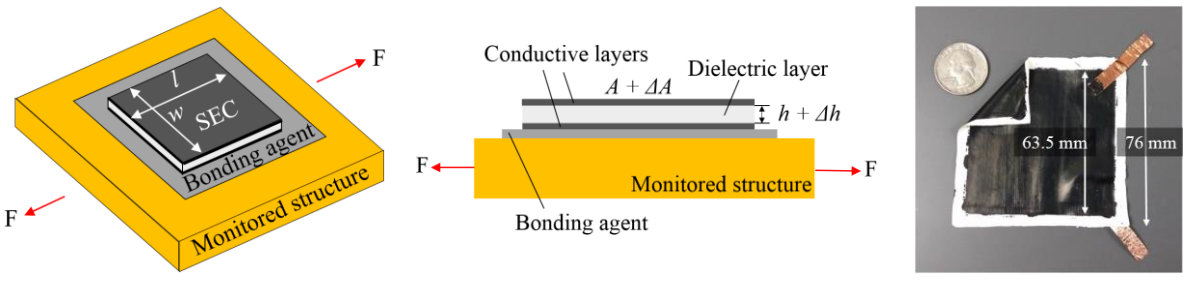

(a) (b) (c)

Figure 14. (a) Schematic of the SEC; (b) the SEC under a tensile strain; and (c) a picture of the SEC

The authors approached this investigation with a hypodissertation that the strain sensing ability of the SEC could be extended to fit the purpose of fatigue crack monitoring in steel bridges. Figure 15 demonstrates a supporting principle using a steel plate as an example. The fatigue load *F* is assumed to have a constant load range, and a fatigue crack initiates at the left edge of the plate and propagates to the right. The SEC is deployed on the plate prior to the crack initiation. Points *a*, *b*, and *c* represent three stages of crack propagation when the crack tip first reaches these locations.

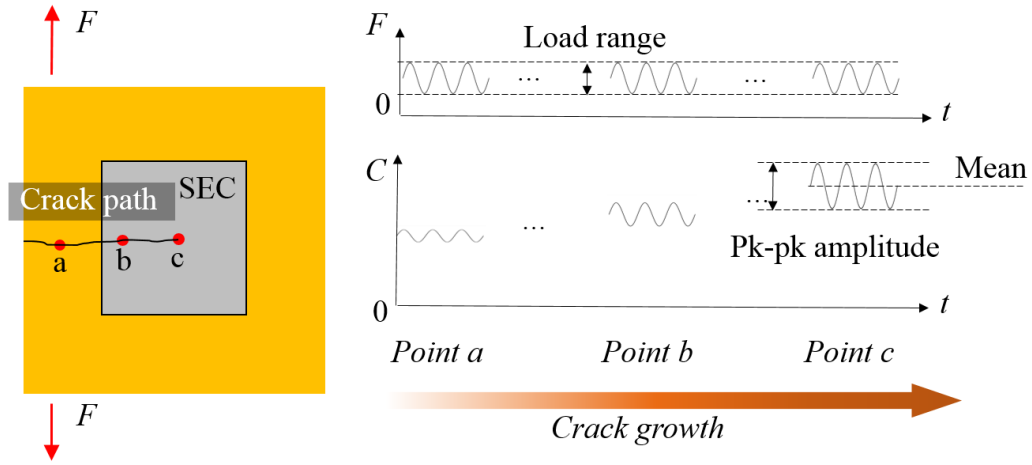

Figure 15. Schematic of the sensing principle for crack monitoring

The crack monitoring capabilities of the SEC can conceptually be thought of as occurring across three stages of crack growth:

1) When the crack is approaching the SEC (point *a*), the sensor can be treated as a large area strain gage, where localized strain changes can be measured by a change in capacitance *C*;
2) When the crack grows into the sensing area (point *b*), the crack opening beneath the sensing skin produces a stretch in the SEC, and thus causes an additional increase in capacitance. Therefore, larger responses in terms of both the mean and the pk-pk amplitude should be observable;
3) When the crack propagates further (point *c*), higher responses for both mean capacitance and pk-pk amplitude should be measurable. This is due to the fact that the crack weakens the local stiffness of the plate (i.e. the crack opens more under same range of the load).

A challenge associated with SECs is that measurements can be subject to capacitance drift (Ubertini et al., 2014) during long-term monitoring due to environmental factors such as temperature or humidity changes, and to an intrinsic electrical behavior found in many sensors fabricated from smart materials (Cai et al., 2013, Kang el al., 2006).

To ensure robustness against capacitance drift, the pk-pk amplitude of the capacitance measurement (as illustrated in Figure 15) was hypothesized to be an indicator of cracking useful for long-term monitoring of fatigue cracking. By extracting only the pk-pk amplitude, the drift effect in the mean capacitance can be filtered out. To illustrate, denote $C_{pk\text{-}pk}$ as the pk-pk amplitude of the sensor's capacitance. $C_{pk\text{-}pk}/C_m$ is then the percentage change of capacitance of the SEC reflecting the amount of strain transmitted to the SEC, where C_m is the mean capacitance. Using the sensing principle (Equation 2):

$$\frac{C_{pkpk}}{C_m} = 2\varepsilon \tag{3}$$

Now, assume that the excitation load range ΔF is constant over the long-term period, but that the capacitance drifts by ΔC_m, as illustrated in Figure 16. Such a drift would provoke a change to the pk-pk amplitude ΔC_{pkpk} as well. Since the monitored strain remains constant before and after the drift, the corresponding relative change in capacitance should remain the same:

$$\frac{C_{pkpk}}{C_m} = \frac{C_{pkpk} + \Delta C_{pkpk}}{C_m + \Delta C_m} = 2\varepsilon \tag{4}$$

Rearranging Equation 4 provides:

$$\frac{\Delta C_{pkpk}}{C_{pkpk}} = \frac{\Delta C_m}{C_m} \tag{5}$$

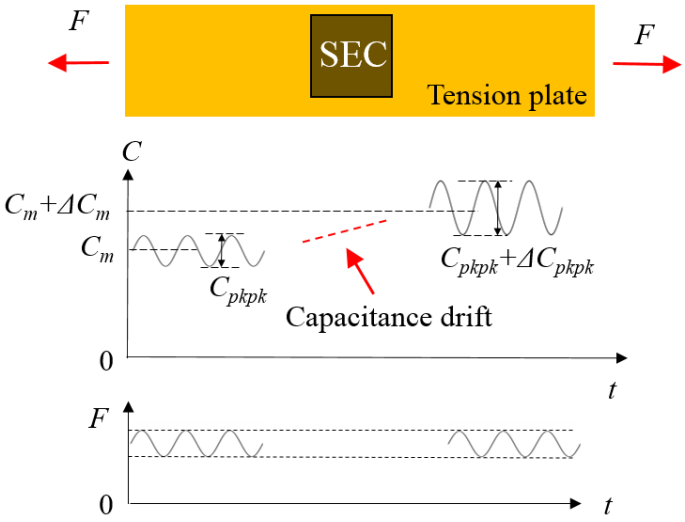

Figure 16. Illustration of drift impact on both mean and pk-pk amplitude of capacitance measurement

Equation 5 indicates that the percentage change of the pk-pk amplitude caused by the capacitance drift $\Delta C_{pkpk}/C_{pkpk}$ is the same as the percentage change of the mean capacitance $\Delta C_m/C_m$. In the fatigue tests of this chapter, a maximum capacitance drift was found as 10 pF during a period of several weeks, leading to $\Delta C_{pkpk}/C_{pkpk} = \Delta C_m/C_m$ = 10 pF / 900 pF = 1.1 %, in which the 900 pF is a typical mean capacitance C_m of the SECs. On the other hand, test results in this chapter also showed that $\Delta C_{pkpk}/C_{pkpk}$ caused by crack growth reached 100% when the crack

grows from 0 mm (0 in.) to 46.0 mm (29/16 in.). Such an increment provoked by the crack growth (100%) is much larger than the change of capacitance drift (1.1%) so that the drift can be neglected for tests in this study.

The pk-pk amplitude is sensitive to signal-to-noise ratio due to its small magnitude. For high-cycle fatigue cracks, the pk-pk amplitude can even be smaller, given that fatigue in steel bridges is usually driven by relatively low stress ranges. To robustly and accurately identify pk-pk amplitude, a crack monitoring algorithm is proposed based on frequency analysis, as explained in the next section.

4.3. Crack monitoring algorithm for high-cycle fatigue cracks

An illustration of SEC application for crack monitoring in steel bridges is shown in Figure 17. Fatigue cracks can take years to decades to initiate and propagate before reaching a critical size (Zhao and Haldar, 1996). For this reason, continuously collecting data throughout bridge service life is impractical. An effective crack monitoring strategy would follow a multi-timescale (Gupta and Ray, 2007): a fast timescale for data collection and a slow timescale for tracking crack growth. As shown in Figure 17, in the fast timescale monitoring, a short-time measurement is taken by the SEC network. Within the period of measurement, the fatigue crack can be assumed unchanged. An indicator of crack length can be extracted for this particular point-in-time using a crack monitoring algorithm. By taking multiple fast timescale measurements and extracting features of crack length over the slow-timescale over the entire fatigue life, the global behavior of crack growth can be identified.

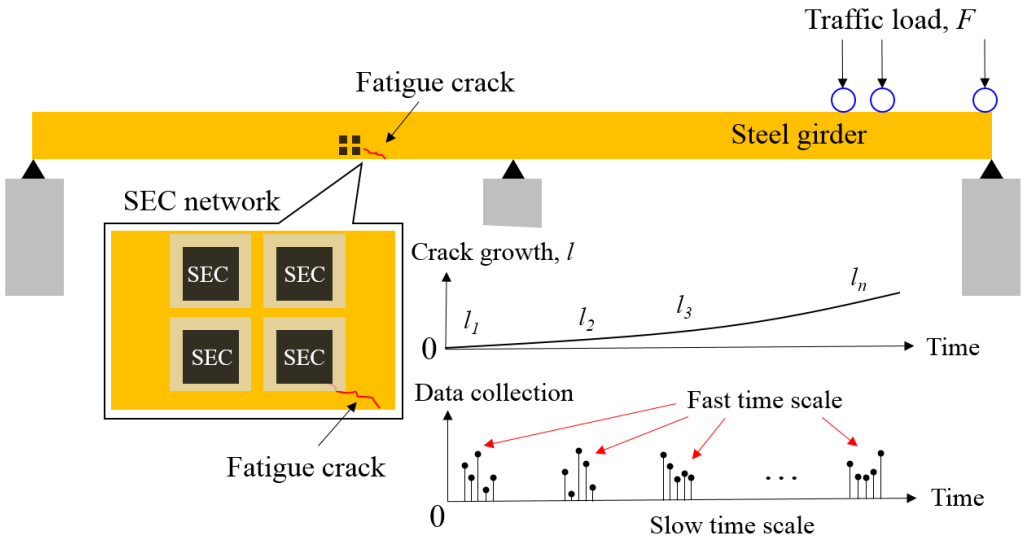

Figure 17. Demonstration of fatigue crack monitoring in steel bridges using SEC network

For this approach to be viable, a computed value is required to serve as an indicator of crack length; the Crack Growth Index (*CGI*) was developed to serve as such an indicator. The *CGI* acts as a normalized strain indicator from which crack growth under the SEC can be inferred. Figure 18 depicts the steps used in the developed crack monitoring algorithm for extracting the *CGI*. The algorithm is a four-step procedure including data acquisition, frequency analysis, establishing *CGIs*, and crack growth monitoring.

The first step in the monitoring algorithm is data acquisition (Figure 18a). A series of short time measurements are taken as the crack grows to different lengths (l_i). Both capacitance measurements $C_i(t)$ of the SEC and force measurements $F_i(t)$ of the fatigue load are collected. The pk-pk amplitude of the SEC is directly related to the opening of the crack, but is also affected by the magnitude of load. To successfully identify crack growth through the SEC's response, the capacitance measurements $C_i(t)$ should be normalized with respect to the level of fatigue load. The fatigue load can either be directly measured or indirectly determined via strain measurements.

The next step in the monitoring algorithm is to convert the capacitance, $C_i(t)$, and force measurements, $F_i(t)$, from the time domain to Power Spectral Densities (PSDs) in the frequency domain. Physically, a PSD represents the energy distribution of a signal in the frequency domain. The peak amplitude is then identified to represent the pk-pk amplitude of the time series. Compared with identifying the pk-pk amplitude in the time domain, the peak of the PSD in the frequency domain is less sensitive to noise content in the measurements. As shown in Figure 18b, $peak_i^F$ is denoted as the PSD peak of the i^{th} force measurement $F_i(t)$, and $peak_i^C$ as the PSD peak of the i^{th} sensor measurement $C_i(t)$. Both $peak_i^F$ and $peak_i^C$ should locate at the same frequency (i.e. the loading frequency), but may have different amplitudes.

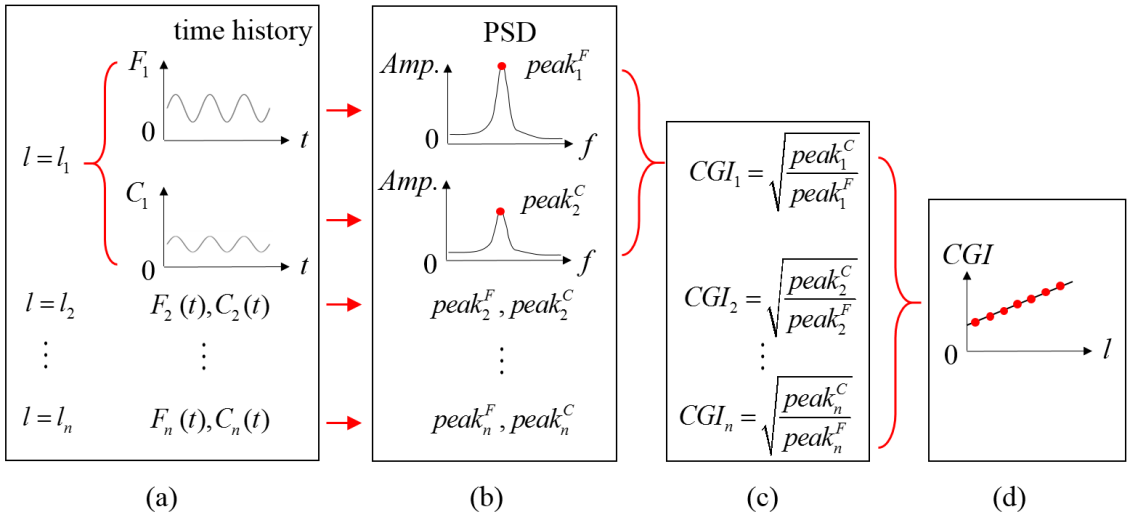

Figure 18. The four-steps involved in the proposed crack monitoring algorithm: (a) data acquisition; (b) frequency analysis; (c) establishing *CGIs*; and (d) crack growth monitoring

Once the PSD peaks are obtained, *CGIs* can be computed using equations shown in Figure 18c. *CGI* is a feature extracted from sensor's measurement $C_i(t)$ and applied load $F_i(t)$. It represents the level of the pk-pk amplitude under a unit excitation load.

In the final step of the algorithm, crack growth is monitored using the *CGI* values. Specifically, CGI_i at the i^{th} measurement is correlated with its crack length l_i, so that a curve between *CGI* and crack length can be established (Figure 18d).

Fatigue testing was performed as part of this study to evaluate to what extent crack growth can be indicated by monitoring increasing *CGI*, and to evaluate the overall effectiveness of the monitoring algorithm.

4.4 Fatigue loading protocols

In previous investigations focused on the SEC performance in the presence of low-cycle fatigue cracks (Kong et al., 2015a; 2015b; 2016a), a fatigue load with a 26.0 kN (5.85 kip) constant range was applied to specimens. However, a constant load range only guarantees relatively small crack openings in the early stages of crack propagation. As the crack grows longer, excessive opening and plastic deformation at the crack tip can occur due to significant stiffness reduction. This leads to crack characteristics which are not representative of fatigue cracks that commonly occur in steel bridges.

To generate realistic high-cycle fatigue cracking, the loading protocol used in this study was based on maintaining a constant range of applied stress intensity, ΔK. A relatively low value for ΔK was used to limit formation of a large plastic zone at the crack tip so that crack openings remained small even as the crack length increased. This approach generated fatigue cracks that are more representative in steel bridges. ΔK is the range of stress intensity within one load cycle and can be expressed as:

$$\Delta K = K_{\max} - K_{\min} \tag{5}$$

where K_{max} and K_{min} are the maximum and minimum stress intensity factors. In fracture mechanics, ΔK is a parameter representing the stress state change around the crack tip caused by

the fatigue load ΔF. According to ASTM E1820-15 (ASTM, 2015), for the compact tension specimen adopted in this study (Figure 19), ΔK can be determined as:

$$\Delta K = \frac{\Delta F}{B\sqrt{W}} f(\frac{a}{W}) \tag{6}$$

where $\Delta F = F_{max} - F_{min}$ is the difference between the maximum load F_{max} and the minimum load F_{min} in one load cycle; B is the thickness of the specimen; a is the length of the crack measured from the load line; and W is the distance between load line and the back face of the specimen. The term $f(a/W)$ in Equation 6 is a polynomial with the variable a/W. Detailed expressions for $f(a/W)$ can be found in reference (ASTM, 2015). Dimensions a and W are also labeled in the schematic presented in Figure 19.

From Equation 6, ΔF can be determined once a desired ΔK is established, but this requires knowledge of F_{max} and F_{min}. A common approach is to introduce the stress ratio, $R = K_{min} / K_{max} = F_{min} / F_{max}$, representing the ratio of maximum stress and minimum stress in one load cycle. In the case of steel bridges, R is the ratio between the magnitude of live load-induced stress (i.e. vehicle load) and the magnitude of dead load-induced stress (i.e. bridge self-weight), at a particular location on the structure.

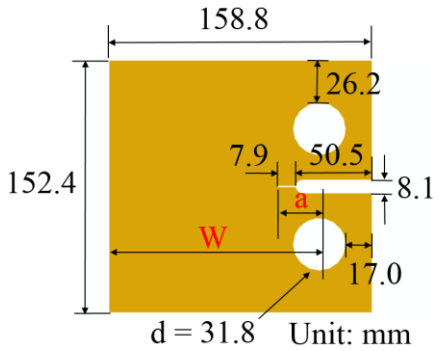

Figure 19. Dimensions of the *C(T)* specimen

The procedure used to apply the loading protocol is summarized in Figure 20. A constant ΔK was first assigned. Then, based on ASTM E1820 (ASTM, 2015), the corresponding ΔF for the targeted ΔK was computed. Finally, a chosen magnitude for the stress ratio R guarantees a unique solution of F_{max} and F_{min}, so that the loading protocol can be applied using load control. Three R values were used in the test program: 0.1, 0.4, and 0.6, simulating stress ratios caused by passing vehicles with different weights in steel bridges.

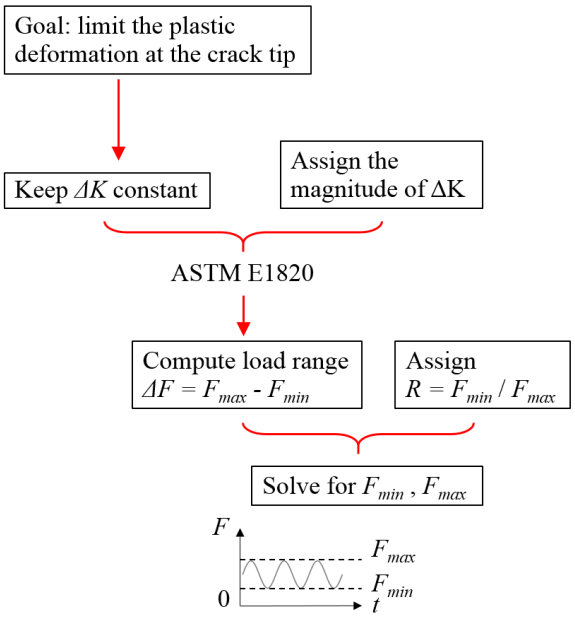

Figure 20. Procedure for determination of the fatigue loading protocol

4.5 Experimental validations

The SEC's ability to monitor high-cycle fatigue cracks was investigated through fatigue testing performed on steel *C(T)* specimens. The suitability of the monitoring algorithm was evaluated based on the experimental findings.

4.5.1 Test configuration

A series of small-scale steel specimens equipped with SECs were tested under fatigue loading using a constant ΔK. *C(T)* specimens were fabricated from A36 steel plates of 6.4 mm (1/4 in.)

thickness. Figure 19 shows the dimensions of the *C(T)* specimen. The specimens were loaded using a closed-loop servo-hydraulic uniaxial load frame utilizing two clevises. Two adhesive measuring tapes were adhered to the front face of each specimen to allow for visual measurement of crack length during testing. The SEC was attached to the back face of the specimen using bi-component epoxy JB-Weld (Figure 21b), while the top and bottom conductive layers of the SEC were connected to a DAQ system (ACAM PCAP02) for measuring the capacitance response.

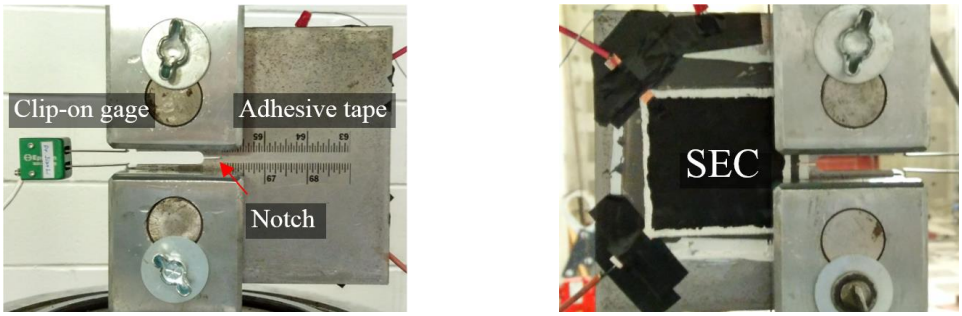

(a) (b)

Figure 21. (a) Front face of the specimen; and (b) back face of the specimen

Table 2 summarizes the experimental testing procedures used on the three tests included as part of this study, as well as the previous low-cycle fatigue test (Kong et al., 2016a; 2016b). Test 1 was performed using R=0.1. Tests 2 and 3 were performed with identical test parameters, using R=0.6 during crack propagation, but R=0.4 and R=0.6 during each data collection interval. This was done to enhance an understanding of the influence of the stress ratio on SEC performance.

A loading frequency of 10 Hz was used for initiating and propagating fatigue cracks. Data collection was performed at every 1.6 mm (1/16 in.) increment of crack growth, and the loading rate was reduced to 0.5 Hz while data was being collected. For each data collection interval, data were sampled at 50 Hz over 100 cycles, and measurements were recorded for

actuator force and capacitance of the SEC. After each data collection interval, the fatigue loading rate was returned to 10 Hz so that the crack propagation could be continued.

Table 2. An overview of the procedure on experimental testing

Test number	**Range of stress intensity factor ΔK**	**Crack propagation**	**Data collection**
Test 1	22.0 to 27.5 $MPa\sqrt{m}$ (20 to 25 $ksi\sqrt{in.}$)	R = 0.1	Figure 22, R = 0.1
Test 2 and Test 3	22 $MPa\sqrt{m}$ (20 $ksi\sqrt{in.}$)	R = 0.6	Figure 22, R = 0.4 Figure 22, R = 0.6
Previous Low-cycle Fatigue Test (Kong et al., 2016a)	48.3 to 146.7 $MPa\sqrt{m}$ (44.5 to 133.5 $ksi\sqrt{in.}$)	R = 0.1	Figure 22, R = 0.1

Figure 22 presents the loading protocols applied in the tests with different R ratios: 0.1 (Test 1), 0.4 (Tests 2 and 3), and 0.6 (Tests 2 and 3). The loading protocol used by (Kong et al., 2016a) for low-cycle fatigue testing is also shown for comparison. It can be seen that the ΔK values used in Tests 1, 2, and 3 were much smaller than used in (Kong et al., 2016a), representing a higher demanding on the SEC's resolution. Note that crack lengths in these plots were measured from the notch of the specimen (Figure 21a).

The relationship between stress intensity factor, applied stress, and crack length defined in Equation 6 indicates that a longer crack length, a, should correspond to a smaller ΔF if the target ΔK is fixed. This relationship mandates that the difference between the minimum and maximum bounds of the fatigue loading should decrease as the crack grows. As shown in Figure 22a, a multi-stage loading protocol was adopted in Test 1, in which ΔF was re-computed and adjusted for every 9.5mm (3/8 in.) of crack propagation, maintaining an approximately constant ΔK within a range between 22.0 $MPa\sqrt{m}$ to 27.5 $MPa\sqrt{m}$ (20 $ksi\sqrt{in.}$ to 25 $ksi\sqrt{in.}$). In Tests 2

and 3, shown in Figure 22b and c, more frequent adjustments were made by decreasing ΔF every 1.6 mm (1/16 in.) of crack growth. This ensured that ΔK was maintained at 22.0 $MPa\sqrt{m}$ (20 $ksi\sqrt{in.}$) throughout Tests 2 and 3.

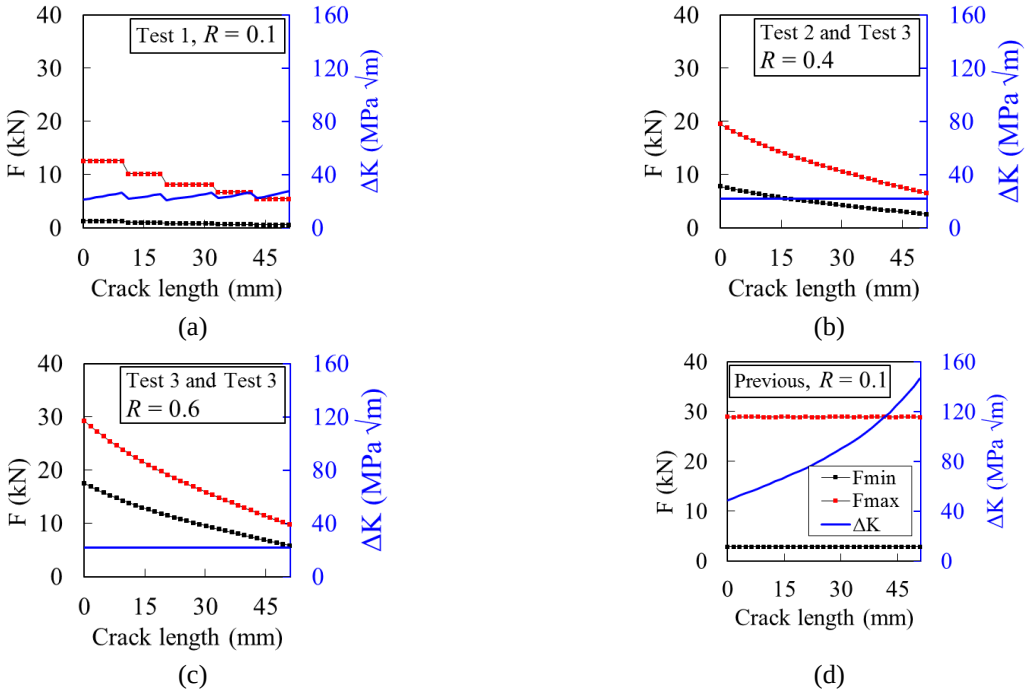

Figure 22. (a) Test 1 loading protocol, R = 0.1; (b) Test 2 and 3 loading protocol, R = 0.4; (c) Test 2 and 3 loading protocol, R = 0.6; and (d) Loading protocol used in prior low-cycle fatigue test (Kong et al., 2016a), R = 0.1. Red dotted line represents F_{max}, black dotted line represents F_{min}, and blue line represents ΔK.

4.5.2 Crack growth under the new loading protocols

Figure 23 presents a comparison between cracking generated by maintaining an approximately constant value for ΔK, and that generated in previous testing by maintaining a constant value for ΔF. Although the crack sizes obtained in Tests 1 is significantly longer than that observed during the previous low-cycle fatigue testing, crack opening was observed to be much smaller. Due to the large crack opening in the previous test, excessive plastic deformation produced a dimple which could be observed at the crack tip, while such plastic deformation was not observed in the tests performed as prt of the current study.

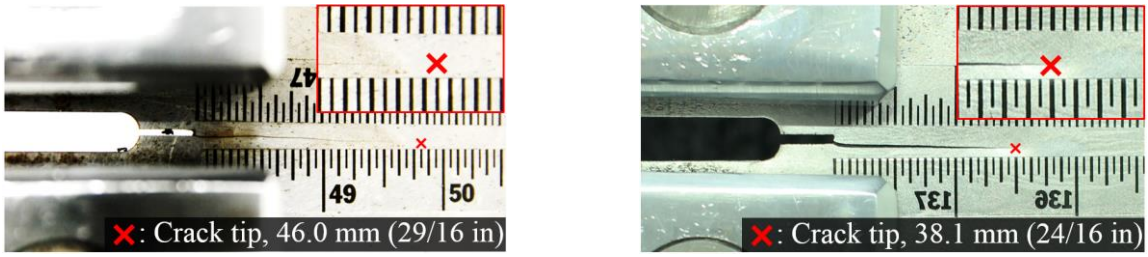

(a) (b)

Figure 23. Pictures of cracks showing different features between the new and previous tests: (a) crack in Test 1 at 46.0 mm (29/16 in.); and (b) crack from previous testing (Kong et al., 2016a) at 38.1 mm (24/16 in.).

Table 3 summarizes the fatigue test results, and includes the number of cycles applied, final crack length, and fracture status. Because the load range was continuously decreased in Tests 1, 2, and 3, these specimens did not experience fracture. In the previous test, the specimen failed in ductile tearing when the crack reached a length of 37.1 mm (24/16 in.). Tests 1, 2, and 3 produced significantly longer fatigue lives than noted in the specimen previously tested because of the lower ΔK. In particular, nearly 2 million cycles were applied in Test 1, which was performed at the lowest stress ratio (R = 0.1).

Table 3. Fatigue testing results

Test number	Number of cycles	Final crack length	Specimen fracture
Test 1	1,810,000	46.0 mm (29/16 in.)	No
Test 2	660,000	50.8 mm (32/16 in.)	No
Test 3	605,000	50.8 mm (32/16 in.)	No
Previous Low-cycle Fatigue Test (Kong et al., 2016a)	14,500	37.1 mm (24/16 in.)	Yes

4.5.3 Evaluation of proposed crack monitoring algorithm

Figure 24 presents sample raw capacitance measurements from the SECs in Tests 1, 2, and 3 as cracking propagated in the *C(T)* specimens. For better pk-pk amplitude comparisons, all the measurements have been detrended to have a zero mean. Results in these figures show an

increasing trend of pk-pk amplitudes as cracking propagated. For example, the pk-pk amplitude increased from approximately 0.5 pF to 2 pF when the crack grew from 0 mm (0 in.) to 46.0 mm (29/16 in.). The SEC's measurements showed similar levels of response among the tests for similar crack lengths. One example is that pk-pk amplitudes were approximately 2 pF for all three tests (and all three R values tested) when the crack reached 46.0 mm (29/16 in.), as shown in the last column of the figures. This finding indicates that for a certain crack length, sensor response is governed by load range ΔF and is invariant to stress intensity ratio R.

Figure 24 also exhibits noise content in the capacitance measurements, especially when crack lengths were short. Identifying the pk-pk amplitudes directly from the raw measurements in the time domain will suffer from uncertainty due to this noise content. For this reason, the proposed crack monitoring algorithm based on frequency analysis was utilized.

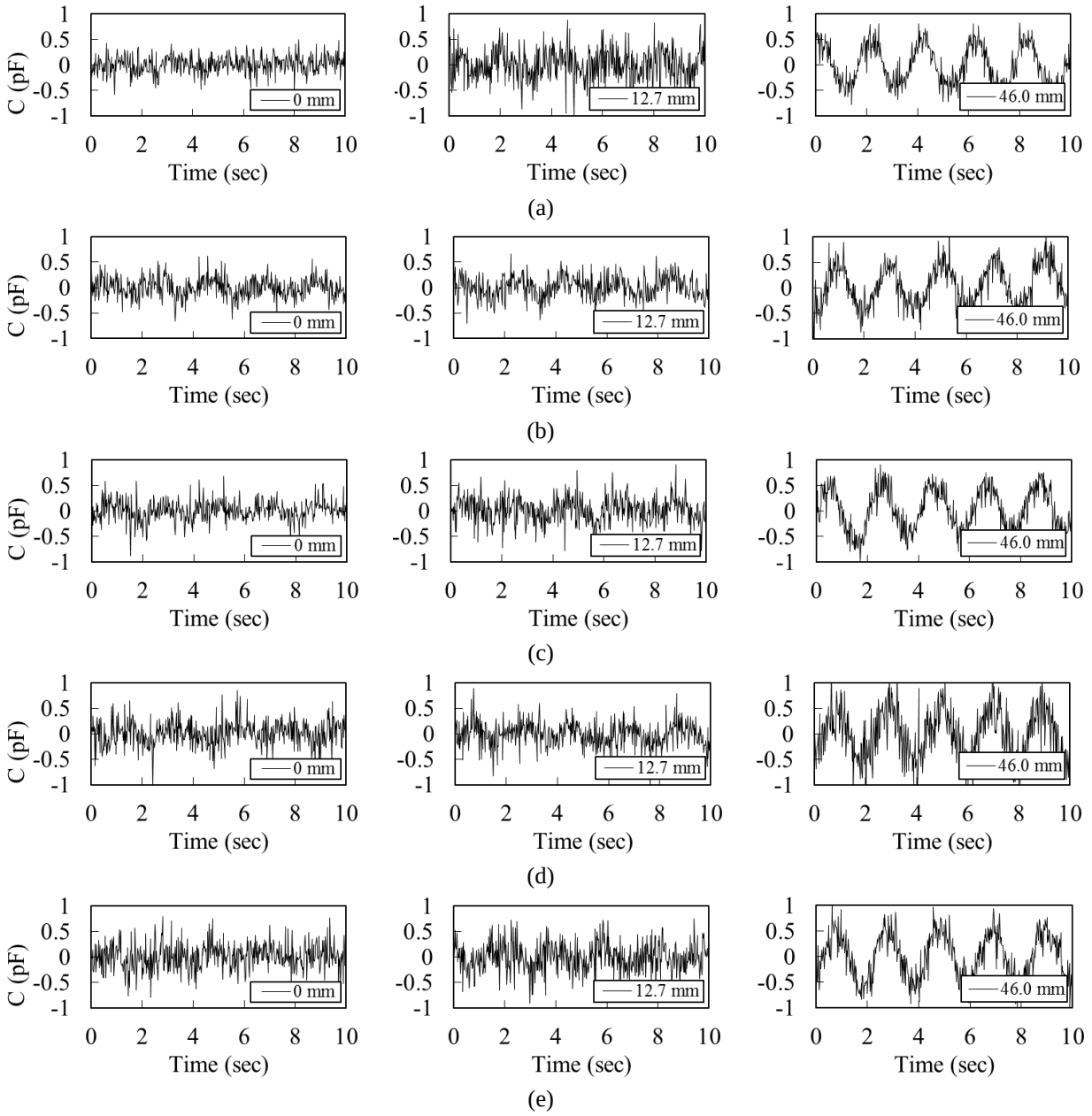

Figure 24. Sample raw measurements of SECs when the crack propagates to different lengths: (a) Test 1, R = 0.1; (b) Test 2, R = 0.4; (c) Test 2, R = 0.6; (d) Test 3, R = 0.4; and (e) Test 3, R = 0.6. The crack lengths are indicated in each plot.

Figure 25 shows the outcome of the crack monitoring algorithm for all testing cases. The plot for Test 1 is missing data for some crack lengths. This is due to faster than anticipated crack growth. In subsequent tests, more frequent observations were scheduled in order to avoid this loss of data.

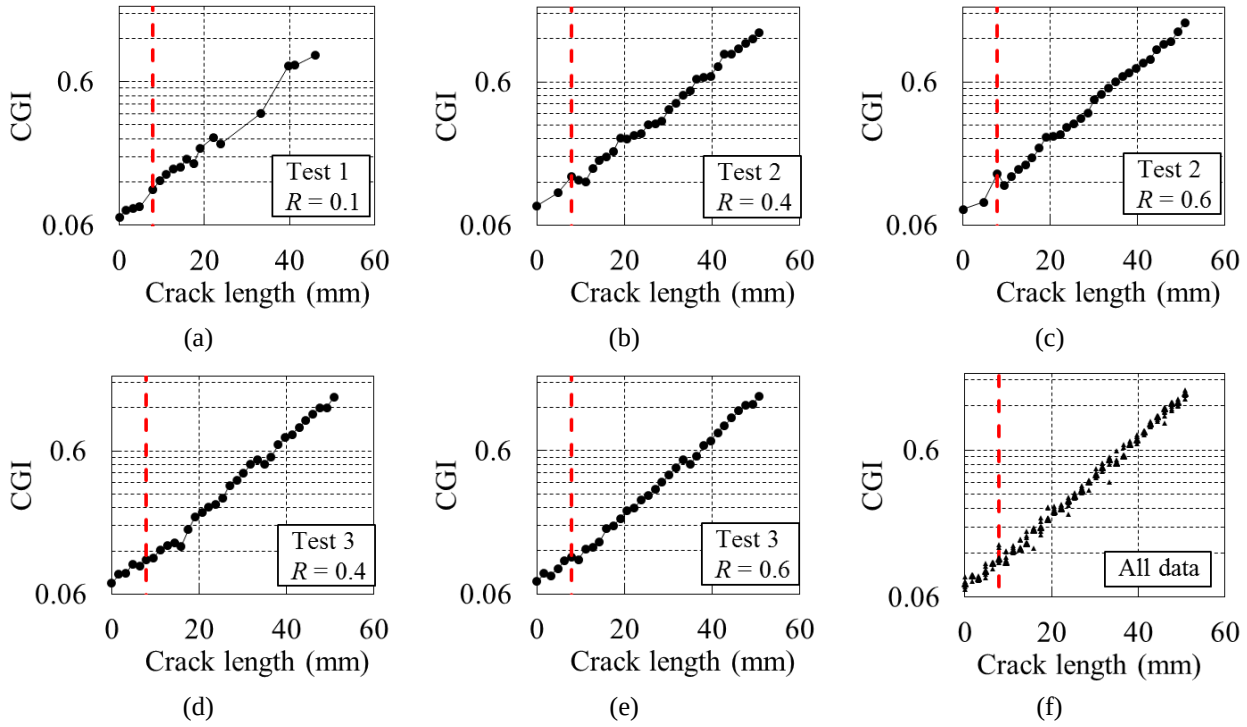

Figure 25. Representative measurements of SECs as the crack propagated to different lengths: (a) Test 1; (b) Test 2, R = 0.4; (c) Test 2, R = 0.6; (d) Test 3, R = 0.4; (e) Test 3, R = 0.6; and (f) a comparison of all data. Red dashed line indicates the start of effective sensing area on the SEC.

The crack length in Figure 25 is measured from the notch of the specimen. However, due to the fact that the effective sensing area of the SEC is less than its outermost dimensions, the crack does not reach the effective sensing area when it initiates from the notch. As shown in Figure 26, the notch is at a distance of 7.9 mm (5/16 in.) from the edge of the sensing area. The dashed red line in Figure 25 indicates the start of the SEC's effective sensing area.

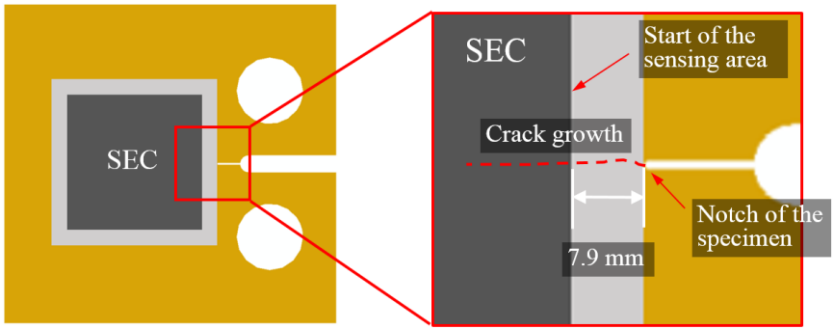

Figure 26. Demonstration of the boundary of the sensing area

A positive correlation between *CGI* and crack length can be clearly observed in Figure 25a-e. An approximate linear relationship was identified between crack length and log(*CGI*). The data shows that fatigue crack growth can be successfully identified by monitoring the *CGI* values produced based on the developed algorithm. Furthermore, such a trend also exists when the crack is approaching, but has not quite reached the sensing area, as shown by the data points prior to the red dashed line. This is because the SEC essentially acts as a large-area strain gauge for monitoring the increasing strain field cause by crack growth. As a crack monitoring method based on direct strain measurement, its effectiveness is validated when the crack is either close to or directly underneath the SEC.

Figure 25f shows a compilation of *CGIs* for Tests 1, 2, and 3. Excellent agreement was observed between all tests in which fatigue loading with different stress intensity ratios were applied. Considering the fact that a bridge under traffic loading is subject to changing stress intensity ratios over time, the result in this plot indicate the SEC could robustly monitor high-cycle fatigue cracks under different stress ratios, *R*.

Based on the finding, the proposed crack monitoring algorithm provided a good solution for monitoring fatigue crack growth using an SEC. The algorithm showed robustness even when the crack was small and the measurements were contaminated by noise content. Moreover, the proposed algorithm proved to be applicable for various loading conditions.

4.6 Evaluation of the SEC under varying crack growth rate and random traffic load

4.6.1 Motivation

Research work reported in this chapter by far were based on a constant crack growth rate under harmonic traffic load. Before the SEC-based crack sensing technology can be translated from laboratory to field applications, two research questions need to be addressed. The first research

question was whether the SEC can be expected to produce false-positive results during long-term monitoring. Crack propagation in the field is likely to be driven by more complex loadings than the constant crack growth rate. The stress intensity factor range at the crack tip, ΔK, which is the driving force behind crack growth, can be expected to fluctuate due to changing loading and structural conditions in the field. As a result, the crack propagation rate may fluctuate, and in some cases, the crack may stop growing when ΔK approaches its threshold for crack growth. To ensure that the SEC is capable of consistently monitoring crack growth over the long-term without false-positive results, it is critical to evaluate the SEC-based crack sensing technology under varying crack propagation rates.

The second research question is whether the SEC is still functional as a fatigue crack sensing device under more realistic loading cycles occurring in steel highway bridges. In field applications, traffic loads are composed of a series of load cycles due to passing vehicles. These load cycles can be expected to have different peak-to-peak amplitudes and periods. The load cycles used in Section 4.5 were based on a harmonic time series with a single period and a constant peak-to-peak amplitude, which does not fully capture realistic traffic load cycles in steel highway bridges.

In this section, we examined these two research questions through fatigue test of a steel C(T) specimen. First, a new loading protocol was created to generate and propagate a fatigue crack under a decreasing ΔK, eventually diminishing all the way to the material threshold for crack growth. As a result, the crack propagation rate continued to decrease until crack growth arrested. Measurements of the SEC under harmonic load cycles were collected, from which crack growth features were extracted. The SEC's crack monitoring performance under the decreasing crack propagation rate was then assessed. The result was also investigated when the

crack stopped growing (i.e. when ΔK approached the threshold for crack growth). Second, new stochastic traffic load was established using random peak-to-peak amplitudes and periods, designed to simulate realistic features of traffic loads of steel bridges. An updated crack sensing algorithm was established for extracting crack growth features to investigate the SEC performance under the simulated random traffic load cycles.

4.6.2 Load range design

Load range is a critical parameter that governs fatigue crack propagation. Given that one of the research questions being investigated was whether the SEC would produce "false-positive" readings at low load ranges, our objective in selecting a loading protocol was to determine the upper and lower bounds of a load cycle (i.e. F_{max} and F_{min}), and to adjust those bounds during crack propagation to achieve a decreasing crack propagation rate throughout the test. To accomplish this, the stress intensity factor range, ΔK, was chosen as the design criteria. ΔK represents the change of stress state in one load cycle around the crack tip, hence governs the crack propagation rate.

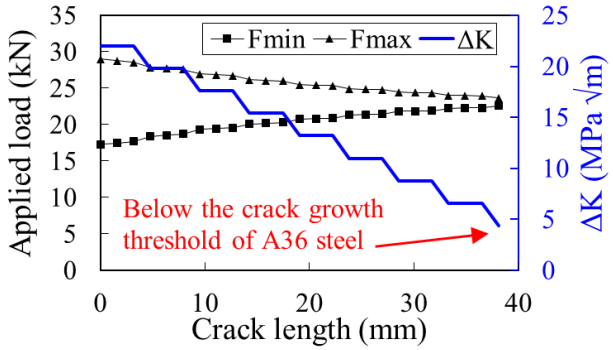

Figure 27. Loading protocol.

As shown in Figure 27, an initial ΔK = 22.0 MPa√m (20 ksi√in.) was assigned at the beginning of the test. Each time the crack propagated an additional 4.8 mm (3/16 in.), as visually identified by the measuring tape, ΔK was decreased by 2.2 MPa√m (2 ksi√in.). As a result, ΔK

was incrementally decreased while the crack propagated, generating a decreasing crack propagation rate. Ultimately, the crack was expected to stop growing when ΔK dropped to 4.4 MPa√m (4 ksi√in.), which is below the crack growth threshold of the A36 steel.

Once the relation of ΔK versus crack length was determined, the corresponding F_{max} and F_{min} of the load cycles was calculated using the recommended method in the ASTM E1820 (ASTM 2015). The stress intensity ratio $R = F_{min} / F_{max}$ was also induced in this calculation, and its initial value was set as 0.6. The resulting F_{max} and F_{min} were equal to 29 kN (6.52 kip) and 17.3 kN (3.88 kip), respectively at the beginning of the test. The mean load, $F_{mean} = 0.5 \times (F_{max} + F_{min})$, was maintained as 23.1 kN (5.2 kip) throughout the fatigue test.

4.6.3 Traffic load cycles design

When designing the traffic loading protocol for the laboratory test, the goal was to mimic features of realistic traffic loads in steel highway bridges. The stochastic nature of the peak-to-peak amplitude and period are two important characteristics of traffic load cycles. In steel highway bridges, the peak-to-peak amplitude is governed by vehicle weight. Lu et al. (2012) found that among all type of vehicles, only fully-loaded heavy trucks were critical for fatigue crack propagation, while excitation forces from lighter-weight vehicles were below the threshold of fatigue crack growth. Vrouwenvelder and Waarts (1993) measured 16,000 vehicles in the Netherlands in the 1970s and found the weights of fully-loaded heavy trucks followed normal distributions with coefficients of variation (COVs) from 0.12 to 0.22, depending on specific truck types. To simplify the laboratory loading, only one type of fully-loaded truck was considered in this study, and the peak-to-peak amplitude of load cycles was taken to have a normal distribution with a COV = 0.13.

The period of traffic load cycles, on the other hand, is governed by bridge geometric configuration such as span length, and vehicle speed. For a specific steel highway bridge with known geometric configurations, vehicle speed becomes the only factor that affects the loading period. Different statistical distributions have been reported for highway vehicle speed, including bimodal distribution (Dey et al. 2006), normal distribution (McLean 1978), and gamma distribution (Haight and Mosher 1962). In this study, the period of traffic load cycles was assigned a normal distribution. The mean period was taken as 2.49 sec, while the COV of the period was taken as 0.20.

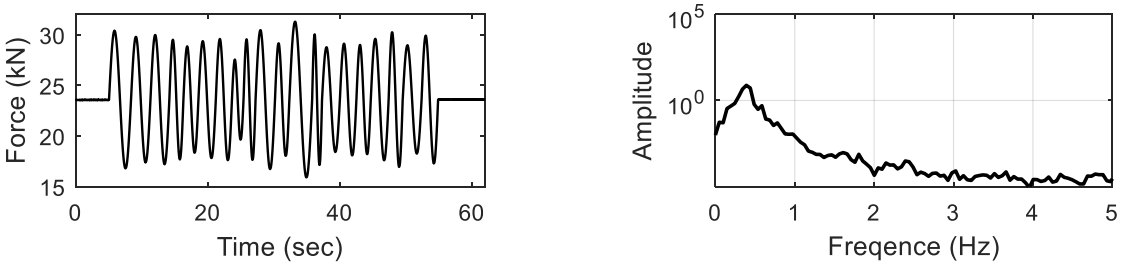

(a) (b)

Figure 28. (a) Generated traffic load cycles with stochastic amplitude and period; and (b) PSD of traffic load cycles.

Figure 27a shows the generated traffic load cycles for the beginning of the test. In total 20 cycles were generated following the previously-determined statistical distributions of peak-to-peak amplitude and period. The generated waveform was combined with the load range, F_{max} and F_{min} shown in Figure 27, to produce the final traffic load for the whole test. The corresponding power spectral density (PSD) of the generated load cycles is illustrated in Figure 27b. Instead of a single dominant peak at the loading frequency, which was the case for the previous harmonic load cycles, a wide plateau can be observed around 0.5 Hz due to the variation of frequency content in the time series of loading signal.

4.6.4 Crack sensing algorithm

The crack sensing algorithm for harmonic load cycles was modified for the case of traffic load cycles. A moving-average filter (i.e. low-pass filter) was applied to smooth the PSD curves as shown in Figure 29. The PSD curves of the applied load $F_T(t)$ and capacitance measurement $C_T(t)$ both exhibited a broad-band feature due to multiple frequency contents in the traffic load cycles. To obtain robust results, the moving-average filter is necessary to smooth the PSD curves. With adequate order of the filter, flat plateaus can be achieved and the magnitudes of the flat plateaus ($Peak_C$ and $Peak_F$) are adopted for computing the *CGI*.

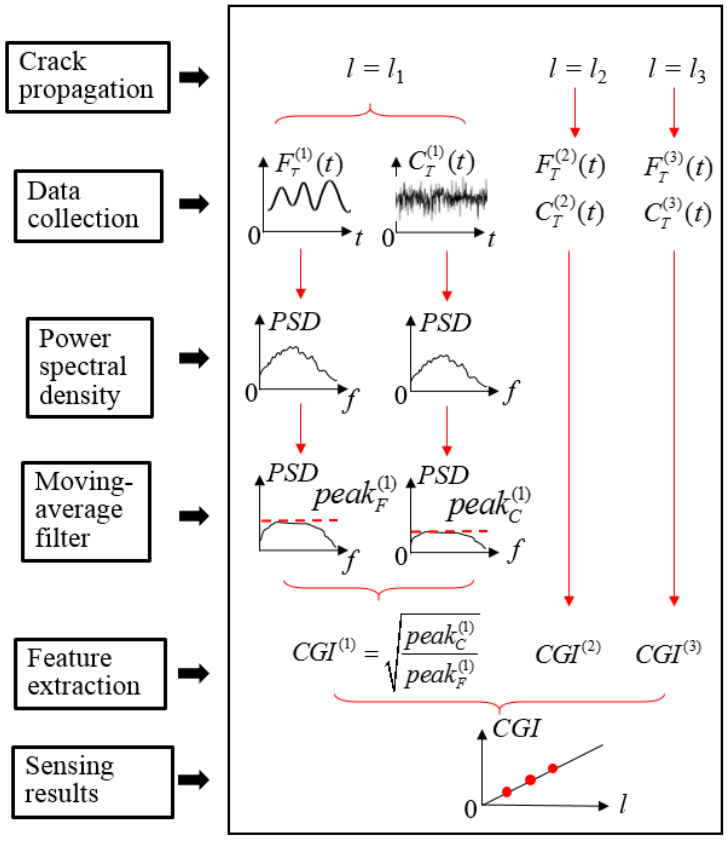

Figure 29. Crack sensing algorithm

4.6.5 Crack growth characteristics

Under the aforementioned test setup with the newly-designed loading protocol, the experimental test was conducted in the Fatigue and Fracture Laboratory at the University of Kansas. During the test, the number of cycles for propagating the crack each additional 1.6 mm (1/16 in.) was recorded. This information was converted to the crack propagation rate in terms of d*a*/d*N* (increment of crack length per load cycle). Table 4 summarizes typical crack propagation rates and number of cycles under each ΔK throughout the test.

Table 4. Crack growth characteristics

ΔK	**Number of cycles (million)**	**Crack length**	**da/dN**	**Remark**
22.0 MPa √ m (20 ksi √ in.)	0.08	3.2 mm (1/8 in.)	8.0×10^{-5} mm/cycle (3.13×10^{-6} in./cycle)	Decreasing crack propagation rate
15.4 MPa √ m (14 ksi √ in.)	0.27	15.9mm (5/8 in.)	3.2×10^{-5} mm/cycle (1.25×10^{-6} in./cycle)	
11.0 MPa √ m (10 ksi √ in.)	0.79	27.0 mm (1-1/16 in.)	1.6×10^{-5} mm/cycle (6.25×10^{-7} in./cycle)	
6.6 MPa √ m (6 ksi √ in.)	4.73	38.1 mm (1-1/2 in.)	2.0×10^{-6} mm/cycle (7.81×10^{-8} in./cycle)	
4.4 MPa √ m (4 ksi √ in.)	6.37	38.1 mm (1-1/2 in.)	0	Crack propagation stopped

The crack propagation rate, d*a*/d*N*, was found to be 8.0×10^{-5} mm/cycle ($3.13\text{x}10^{-6}$ in./cycle) at the beginning of the test when ΔK = 22.0 MPa√m (20 ksi√in.), after which it decreased as the crack propagated. Then the crack length reached 38.1 mm (1-1/2 in.) when ΔK = 6.6 MPa√m (6 ksi√in.), d*a*/d*N* became 2.0×10^{-6} mm/cycle ($7.81\text{x}10^{-8}$ in./cycle), which was significantly lower than the initial crack propagation rate. A total of 4.73 million cycles had been applied to the specimen at this point. ΔK was then further reduced to 4.4 MPa√m (4 ksi√in.), and the crack propagation rate was found to be extremely low, after which the crack stopped growing.

These observations indicate that the newly designed loading protocol successfully generated a varying crack propagation rate in the fatigue test.

To evaluate whether the SEC would produce a false-positive result, five additional measurements, taken at increments of 0.2 million load cycles, were recorded under harmonic load cycles. Figure 30 shows a photograph when the crack reached 38.1 mm. Despite the visible crack opening shown in the photograph, the crack propagation rate was extremely slow at this point because ΔK had decreased below the crack growth threshold for A36 steel.

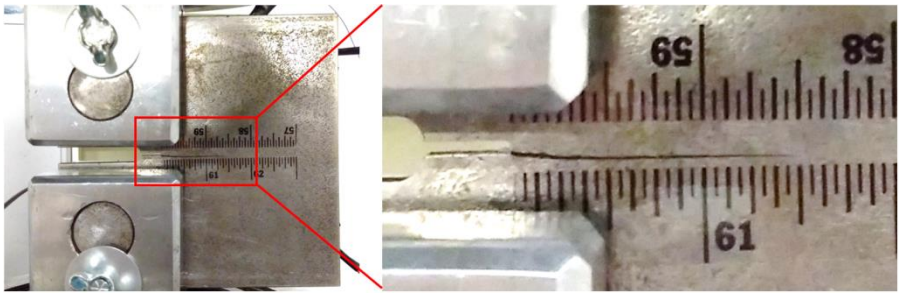

Figure 30. The fatigue crack developed in the specimen

4.6.6 *CGI* Extraction and Crack Sensing Results

By following the proposed crack sensing algorithm shown in Figure 29, the *CGIs* can be extracted from the measurements taken at different crack lengths. Figure 31 shows the *CGIs* under both harmonic and traffic load cycles.

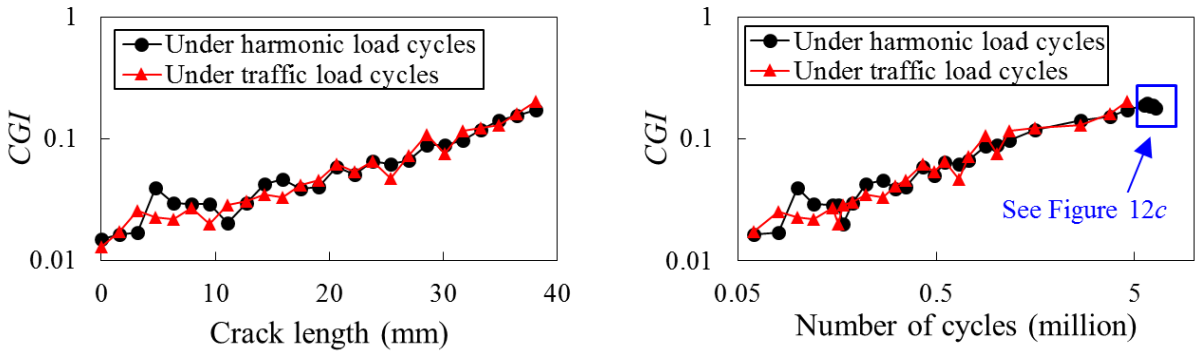

(a) (b)

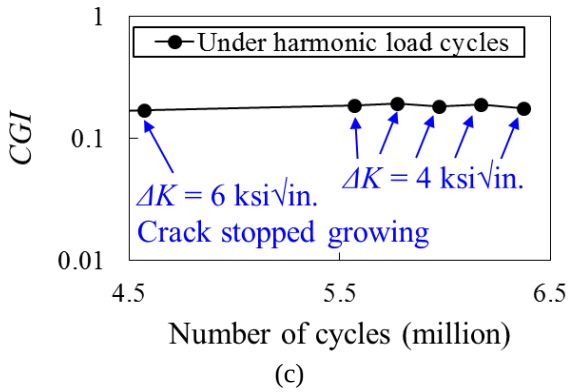

(c)

Figure 31. (a) *CGI* vs. crack length; (b) *CGI* vs. number of cycles; and (c) *CGI* when the crack stops growing

Figure 31a illustrates *CGI* versus crack length. The crack length was measured from the notch of the C(T) specimen. In general, the *CGIs* under both harmonic and traffic load cycles have a similar increasing trend. The lowest *CGI* occurred at the beginning of the test when the crack length was 0 mm, after which *CGI* gradually increased as the crack grew longer. This result validates the SEC's ability to detect fatigue crack initiation and monitoring crack propagation, regardless the loading scenarios. In particular, the SEC and its data processing algorithm remained effective under 20 traffic load cycles with random peak-to-peak amplitudes and periods.

Figure 31b shows *CGI* versus the number of load cycles, in which the number of cycles is shown in log scale. As described previously, the crack propagation rate continuously decreased during crack propagation. The same behavior was also observed in the *CGI*, which increased rapidly at the beginning of the test but slowed after approximately 1 million cycles. Importantly, the *CGI* continued exhibiting an increasing trend toward the end of the test during the period of extremely low crack propagation rate. This result demonstrates the crack monitoring capability of the SEC under a varying crack propagation rate.

Finally, CGIs of the five measurements taken under harmonic load cycles after the crack growth had stopped at 38.1 mm (1-1/2 in.) are marked in Figure 31b, with the details shown in Figure 31c. The CGI remained stable during the additional 1.8 million load cycles applied to the specimen, indicating that the SEC does not produce false-positive results when the crack is not growing.

4.7 Conclusions

This chapter has presented a study that was focused on examining the suitability of a novel large-area strain-based sensing technology for monitoring fatigue cracking in steel bridges. The SEC is a large-size, flexible, low-cost, and mechanically-robust capacitive strain gage, and has a wide strain measuring range, making it a promising tool for monitoring cracking in bridges. Previous studies have verified the SEC's capabilities for monitoring low-cycle fatigue cracking, but high-cycle fatigue cracking is characterized by small crack openings, which presents a new challenge for a capacitance-based sensor such as the SEC. To achieve a monitoring solution for fatigue cracking in steel bridges, the pk-pk amplitude of the sensor's measurement was used to construct an indicator of crack growth. Then, a crack monitoring algorithm was established to compute *CGIs* as a normalized pk-pk amplitude in frequency domain. The sensor's capabilities and the proposed algorithm were evaluated through experimental testing under various stress ratios, *R*. The following conclusions were drawn:

- The developed algorithm was able to overcome noise infiltration, and resulted in excellent correlation between increasing fatigue crack length and increasing *CGI*. Therefore, the proposed crack monitoring algorithm was validated by the test data.

- The proposed crack monitoring algorithm was able to robustly monitor the growth of high-cycle fatigue cracks under various loading conditions, and provided consistent results for the three stress ratios that were studied.
- With the introduction of the monitoring algorithm, the SEC was found to be capable of serving as a monitoring device for propagating fatigue cracks in steel bridges.

In addition, the emphasis was placed on performance evaluation of the SEC applied over a fatigue crack with varying propagation rates and random traffic load cycles. To facilitate the investigation, we developed an experimental methodology including three components: 1) An efficient data collection strategy was developed by taking multiple short-time measurements during crack propagation, and then extracting crack growth features, the *CGIs*, to monitor fatigue crack growth in a long-term fashion; 2) A new loading protocol was developed for generating a fatigue crack with decreasing crack propagation rates, and random load cycles that can reflect realistic stochastic features of traffic load of steel highway bridges; and 3) Crack sensing algorithms based on frequency analysis was developed to extract *CGIs* under harmonic and traffic load cycles.

Experimental results showed an increasing trend of *CGI* during the process of crack initiation and propagation, despite continuously decreasing crack propagation rate or random traffic load cycles. Furthermore, the SEC produced constant *CGIs* after the crack stopped growing, indicating no false-positive results. Results of this study verified the capability of the SEC to detect and monitor fatigue cracks under more complex and realistic loading conditions, which is a critical step towards field applications of the technology.

The research reported in this chapter forms the basis for use of SECs as a robust fatigue monitoring solution in steel bridges. Development of such a monitoring solution is highly

impactful, as the sensors themselves are large and can cover large areas in fatigue-susceptible regions of steel bridges, leading to more reliable and comprehensive long-term fatigue monitoring solutions.

Chapter 5: Large-Scale Experimental Investigation of Soft Elastomeric Capacitors for Fatigue Crack Monitoring

This chapter is modified based on the following journal publication:

Kong, X., Li, J., Collins, W., Bennett, C., Laflamme, S., & Jo, H. (2018). Sensing distortion-induced fatigue cracks in steel bridges with capacitive skin sensor arrays. *Smart Materials and Structures*, In press

5.1 Overview

In this chapter, we investigated the SEC's crack monitoring performance on bridge girder to cross-frame connections subjected to distortion-induced fatigue. Multiple SECs were deployed over a large structural region to form an SEC array. A new fatigue damage sensing approach was then established in terms of crack growth index (CGI) map, which is a 2D image constructed by signals from the SEC array. The CGI map offers more comprehensive fatigue-related information about the monitored structural region than relying on discrete values from individual SECs. The effectiveness of the SEC array and the CGI map were validated through laboratory tests on scaled bridge girder to cross-frame connection models.

5.2 Background

This section introduces the background of this study including: a brief review of the mechanism of distortion-induced fatigue cracking, sensing principle of the SEC, and previous work on extracting fatigue sensitive features from SEC measurements.

5.2.1 Distortion-induced fatigue cracks

Figure 32 shows the mechanism of distortion-induced fatigue at web-gap regions in steel girder bridges built prior to the mid-1980s in the United States. Cross-frames and diaphragms are used to provide lateral stability to girders, as shown in a skewed bridge configuration in Figure 32(a). As illustrated in Figure 32(b), the traffic load *F* applied on top of Girder A leads to a differential vertical movement *Δ* between the two adjacent girders, which would in turn provoke an out-of-plane bending moment at the top web-gap region in the adjacent girder (i.e. Girder B). This repetitive out-of-plane loading leads to the initiation and propagation of fatigue cracks. A more detailed discussion about the mechanism of distortion-induced fatigue cracks can be found in (Jajich and Schultz, 2003).

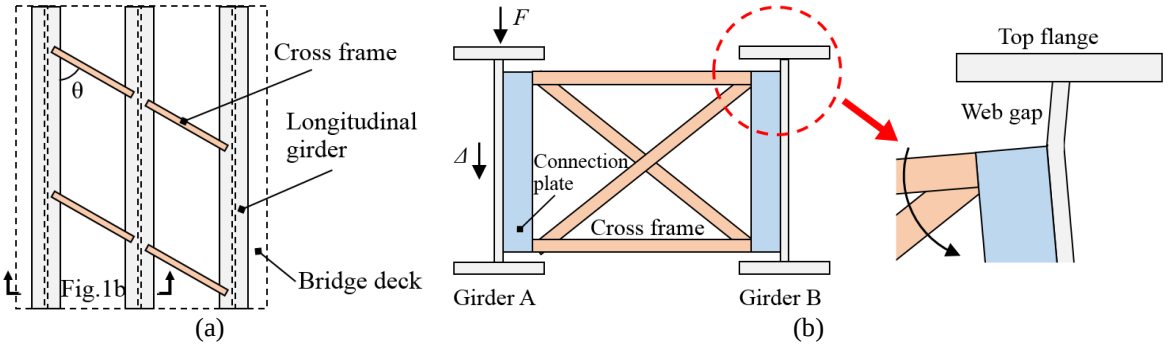

Figure 32. Schematic of a girder bridge under traffic load: (a) plan view; and (b) elevation view and detail of the web-gap region.

Figure 33(a) is a photo that illustrates a common structural layout of a steel highway girder bridge. Many fatigue cracks have been identified at the web-gap region in this bridge during routine bridge inspections. Figure 33(b) shows a typical example where Crack A was found between the top flange and web, while Crack B initiated at the top end of the fillet weld between the connection plate and the web. Depending on the skew angle of the cross frame (denoted as *θ* in Figure 32(a)), Crack B could propagate into the web region, or grow along the fillet weld between the connection plate and the web.

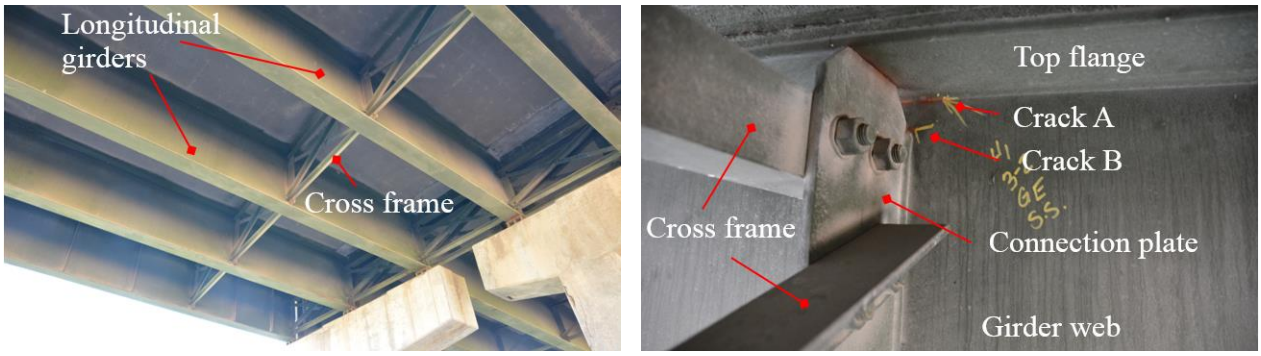

(a) (b)

Figure 33. (a) A typical structural layout of a steel girder bridge in the field; and (b) representative distortion-induced fatigue cracks at the web-gap region.

5.2.2 Soft elastomeric capacitor

The SEC technology is described in detail in (Laflamme et al. 2012). Briefly, as shown Figure 14(a), the SEC is a large-area capacitor consisting of a dielectric layer sandwiched between two conductive layers. The two sizes of SECs adopted in this study (Figure 14(b)) are 76.2 mm by 76.2 mm (3 in. by 3 in.) and 38.1 mm by 38.1 mm (1.5 in. by 1.5 in.), with respective nominal capacitance values of approximately 900 pF and 150 pF. Two copper tapes were adhered onto both conductive layers for measuring capacitance of the sensor.

Equation 1 shows the sensing principle of the sensor, where C is the capacitance of the SEC, ε_0 and ε_r are the vacuum and polymer relative permittivity, respectively, and l, w and h are the length, width, and thickness of the SEC (Figure 14(a)), respectively. A change in surface strain on the monitored surface will provoke a change in the geometry of the SEC (i.e. l, w, and h), hence changing the capacitance C.

$$C = \frac{\varepsilon_0 \varepsilon_r l w}{h} \tag{1}$$

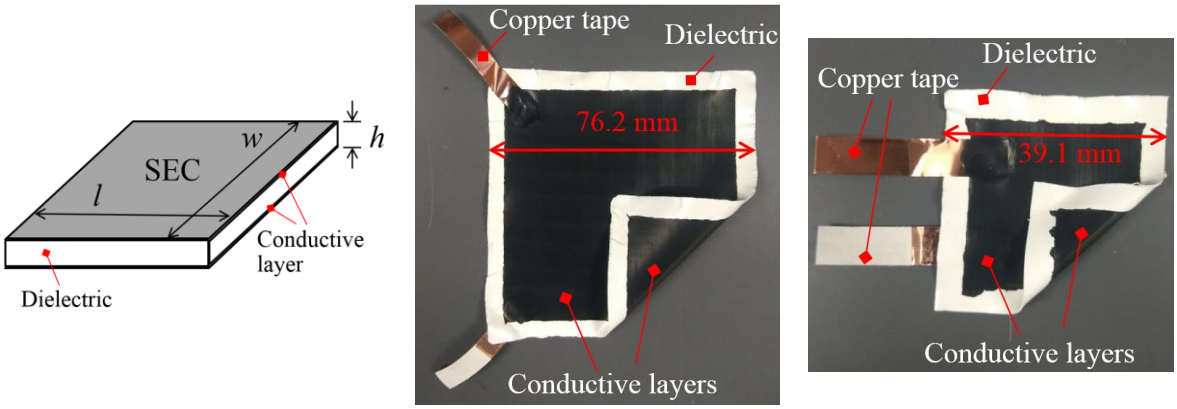

(a) (b) (c)

Figure 34. (a) Schematic of the SEC; (b) photo of an SEC of dimension 76.2 mm by 76.2 mm; (c) photo of an SEC of dimension 39.1 mm by 39.1 mm.

5.2.3 Crack growth index

Previous work (Kong et al. 2017a; 2018e; 2018f) proposed and demonstrated a crack detection and monitoring algorithm by extracting a crack-sensitive feature, termed the crack growth index (CGI), from the SEC's capacitance measurements. This feature extraction method is briefly reviewed here as it serves as the basis for constructing the CGI map to be introduced in Section 5.2.4.

Figure 35(a) shows the procedure for computing CGI. In the figure, a fatigue crack in a steel plate is generated by the fatigue load *F*. An SEC is deployed onto the steel plate to monitor the crack activity. A previous investigation (Kong et al. 2017a) verified that the peak-to-peak amplitude of capacitance (denote in Figure 35(a)) of the SEC is a robust indicator for fatigue crack growth. In general, peak-to-peak capacitance increases when the crack propagates due to the reduction of local stiffness around the crack. However, the SEC's signal usually contains noise. Directly identifying the peak-to-peak capacitance from a time-series measurement is challenging. Hence, the power spectral density (PSD) is computed to convert time-series measurement into the frequency domain. The PSD curve represents the energy distribution of the

time-series signal, and the peak around the dominant loading frequency (denote as $peak_C$ in Figure 35(a)) can robustly indicate the peak-to-peak capacitance.

The magnitude of the applied load F is also required for CGI extraction. This is because the load range (denote as Amp_F in Figure 35(a)) also directly affects the peak-to-peak capacitance of the SEC. A larger load range would induce higher capacitance response even if the crack does not grow. Hence, the capacitance response needs to be normalized with respect to the load range, which leads to the equation $CGI = \sqrt{peak_C} / Amp_F$. The applied fatigue load can either be directly measured from the actuator in a laboratory setting or indirectly inferred via strain measurements in practical applications.

Once the CGI is extracted from one set of short measurements, crack growth can be monitored through a long-term monitoring strategy as illustrated in Figure 35b. Briefly, a series of short-time measurements of the applied load F and capacitance response C are collected during the fatigue life of the steel plate. If the crack grows between the data collection intervals, the extracted CGI would increase. By collecting the CGIs through repeated measurements over time, the fatigue crack growth can be monitored. It should be noted that the absolute value of CGI is also governed by the type of normalizer. The normalization procedure for computing CGIs could be based on the applied load from the actuator in the laboratory or the strain measurement from the strain gauge installed in the steel bridge. Therefore, directly comparing CGIs from different test set-ups or normalizers is not meaningful. However, for a predetermined test set-up with a fixed normalizer, the relative change of CGIs (i.e. the increasing trend in Figure 35b) is a robust indicator of fatigue crack growth.

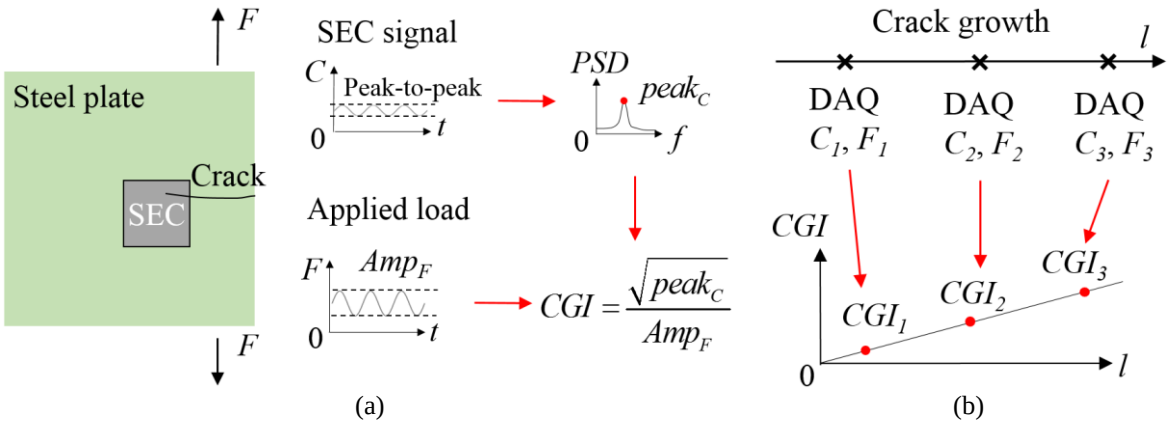

(a) (b)

Figure 35. (a) Methodology for extracting CGI from a single dataset; and (b) correlating CGI with crack lengths based on multiple datasets. DAQ in Figure 35b represents data acquisition.

5.3 Methodology

Previous research has focused on the examination of a single SEC on a small-scale specimen with an in-plane fatigue crack. The method of CGI extraction reviewed in Section 5.2.3 was developed for single SEC utilization. However, for sensing distortion-induced fatigue cracks in steel bridges, an array of SECs is adopted in this study to cover a larger fatigue-susceptible region. As the number of SECs increases in this application, measurements from the SEC array result in multiple CGIs. Investigating the CGI change for each individual SEC against different crack lengths would be time-consuming and less informative. A better approach is to spatially visualize all CGIs of the SEC array over the fatigue-susceptible region. We do so by extending the CGI index to a CGI map to visually represent the spatial distribution of CGIs.

5.3.1 CGI map

Figure 36 illustrates the methodology for constructing a CGI map. An array of SECs was deployed on a steel plate to monitor the crack growth, and CGI①, CGI②, CGI③, and CGI④ are the CGI values for each individual SEC (Figure 36(a)). Where a crack propagates under an SEC (e.g. SEC①, SEC②, and SEC④ in Figure 36(a)), the CGI is a direct indicator of crack growth. On the other hand, where the crack does not grow under an SEC (e.g. SEC③ in Figure 36a), the

SEC serves as a large-area strain gauge for monitoring migration of the strain field caused by the crack growth.

Next, the CGIs of the four SECs in Figure 36(a) were mapped to a 3D coordinate system where the vertical axis is the magnitude of CGI and the two horizontal axes represent the plane of the structural surface. The CGIs are placed at the centroid of each SEC as shown in Figure 36(b). Subsequently, a 3D CGI surface was created using linear interpolation. The 3D CGI surface is a matrix that contains the interpolated CGIs over the zone defined by the four centroids of the SEC array. Finally, by projecting the CGI surface to the structural surface, the 2D image, termed the CGI map, can be constructed as illustrated in Figure 36c.

By constructing a series of CGI maps based on multiple measurements from the SEC array at different crack lengths, fatigue damage in a large region can be monitored. If the fatigue crack does not grow during the data collection intervals, the corresponding CGI maps would exhibit a similar intensity distribution. Conversely, fatigue crack propagation would provoke intensity changes in the CGI maps, which serve as good features for fatigue damage monitoring.

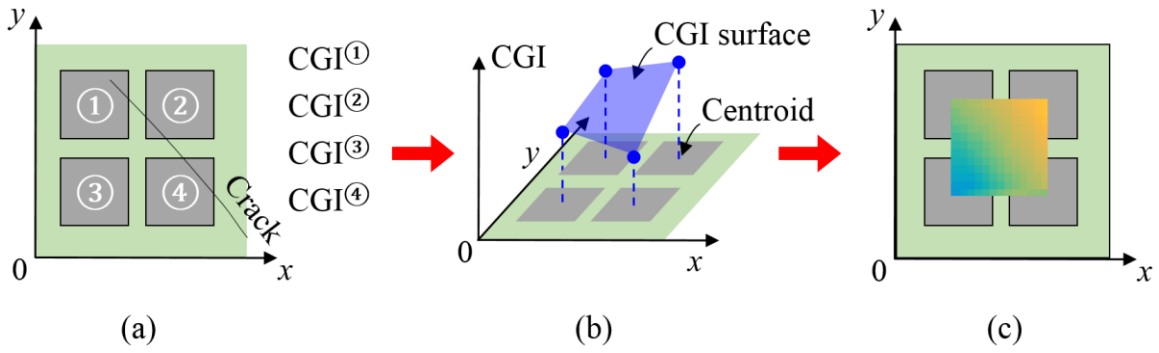

Figure 36. (a) Methodology for constructing CGI map: (a) individual CGIs from an SEC array; (b) a CGI surface through linear interpolation; and (c) CGI map. The SECs in Figure 36(a) and (b) are illustrated as transparent for illustration purpose.

5.3.2 Special considerations for distortion-induced fatigue cracks

Section 5.3.1 presented the methodology for constructing CGI maps through a steel plate under an in-plane fatigue crack. However, distortion-induced fatigue cracks in steel bridges usually

initiate and propagate along complex paths, as they are subjected to multi-directional states of stress that can vary significantly within the web gap region. As illustrated in Figure 33(b), distortion-induced fatigue cracks may initiate between the girder web and top flange (e.g. Crack A), or between the connection plate and girder web (e.g. Crack B). In both cases, cracking initiates at the weld toe between two adjacent structural components. Furthermore, depending on the structural geometric layout, the crack may continue to grow along the weld. Hence, special considerations are needed for detecting distortion-induced fatigue cracks.

Previous studies (Kong et al. 2017a; 2017b) validated that the SEC can effectively sense in-plane fatigue damage if the crack directly propagates under the sensing skin. However, to detect a distortion-induced fatigue crack that grows along the weld, the SEC may need to be deployed in a folded configuration. For instance, an SEC should be folded to cover both the connection plate and the girder web to detect Crack B shown in Figure 33(b).

5.4. Experimental configuration

5.4.1 Description of the test set-up

A bridge girder to cross-frame connection was adopted for the experimental tests in this study, as shown in Figure 37. To simulate the restraint provided to the top flange of a bridge girder by the deck in the field, the bridge girder was mounted upside-down to the strong floor in the laboratory to constrain the bottom flange of the girder. A cross frame was then installed to the girder through a connection plate. The skew angle θ between the cross frame and the girder was 40 degrees as shown in Figure 37(b). To represent the structural layout of typical girder bridges built prior to the 1980s, the connection plate (Figure 37(c)) was only fillet welded to the girder web while the top and bottom of the connection plate were not attached to the flanges. A detailed description of the test specimen can be found in (Yu et al. 2017).

To apply fatigue load cycles, an actuator was vertically attached to the far end of the cross frame. The actuator was restrained from moving laterally (Figure 37(a)) so that it could only move in the vertical direction and apply vertical load to the cross frame. A 0.5 Hz harmonic load was adopted and a load range of -4.9 kN (1.1 kip) to 4.9 kN (1.1 kip) was applied.

As mentioned in Section 5.2.3, the amplitude of the applied load is required for extracting the CGI from the SEC's capacitance measurement. For this purpose, a strain gauge was installed on the top horizontal cross frame member (Figure 37(b)) to indirectly infer the amplitude of applied load during the test. A similar strategy could be applied in field applications where the true fatigue load caused by passing vehicles cannot be easily measured.

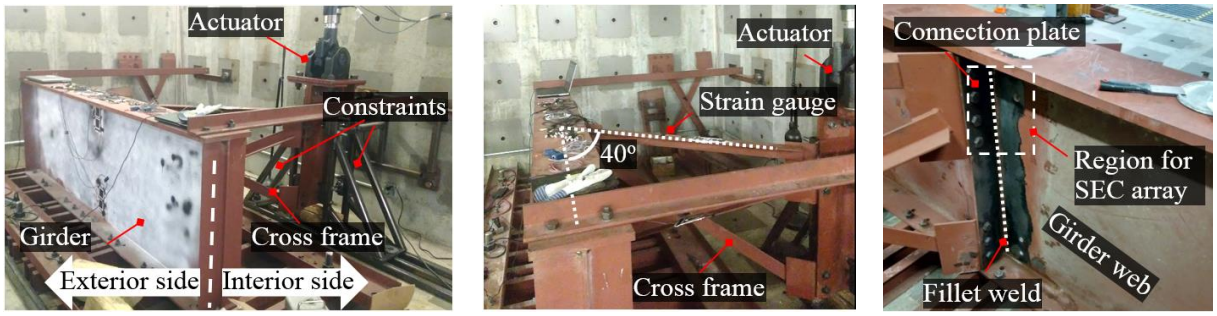

(a) (b) (c)

Figure 37. (a) Exterior view of the test model; (b) interior view of the test model; and (c) detailed view of the connection plate. Figure 37(c) shows the specimen prior to installation of the SEC array.

5.4.2 Existing fatigue damage

Prior to this study, the test model had been fatigue loaded for 2.7 million cycles under a load range of 0 to 11.2 kN (2.5 kip). As a result, a fatigue crack existed at the interior side of the top web-gap region between the connection plate and the girder web. Due to the small opening of the fatigue crack, a fluorescent dye penetrant was used to accurately identify the locations of the crack tip. As shown in Figure 38, the length of the fatigue crack was measured as 19.1 mm (0.75 in.).

Figure 38(c) shows the detailed layout at the top web gap region of the connection model. The connection plate was not welded to the girder flange, leaving a gap between the flange and

connection plate, which was the primary reason for causing distortion-induced fatigue cracks as discussed in Section 5.2.1.

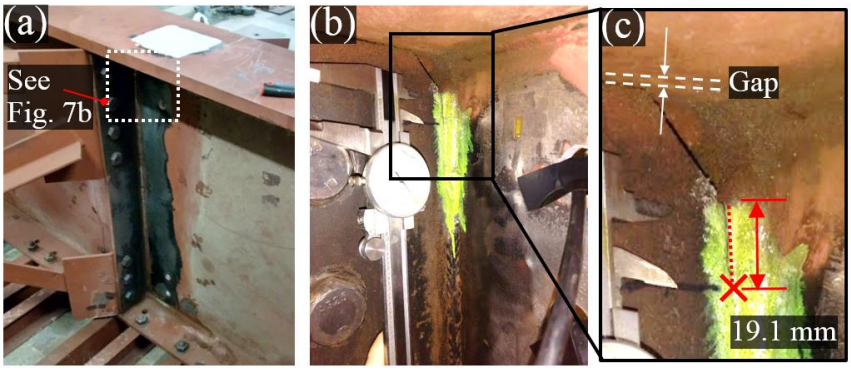

Figure 38. Existing fatigue damage in the connection model: (a) overview; (b) fatigue crack at the top region of the connection; and (c) detailed look of Figure 38(b).

5.4.3 Deployment of an SEC array

To detect and monitor distortion-induced fatigue damage in the test girder, an SEC array was deployed at the top web-gap region, as shown in Figure 39(a). SECs with dimensions 76.2 mm x 76.2 mm (3 in. x 3 in.) are termed large SECs, while those with dimensions 38.1 mm x 38.1 mm (1.5 in. x 1.5 in.) are termed small SECs. A total of 11 SECs were deployed on the structural surface using a bi-component epoxy (JB Weld). Figure 39(b) schematizes the sensor layout. Folded SECs (i.e. SEC a1, a5, and a10) were deployed along the weld to detect crack growth at the weld toes. Flat SECs, on the other hand, were intended to serve as large-area strain gauges to sense the strain field migration caused by cracking activity. An off-the-shelf data acquisition (DAQ) system (ACAM PCAP02) was used to collect the capacitance measurements of the SEC array.

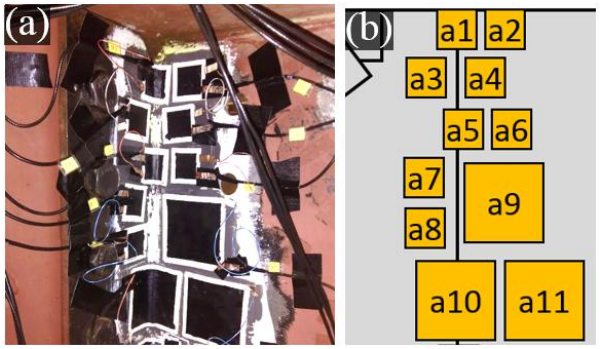

Figure 39. (a) SEC array arrangement; and (b) a schematic of the sensor layout.

5.4.4 Experimental procedure

During the test, 130,000 new load cycles were applied to the test girder under the load range of -4.9 kN (-1.1 kip) to +4.9 kN (+1.1 kip). A total of 13 datasets were collected at cycle counts of 0, 15,000, 21,500, 30,000, 43,100, 53,800, 64,900, 79,200, 93,000, 101,300, 110,000, 121,000, and 130,000. Each dataset contained both capacitance measurements from the SEC array and the strain gauge collected over 2-min periods, sampled at 50 Hz and 2000 Hz, respectively. During the test, four inspections were performed to identify crack lengths at cycle counts of 0, 71,000, 101,300, and 130,000 cycles, respectively.

Figure 40(a) presents a photograph of the specimen at the end of the test, in which some of the SECs were removed to clearly identify the crack tip. The locations of the crack tips identified from the four inspections are marked in Figure 40(a) and (b). The length of the crack was measured from the top end of the weld, as annotated in Figure 40(a). Crack lengths were approximately 19 mm (0.8 in.), 42 mm (1.7 in.), 62 mm (2.5 in.), and 84 mm (3.3 in.), respectively at the time of the four inspections. This result indicates how the fatigue crack propagated over the 13 data collection intervals.

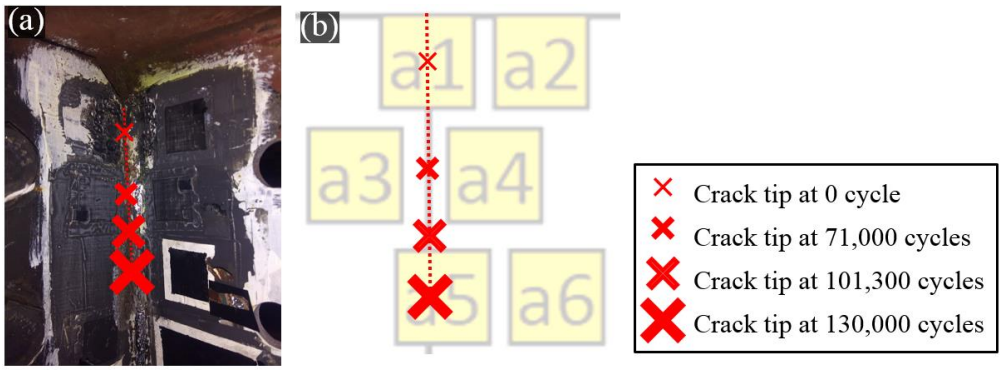

Figure 40. (a) Locations of the crack tips at different cycle counts; and (b) illustration of crack tips with respect to the sensor layout.

SEC a1 was removed after 79,200 load cycles, shown in Figure 41. The bonded side (i.e. the side in direct contact with the steel surface) of SEC a1 experienced damage during loading. In particular, a crack was identified in the conductive layer of SEC a1, exposing a white line that revealed the dielectric layer. This crack in the SEC was attributed to the large out-of-plane crack opening displacement under the sensor that repeatedly stretched the sensing skin during the test. Despite the occurrence of the crack in the conductive layer, SEC a1 continued providing capacitance data as to be illustrated in Figure 44.

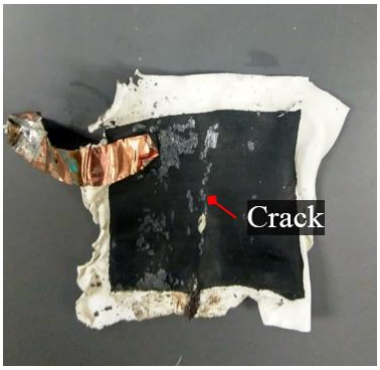

Figure 41. (a) SEC a1 was removed after 79,200 load cycles for a detailed inspection. On the bonded side (the side in direct contact with the steel surface) of the SEC, a crack was identified in the conductive layer, indicating damage to the SEC. The white color along the crack is the exposed dielectric layer.

5.5 Experimental results

5.5.1 Representative time-series measurements

Figure 42 presents a series of plots of representative time-series measurements of the SEC array taken from SECs a2 and a6. The plots present 10 seconds of measurements collected at 0 cycles (the beginning of the test) and 64,900 cycles. SEC a2 initially exhibited a larger peak-to-peak capacitance $\Delta C/C$ (Figure 42(a)), which became significantly smaller after 64,900 cycles (Figure 42(c)). This reduction may be attributed to the crack tip propagating away from SEC a2, causing strain relief around SEC a2 (Figure 40(b)). SEC a6, which was located in front of the crack propagation path, experienced an increased peak-to-peak capacitance, $\Delta C/C$, at 64900 cycles due to higher strain caused by the crack tip moving closer to the sensor.

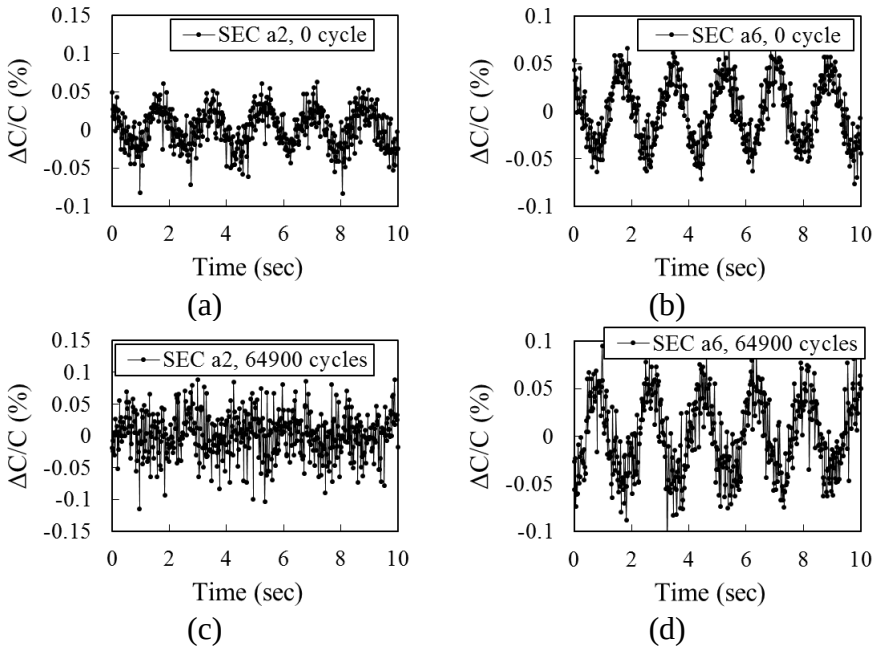

Figure 42. Representative time-series measurements from the SEC array. (a) SEC a2 at 0 cycle; (b) SEC a6 at 0 cycle; (c) SEC a2 at 64,900 cycles; and (d) SEC a6 at 64,900 cycles.

As discussed in Section 5.2.3, although peak-to-peak capacitance is a good indicator of fatigue crack growth, it is often times difficult to reliably identify in time-series signals due to the noise content. This can be observed in the signals plotted in Figure 42. Therefore, CGIs were extracted from the time-series signals through frequency analysis described in the next subsection.

5.5.2 CGIs from the SEC array

5.5.2.1 CGIs from the flat SECs

CGIs were extracted from the SEC array using the method introduced in Section 5.2.3. The strain measurement at the top chord of the cross frame was used to normalize the SEC measurements. Figure 43 shows the CGIs from the flat SECs at different numbers of load cycles. For clarity, results have been grouped based on the similarity of amplitude of CGI response.

As shown in Figure 43(a), CGIs from SEC a3 and a4 quickly increased at the beginning of the test and then gradually decreased. This phenomenon was a result of crack propagation which initially brought the crack tip closer to a3 and a4 during the first three datasets collected (0, 15,000, and 21,500 cycles). The stress concentration around the crack tip increased the responses of nearby sensors. As the crack propagated further and the crack tip moved beyond a3 and a4, the stress relief along the fatigue crack path led to a decrease in the responses of these two sensors after 21,500 cycles.

Figure 43(b) shows the CGIs from SECs a6, a7, a8, a9, and a11, in which increasing CGIs were observed for all SECs. This increasing trend was due to increases in the strain field at these SECs caused by crack growth. Figure 43(c) illustrates the CGI change for SEC a2. As the crack propagated downward, stress relief along the crack path led to a decreasing trend of CGI as shown in the figure. This behavior is corroborated by comparing time-series measurements

shown in Figure 42(a) and (c), in which the peak-to-peak capacitance decreased significantly at 64,900 cycles.

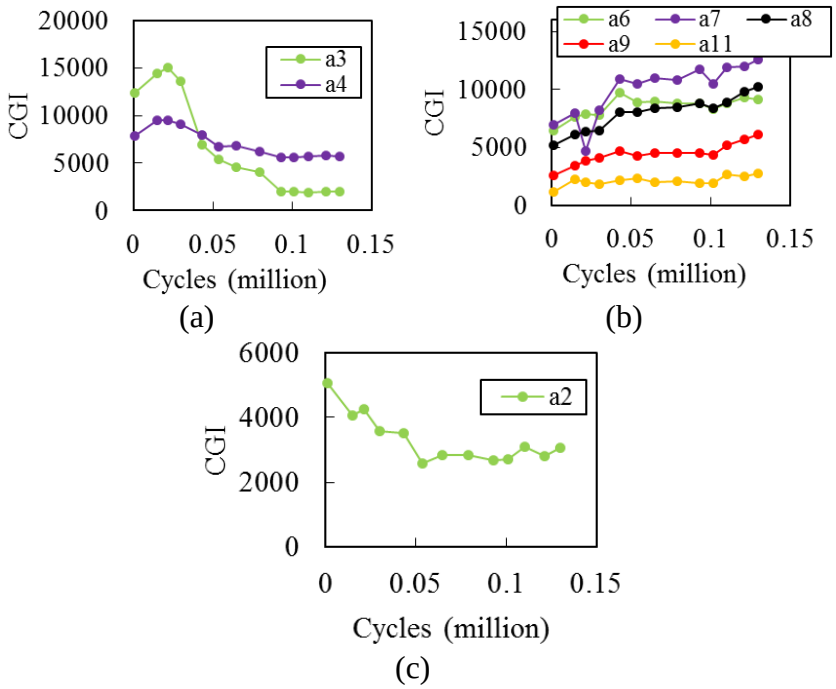

Figure 43. CGIs for (a) SEC a3 and a4; (b) SEC a6, a7, a8, a9, and a11; and (c) SEC a2.

5.5.2.2 CGIs from the folded SECs

SECs a1, a5, and a10 were folded at the corner between the connection plate and the girder web. CGIs from these three SECs have been plotted in Figure 44. Only eight datasets were collected for SEC a1, after which the sensor was removed for a detailed inspection (see discussion in Section 5.4.4). SEC a1 exhibited significantly higher CGI responses than the other SECs. In addition, the CGIs from SEC a1 exhibited fluctuations during the test. This behavior is caused by the damage occurring in the sensing material of SEC a1 (Figure 41) provoked by the distortion-induced fatigue cracking.

SEC a5 also exhibited much larger CGI responses than adjacent flat SECs. The initial CGI from SEC a5 was approximately 14,400 while the CGIs from SEC a6 and a7 were approximately 6,500 and 7,000, as shown in Figure 43(b). This is due to the relative rotation

between the connection plate and the girder web, which periodically stretches the sensing skin around the corner, provoking additional capacitance change to the SEC. In addition, the CGIs from SEC a5 (Figure 43b) steadily increased at the beginning of the test, and then decreased after 43,100 cycles. However, based on the observation illustrated in Figure 40(b), the fatigue crack reached SEC a5 at approximately 100,000 cycles and propagated to the center of SEC a5 at 130,000 cycles (end of the test). The CGI from SEC a5 continuously decreased during this stage despite the fact that the fatigue crack was growing under the sensing skin. A detailed discussion about the possible cause of this phenomenon can be found in Section 5.6.

Figure 44(c) shows the CGI from SEC a10, which is a folded sensor located far away from the fatigue crack. Large fluctuations were observed in the CGIs collected throughout the test from this SEC. The fluctuations may be attributed to the fact that SEC a10 was far away from the fatigue crack, and hence was less sensitive to the fatigue crack growth.

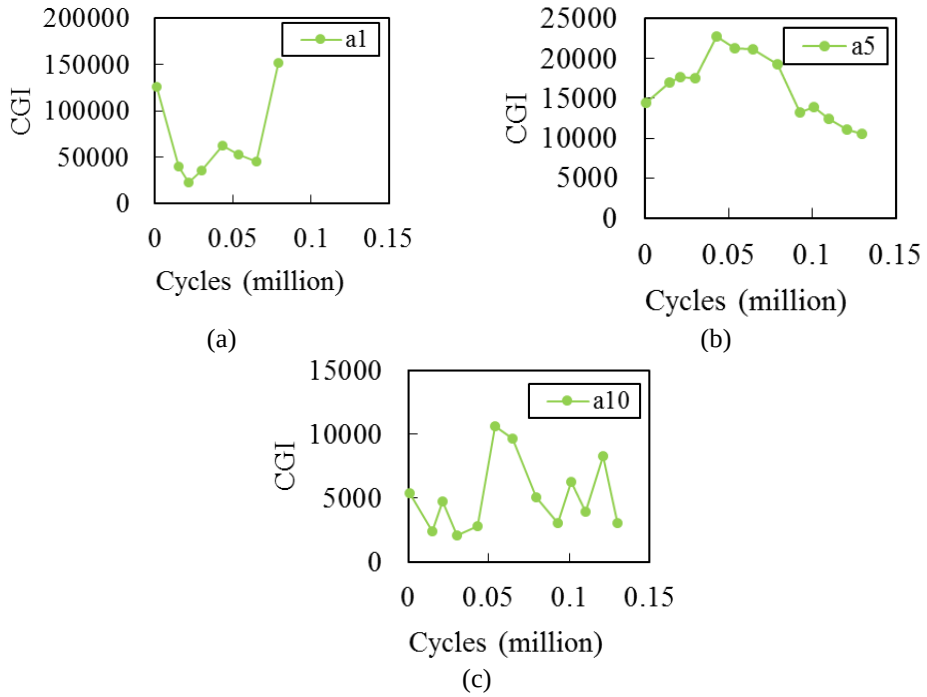

Figure 44. CGIs from (a) SEC a1; (b) SEC a5; (c) SEC a10

In summary, CGIs from folded SECs, initially deployed for directly detecting the crack growth, were unable to fulfil such a purpose (i.e. fluctuations of CGIs in SEC a1 and a10; decreasing CGIs when the crack grew into SEC a5). In this regard, only the flat SECs were adopted for constructing CGI maps, presented in the next subsection.

5.5.3 CGI maps

CGI maps were constructed using CGIs from the SEC array. Figure 45(a) illustrates the flat SECs used in constructing the CGI maps. The dashed lines represent the boundaries of the CGI maps. A 2D coordinate system was created where the origin was at the top of the weld. Figure 45(b) schematizes the 15 cm x 25 cm (6 in. x 10 in.) region used as the boundary for the plots shown in Figure 46.

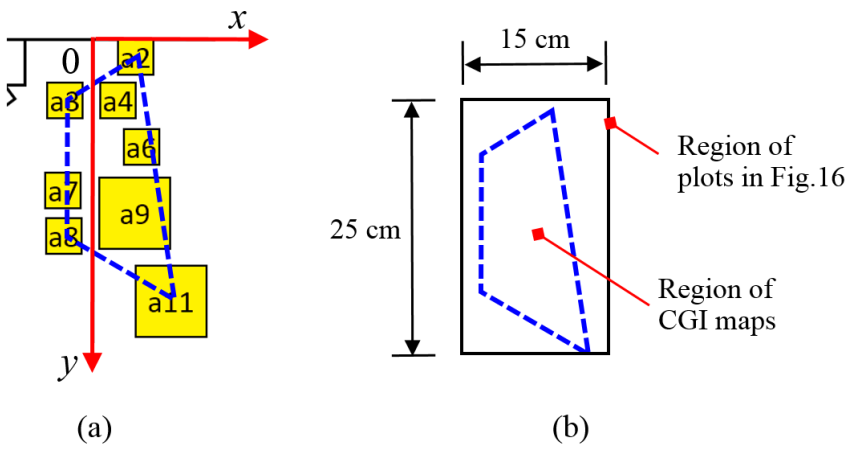

Figure 45. SECs for constructing the CGI maps.

Figure 46 shows the resulting CGI maps. Due to significant differences in magnitudes of CGIs (e.g. the CGI was as large as 15,000 for SEC a3, and approximately 2,000 for SEC a11), the intensity in the CGI maps is represented in logarithmic scale. The CGI map covers a large area of fatigue susceptible region (10 cm by 20 cm). The crack tip locations were identified multiple times during the test, which are also marked with white x's in Figure 46a, h, j and m.

Each plot in Figure 46 illustrates the distribution of CGI for the SEC array corresponding to each data collection interval, enabling a clear depiction of the fatigue damage over this large area. As the number of load cycles increases, the intensity in the CGI map changes. For instance, as the crack tip moved downward (shown in the progressions of Figure 46 (a) to (d)), higher intensities/brightness can be observed in the top-left region of the CGI map. However, as the crack continued to propagate, the top-left region became darker due to the stress relief along the crack path, as demonstrated in the progression shown in Figure 46e to h. The bottom-left corner of the CGI map became brighter during crack propagation, evident in a comparison of Figure 46h and m. This is due to the increasing strain field provoked by the propagation of the crack. By comparing the CGI map between the beginning and the end of the test (i.e. Figure 46 (a) and (m)), significant changes in the location of high CGI intensity can be observed, indicating the fatigue crack propagation behavior during these 13 data collection intervals.

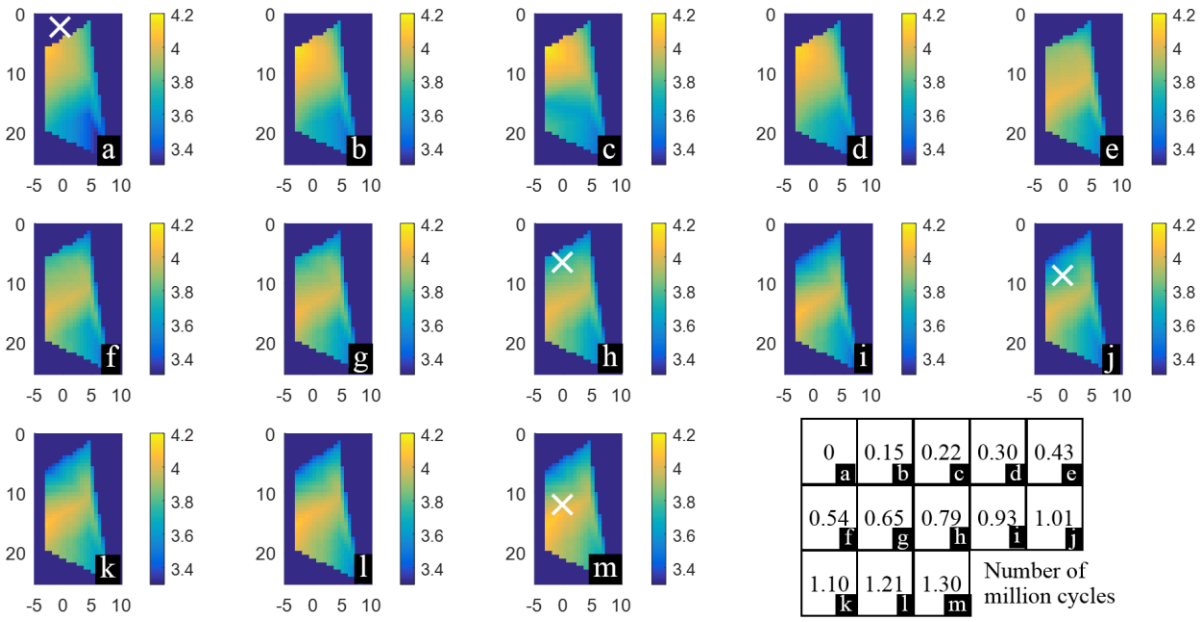

Figure 46. CGI maps at the top region of the connection under different load cycles. The 'x' at a, h, j and m indicate the locations of the crack tips observed during the test. The number of load cycles associated with each plot is shown at the bottom-right corner of this figure.

5.6 Further discussion on folded SEC sensors

This section investigates the potential source of the electromechanical behavior of the folded SEC a5 described in Section 5.2.2. SEC a5 was initially deployed for directly detecting the crack growth, but did not yield increasing CGIs when the crack propagated through the sensor. Figure 47 schematizes the layout of the test model, in which there is a skew angle of 40 degrees between the cross frame and the girder web. Due to the skewed configuration, the fatigue load F creates both a vertical movement of the cross frame and a horizontal rotation around the girder web, as illustrated in Figure 47b. Such a rotational movement could lead to a supplemental change in capacitance of the SEC folded between the connection plate and girder web. As a result, the folded SEC a5 is subject to a combined effect of crack propagation and cross frame rotation, which may have contributed to the behavior of SEC a5.

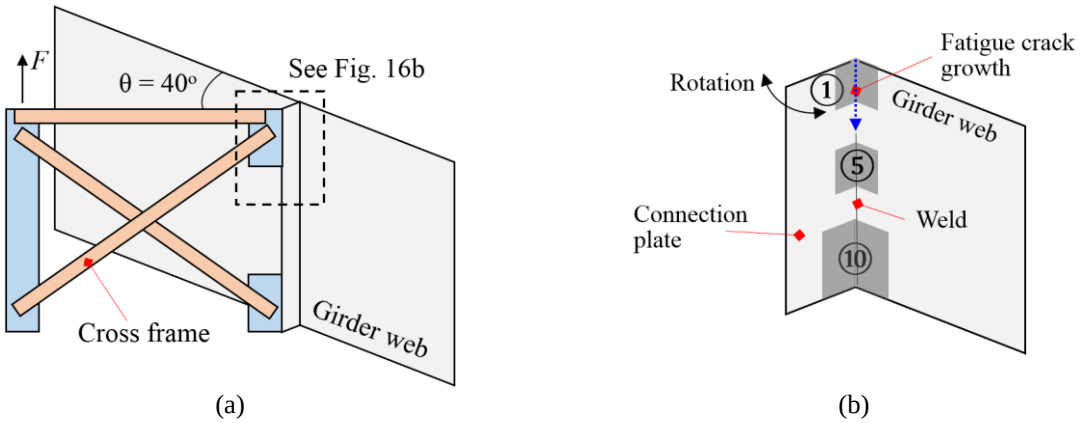

Figure 47. (a) An illustration of the rotation between the connection plate and the girder web in the tested model; and (b) inset detail at the top web gap (other SECs not shown for clarity).

To further validate this hypothesis, an additional experimental investigation was performed on a non-skewed bridge girder to cross frame connection model, as shown in Figure 48(a). This new model is similar to the skewed one described in section 5.4.1, except that the cross frame is perpendicular to the girder web, as denoted in Figure 48(a). The test model was symmetric about the cross frame. This non-skewed structural layout allowed the cross frame to

maintain the vertical movement under the fatigue loading without being subject to the horizontal rotation around the girder web.

(a) (b) (c) (d)

Figure 48. (a) Test set-up of the non-skewed bridge girder to cross frame connection; (b) SEC b1 at the bottom region of the connection (other SECs are note related with this study); (c) SEC b1 was removed for crack inspection after the fatigue test; and (d) crack inspection result.

An SEC, denoted SEC b1 in Figure 48(b), was deployed in folded configuration along the weld between the connection plate and the girder web. A foil strain gauge was installed on the top chord of the cross frame for normalizing the SEC's measurement. Prior to the test, the test model was inspected and no fatigue crack was detected. The test model was then fatigue loaded with 18,900 cycles with a load range of 2.2 kN to 25.5 kN (0.5 kip to 5.75 kip), leading to a newly-initiated fatigue crack beneath SEC b1. After the test, SEC b1 was removed to confirm the crack activity (Figure 48(c)). The fatigue crack is shown in Figure 48(d) under fluorescent dye penetrant.

During the test, 13 short time measurements of both the SEC and the strain gauge were collected for computing the CGIs. Utilizing the same CGI extraction method, CGIs of SEC b1 were computed and plotted in Figure 49. A clearly increasing trend of CGIs is observed in the figure, indicating SEC b1 was able to successfully monitor the crack growth, despite its folded configuration.

A comparison between the two tests with folded SECs under the skewed and non-skewed bridge configurations reveals that the rotational movement occurring between the girder web and

connection plate led to the inability of the folded SEC a5 to provide consistently increasing CGIs under crack propagation. When no such rotational movement is occurring, as it is the case for the non-skewed configuration, the folded SEC b1 was able to provide robust CGIs to monitor crack growth. Therefore, folded configuration of the SECs is only recommended to use in non-skewed bridge configurations or in ones with small skewness that have limited rotations.

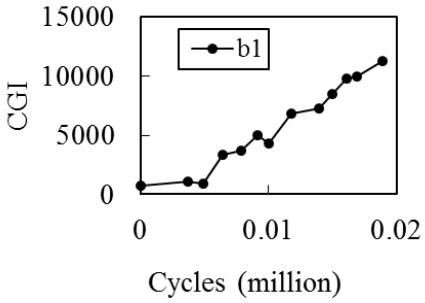

Figure 49. CGIs from SEC b1 in the non-skewed bridge girder to cross frame connection

5.7 Conclusions

This chapter presented a novel strain-based approach for sensing out-of-plane distortion-induced fatigue cracks in steel bridges using soft elastomeric capacitor (SEC) arrays. The SEC is a large-area and flexible sensing skin, able to measure a wide range of strains over large structural surfaces. Previous investigations have verified the ability of a single SEC for sensing an in-plane fatigue crack in a small-scale specimen. In this study, we further demonstrated the ability of the SEC technology in the context of sensing distortion-induced fatigue cracks, which represent the majority of fatigue cracks in aging steel highway girder bridges in the United States.

With the proposed strategy, multiple SECs in the form of a sensor array were deployed to cover a large fatigue-susceptible region. Subsequently, a fatigue sensing algorithm was proposed by constructing a crack growth index (CGI) map from the measurements of the SEC array. The effectiveness of the SEC array coupled with the CGI map was then experimentally validated

through a fatigue test of a bridge girder to cross-frame connection model subjected to distortion-induced fatigue. Test results verified that by deploying the SEC array, multiple CGIs can be obtained over the fatigue-susceptible region, offering a comprehensive picture of the fatigue damage. Furthermore, through monitoring the evolution of CGI maps constructed under different fatigue load cycles, the fatigue crack growth can be clearly visualized by identifying the intensity changes in the CGI maps.

Comparison between the skewed and non-skewed bridge configurations also indicated that the horizontal rotation between the connection plate and the girder web can affect the effectiveness of the folded SEC for directly monitoring crack growth along the corner of the connection. This observation provides an important guideline for applying the SECs in folded configuration in future field applications.

Chapter 6: Vision-Based Fatigue Crack Detection using Video Feature Tracking

This chapter is modified based on the following journal publication:

Kong, X. and Li, J., (2018). Vision-based fatigue crack detection of steel structures using video feature tracking. *Computer-aided Civil and Infrastructure Engineering*, 33, (9). 783-799.

6.1 Overview

In this chapter a novel computer vision-based approach for fatigue crack detection is proposed through a video stream. This method tracks the surface motion of a crack-prone area, and detects fatigue cracks by identifying discontinuities induced by the opening and closing of fatigue cracks under repetitive loads recorded in a video stream. Compared with methods based on edge detection in static images, our proposed method does not rely on edge features of cracks, leading to more robust detection results even when the crack is surrounded by crack-like edges, covered by dust, rust, and corrosion, or visually invisible to human eyes under crack closure. Compared with DIC technologies, our proposed approach is more flexible for field implementation since it does not require expensive equipment, special light sources, or surface treatment. Furthermore, this method enables accurate quantification of the crack opening with submillimeter accuracy. Such information would be used for fatigue damage assessment and long-term fatigue life prediction. Finally, the proposed approach can also be applied to identify the discontinuities in other engineering applications such as detecting localized slippage or loosening of structural components.

The rest of this chapter is organized as follows. Section 6.2 begins with a brief overview of the proposed approach, followed by the technical backgrounds of feature point detection and feature point tracking, and introduces the proposed crack detection algorithm. Section 6.3 validates the proposed approach in two different experimental setups for in-plane and out-of-plane fatigue cracks, respectively. Conclusions are made in Section 6.4.

6.2 Methodology

Figure 50 provides an overview of the proposed approach. First, a short-period video stream is taken for a structural component with existing fatigue cracks under repetitive loading. A region of interest (ROI) is selected in the video stream, in which feature points are detected for each frame t of the video stream. The next step is to track the movement $\delta^i(t)$ of each feature point i throughout the video stream. A feature point matching technology is applied in this step to eliminate outliers. Once the movements of all feature points are obtained, crack detection is achieved by evaluating the movement pattern of each feature point against its adjacent feature points within a localized circular region (LCR). If all feature points share a similar movement pattern, the movement of the LCR is considered as rigid-body motion. If differential movement patterns are found, the feature point at the center of the LCR is highlighted since a crack may exist in the LCR to cause such a phenomenon. Finally, by moving the LCR across each feature point and repeating the above procedure, all LCRs with differential movement patterns are highlighted by their center feature points. The collection of these highlighted feature points indicate the location of the cracks and their associated movements tracked through the video stream can be used to quantify crack dimensions.

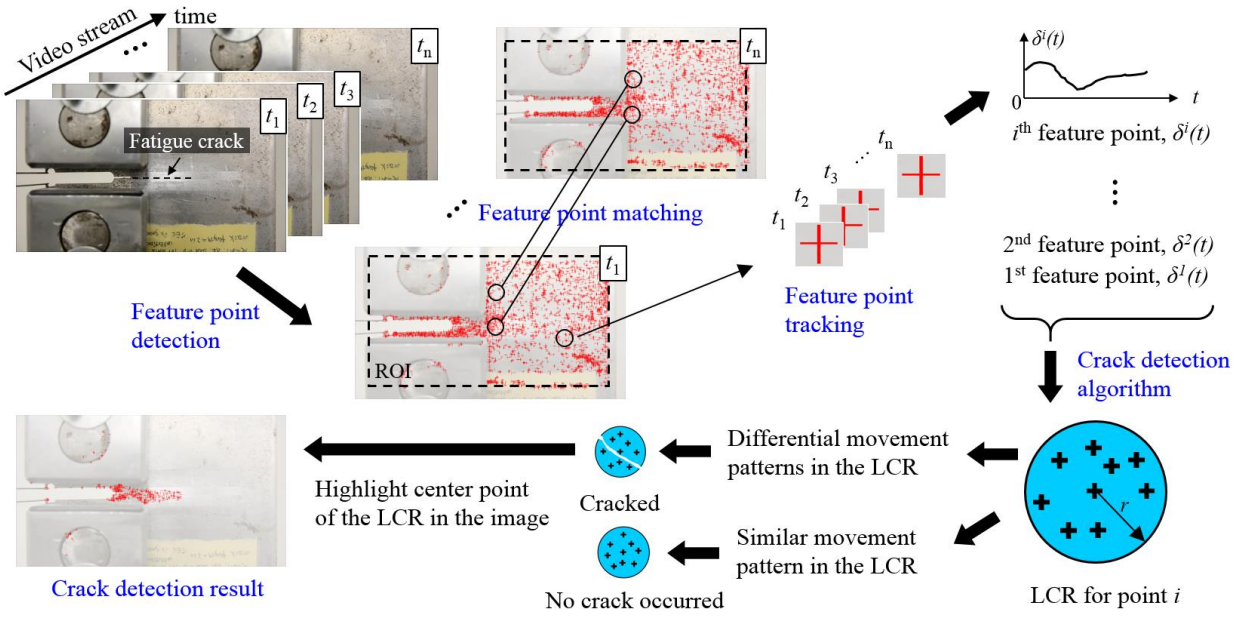

Figure 50. Overview of the proposed approach: t_1, t_2, t_3 … t_n are different frames in a video stream; ROI is the region of interest; $\delta(t)$ is the movement of a feature point; LCR is the localized circular region; and r is the radius of the LCR in terms of pixels.

6.2.1 Feature tracking

In the context of this study, feature tracking is a two-step process: 1) automatically detecting feature points from the monitored structure without using physical target or surface treatment; and 2) robustly tracking movements of these feature points throughout the video stream. Feature tracking has been widely applied for solving many engineering problems including vehicle tracking (Coifman et al., 1998), image mosaicing (Zoghlami et al., 1997), 3D reconstruction (El-Hakim et al., 2004), object recognition (Ta et al., 2009), and so forth. Despite of the great potential of feature tracking techniques, it has not attracted enough attention in the field of civil infrastructural health monitoring. Only a limited number of applications (Khuc and Catbas, 2017; Yoon et al., 2016) have been reported in the literature for tracking global displacement measurement of structures.

6.2.1.1 Feature point detection

Numerous algorithms of feature point detection have been proposed by researchers in computer vision. Several well-known algorithms include: Harris-Stephens (Harris and Stephens, 1998), Shi-Tomasi (Shi, 1994), speeded up robust features (SURF) (Bay et al., 2006), features from accelerated segment test (FAST) (Rosten and Drummond, 2005], scale invariant feature transform (SIFT) (Lowe, 2004), and so forth. We adopted the Shi-Tomasi algorithm in this study. To start the process, an ROI is first selected in the video stream to focus on a specific region for feature point detection. The ROI can be the entire scene or a reduced-size region, depending on the availability of prior knowledge about the approximate location of fatigue cracks. Once the ROI is selected, Shi-Tomasi (Shi, 1994) feature point detector is applied to automatically detect all the feature points within the ROI. To explain this procedure, suppose $I(x, y)$ is an intensity 2D image; I_x and I_y are image intensity derivatives in horizontal and vertical directions respectively; λ_1 and λ_2 are eigenvalues of matrix M within a window function $w(x, y)$:

$$M = \sum_{x,y} w(x,y) \begin{bmatrix} I_x I_x & I_x I_y \\ I_x I_y & I_y I_y \end{bmatrix} \tag{1}$$

Feature points can be determined if λ_1 and λ_2 satisfy the following criteria:

$$R = \min\{\lambda_1, \lambda_2\} > \text{a predefined threshold} \tag{2}$$

To demonstrate how Shi-Tomasi algorithm works, two examples are presented using images of a highway bridge in the field (Figure 51a) and a steel component (Figure 51e) inside a laboratory. Two images were taken by a camera of a smartphone (4th generation Moto G Play) with a resolution of 3264 pixels × 2448 pixels. For illustration purpose, the ROI is selected as a small region of 50 pixels × 100 pixels (Figure 51b and 2f). Then, the Shi-Tomasi algorithm is applied for automatically searching all the possible points that satisfy Equation 2. All detected

points are shown as crosses in Figure 51c and 2g. Typical feature points along with their adjacent areas are visualized in Figure 51d and 2h using patches with 11 pixels × 11 pixels.

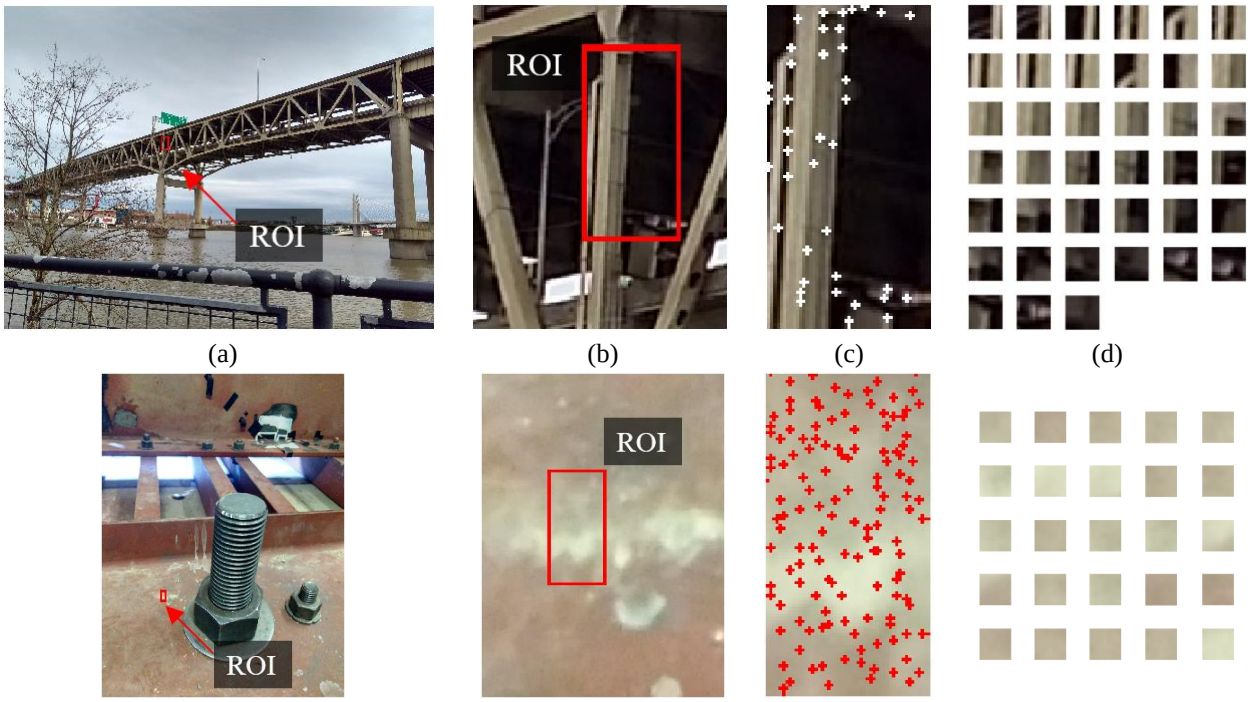

Figure 51. Two examples for demonstrating feature point detection: (a) An image of a highway bridge taken by a smartphone with a resolution of 3264 pixels x 2448 pixels; (e) A image of a steel girder taken by the same smartphone; (b and f) ROIs with a size of 50 pixels × 100 pixels are selected; (c and g) feature points detected by the Shi-Tomasi algorithm within the ROIs; (d) all 39 detected feature points in (c) are visualized using 11 pixels × 11 pixels patches; and (h) the strongest 25 out of the 134 detected feature points in (g) are visualized using 11 pixels × 11 pixels patches.

Several unique aspects of feature point detection can be observed from the examples: 1) feature points are detected based on the change of intensity gradient in the image, which is an inherent nature exists in most images. In this regard, special templates or physical targets commonly required in traditional motion tracking (Feng et al., 2015; Park et al, 2010) are not needed; 2) detecting feature points does not require special lighting conditions or high-end cameras, making it more flexible for engineering applications; and 3) in total 39 and 134 feature points were detected in very small ROIs of the bridge and girder images, respectively, indicating the efficiency of the detecting algorithm.

6.2.1.2 Feature point tracking

Once feature points are detected using the Shi-Tomasi algorithm, the next step is to robustly track the movement of each feature point throughout the video stream. The Kanade-Lucas-Tomasi (KLT) tracker (Tomasi and Takeo, 1991; Lucas and Takeo, 1981) is proposed for tracking feature points in this study. To be able to track feature point *i* throughout the video stream, the KLT tracker would estimate the movement of point *i* between two adjacent frames within the window function $w(x, y)$, so that the Sum of Squared Differences (SSD) of an intensity image $I(x, y)$ is minimized (Sinha et al., 2006). In addition, the Forward-Backward error (Kalal et al., 2010) is adopted for estimating the discrepancies between forward and backward trajectories measured in two adjacent frames. Such an error measurement can reliably detect potential tracking failures (i.e. outliers) and select reliable trajectories in the video stream.

6.2.2 Crack detection algorithm

The principle of the crack detection algorithm is to efficiently and robustly identify discontinuities in the surface motion of the structural component from a video stream. Identifying such discontinuities from the feature point movements could be challenging since the movement of the crack opening and closing is usually very small, hence can be submerged in the larger global rigid-body movement of the monitored structure. To tackle this problem, first denote *x* and *y* as horizontal and vertical coordinates of a 2D image. $x^i(t)$ and $y^i(t)$ are two vectors containing the coordinates of feature point *i* at frame *t*. *M* is the total number of feature points in the ROI. The relative movements of feature point *i* between the t^{th} frame and the initial frame can be expressed as:

$$x_r^i(t) = x^i(t) - x^i(1), \text{ and } y_r^i(t) = y^i(t) - y^i(1) \quad (5)$$

where superscript r represents relative movement, $x^i(1)$ and $y^i(1)$ are the coordinates of feature point i at the initial frame of the video stream. Subsequently, the total movement of feature point i combining both $x^i(t)$ and $y^i(t)$ components is:

$$\delta^i(t) = \sqrt{x_r^i(t)^2 + y_r^i(t)^2} \tag{6}$$

To efficiently identify the movement pattern of the structural surface, the standard deviation S^i of $\delta^i(t)$ is adopted since it provides a robust indication of the magnitude of movement under repetitive loads. In a similar manner, standard deviations of all feature points within the ROI can be computed as S^1, S^2, …, S^i, …, S^M. Then, for each feature points i, a localized circular region (LCR) is defined using point i as the center point and r as the radius. The movement pattern of all feature points within the LCR is evaluated by computing the coefficient of variation CV^i of the standard deviations (S^1, S^2… S^i… S^M) of these feature points located in the LCR. If CV^i is smaller than a predefined threshold Γ, all the feature points in the LCR are considered having the same movement pattern, i.e. rigid-body movement. On the other hand, if CV^i exceeds the threshold Γ, differential movement patterns have occurred in the LCR, indicating the existence of a crack within the LCR.

The above algorithm is illustrated in Figure 52 using a steel plate with an existing fatigue crack as an example. Suppose a repetitive fatigue load F is applied at the top of the plate while the bottom of the plate is fixed. All feature points have been detected in the ROI using Shi-Tomasi algorithm and two typical LCRs are selected for evaluation. LCR 1 contains 7 feature points labeled with point 1 to 7 for demonstration purpose (in practice, feature point labels may not be continuous). Because LCR 1 is away from the crack, it is subjected to a rigid-body movement under F. The movements of all 7 feature points $\delta^1(t)$ to $\delta^7(t)$ would follow a similar pattern under the applied fatigue load F. The standard deviations S^1 to S^7 feature point

movements $\delta^1(t)$ to $\delta^7(t)$ in LCR 1 should have a similar magnitude, leading to a small coefficient of variation CV^1 which is close to zero. In contrast, LCR 2 has 6 feature points (point 21 to 26) with two distinct movement patterns: 4 points above the crack exhibit a similar movement pattern, while point 25 and 26 at the bottom have a much smaller response because of the fixed boundary condition. Such distinct movement patterns in LCR 2 lead to a higher coefficient of variation CV^{21}, indicating the discontinuity and hence a crack occurred in LCR 2.

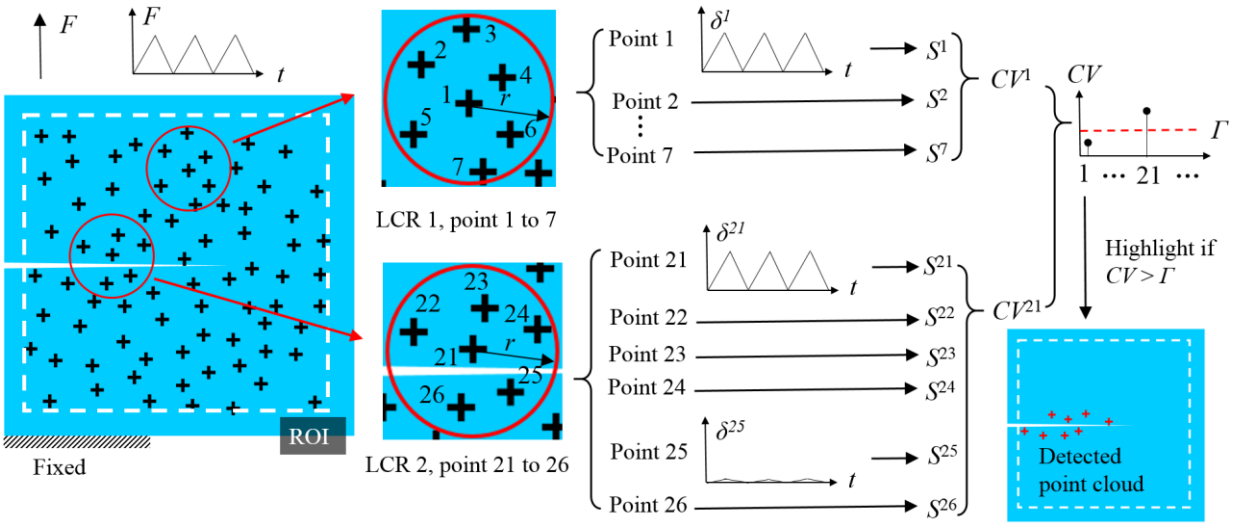

Figure 52. An example for demonstrating the crack detection algorithm using a cracked steel plate, where F is the applied fatigue load, ROI is the region of interest, LCR is the localized circular region, r is the radius of the LCR, $\delta(t)$ is the movement of feature point, S is the standard deviation of $\delta(t)$, CV^1 is the coefficient of variation of S^1 to S^7, CV^{21} is the coefficient of variation of S^{21} to S^{26}, and Γ is the predefined threshold.

Finally, after evaluating each LCR using the above procedure, a vector of coefficient of variation CV is obtained. Feature points at centers of LCRs with CVs larger than the threshold Γ are highlighted. These highlighted feature points are termed as detected point cloud, which is the indicator of the crack path.

6.3 Experimental validation

6.3.1 Validation for in-plane fatigue crack

An experimental test was performed for validating the proposed algorithm using a small-scale compact, C(T), specimen with an in-plane fatigue crack. The test setup and the observed fatigue crack characteristics are presented first. Then, the crack detection result using the proposed approach is illustrated. Finally, a cost-effective approach is introduced for quantifying the crack opening based on feature tracking.

6.3.1.1 Test configuration

The proposed approach was validated through a cracked C(T) specimen under fatigue loading. Figure 53 shows the test setup. Briefly, a closed-loop servo-hydraulic uniaxial load frame served as the fatigue loading system. Normal lighting condition was applied for this test using two ceiling lamps in the laboratory (Figure 53a). A commercial-grade digital camera (Nikon D7100 with Sigma 17-50 mm lens) was deployed on a tripod in front of the C(T) specimen (Figure 53b). The distance between the camera and the C(T) specimen was about 25 cm and the lens was parallel to the surface of the specimen. The C(T) specimen was made of a A36 steel plate with a thickness of 6.35 mm, while other dimensions are shown in Figure 53e. To visually observe the fatigue crack, the specimen had been polished by sandpapers (Figure 53c). The C(T) specimen was installed in the loading frame through two clevises and rods. At the front face (denoted in Figure 53e) of the C(T) specimen, a clip-on displacement gauge (epsilon 3541-0030-150T-ST) was mounted for accurately measuring the opening of the crack (Figure 53c). During the test, a periodic fatigue load was applied by the actuator through the bottom clevis while the top clevis was fixed (Figure 53d). At the time of this test, a fatigue crack had been generated in the

specimen. Using an adhesive measuring tape, the length of the crack measured from the notch of the specimen (Figure 53c) was found to be 53.3 mm as shown in Figure 53f.

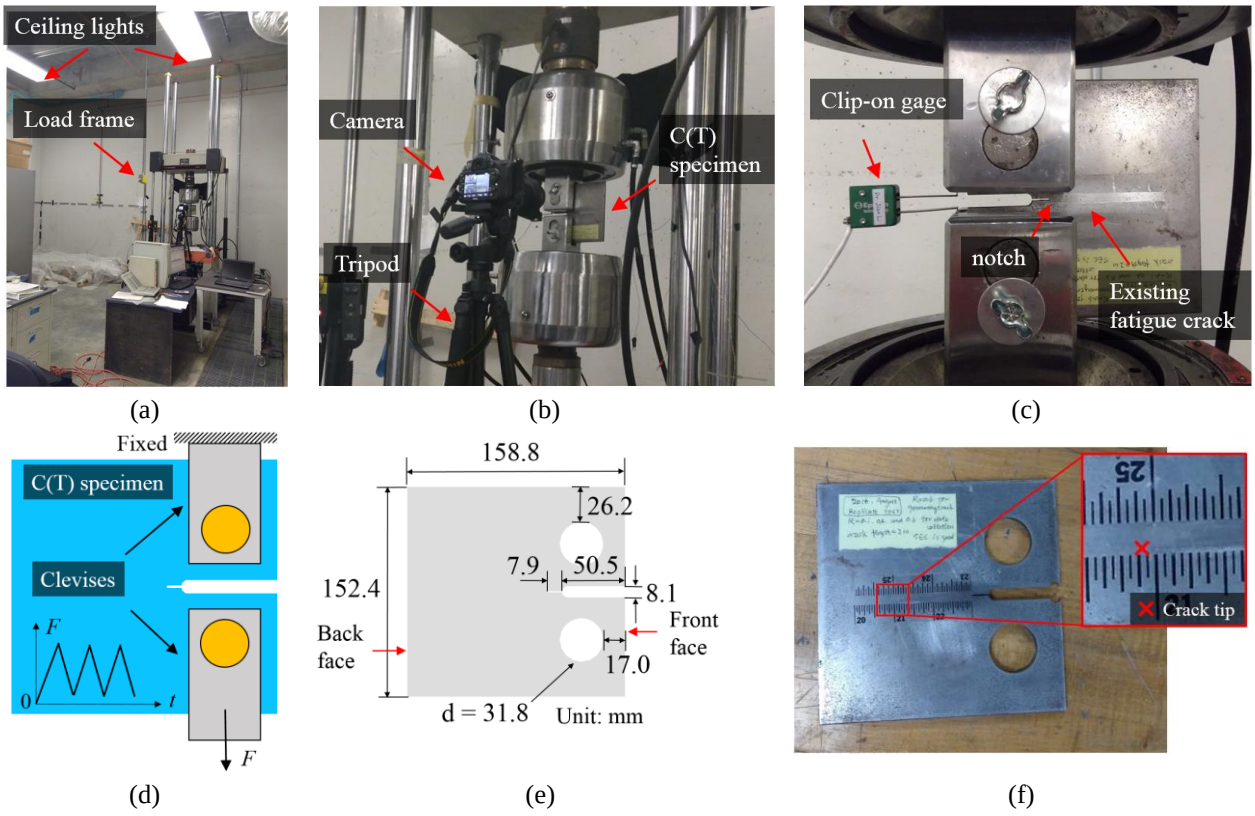

Figure 53. Test setup: (a) load frame and lighting conditions; (b) camera setup; (c) clip-on gauge installation; (d) boundary condition of the specimen; (e) dimensions of the specimen; and (f) identification of the crack length using adhesive measuring tape (US unit).

Because the crack opening on the C(T) specimen is proportional to the applied load, designing a realistic loading protocol is critical for validating the proposed crack detection approach. Here we adopted ASTM E1820-15 (ASTM, 2015) as the design guide. The range of stress intensity factor ΔK was determined as 19.8 MPa$\sqrt{m}$ and the stress intensity ratio R was assigned as 0.47. Utilizing these design parameters, F_{max} and F_{min} of the load cycles were computed as 3.0 kN and 6.5 kN, respectively. A detailed calculation procedure of F_{max} and F_{min} based on ΔK and R can be founded in Kong et al. (2017a). Figure 54e shows the design result, in which 10 load cycles were applied on the specimen. The fatigue loading rate was 0.5 Hz. Under

such a loading protocol, the peak-to-peak amplitude of the crack opening was found to be around 0.2 mm measured by the clip-on gauge at the front face of the C(T) specimen (Figure 54d).

Figure 54a is an image taken from the recorded video stream when the applied load was 0 kN. The detailed view of the fatigue crack is shown in Figure 54b, where the crack is difficult to be visually identified. When F increased to F_{mean} = (F_{max} + F_{min}) / 2 = 4.75 kN (Figure 54c), it provoked an opening of the crack, making it visually observable (Figure 54c). When F reached its maximum of 6.5 kN, a slightly larger crack opening can be found in Figure 54d.

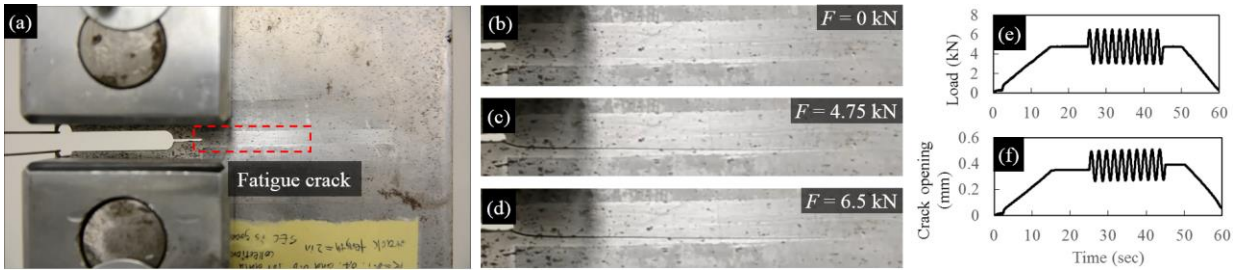

Figure 54. Characteristics of the crack under fatigue loading: (a) a frame taken from the video stream when the applied load F is 0 kN; (b) close-up view of the fatigue crack in Figure 54a; (c) close-up view of the fatigue crack when F is 4.75 kN; (d) close-up view of the fatigue crack when F is 6.5 kN; (e) loading protocol adopted in this test; and (f) the crack opening measured by the clip-on gauge at the front face of the specimen.

6.3.1.2 Crack detection

During the fatigue test, a video was taken for the entire loading event presented in Figure 54e. A 6-sec video stream was cut off from the original video which includes the C(T) specimen under the repetitive load. The resolution of the video is 1920 pixels × 1080 pixels and the frame rate is 29.97 fps. Then, the video stream was processed by the proposed crack detection algorithm described in section 6.2 using the Matlab Computer Vision Toolbox (MathWorks, 2016). Figure 55a shows the initial frame and the selected ROI of the 6-sec video stream. In the ROI, a total of 4043 feature points were detected by the Shi-Tomasi feature point detection algorithm (Figure 55b). Generally, feature points were evenly distributed over the ROI except regions of the two clevises where less feature points were extracted. This is due to the fact that the camera did not

focus on the clevises. However, a few feature points were still recognized at the tiny gaps between the clevises and rods due to higher gradient change at these localized regions.

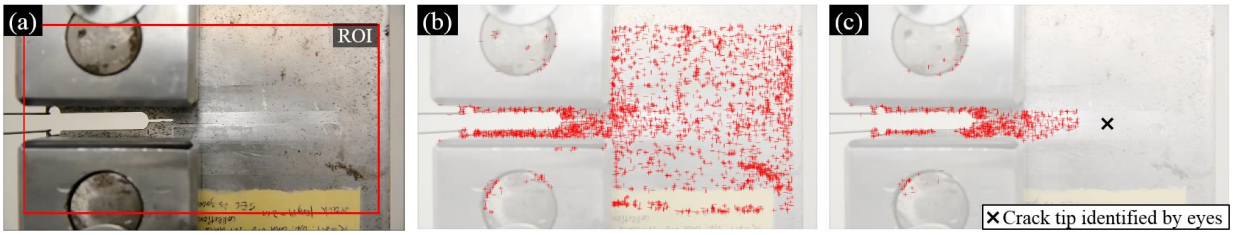

Figure 55. (a) The initial frame of the video stream where the ROI is shown in the red box; (b) all feature points are detected by the Shi-Tomasi algorithm; and (c) crack detection result. Brightness of images in (b) and (c) are enhanced to highlight the feature points.

Figure 55c shows the crack detection result when r = 120 pixels, Γ = 0.20, in which r is the radius of the LCR and Γ is the threshold coefficient of variation described in section 6.2.2. In Figure 6c, a feature point is highlighted if differential movement patterns were found in its associated LCR. In other words, all highlighted feature points in Figure 55c had discontinuity occurred in their surrounding areas (i.e. LCR with a radius of r). The actual fatigue crack should pass through the detected point cloud. An interesting phenomenon from the result is that a few feature points appear at the gaps between the clevises and rods, which might be due to the discontinuities caused by the relative rotation between the clevises and rods during the test.

6.3.1.3 Quantifications of crack opening

Crack opening is an important characteristic for evaluating fatigue crack since it directly relates to the stiffness reduction of the crack-prone region. Quantifying crack opening is critical for compliance calculation and fatigue life prediction (Newman, 1984; Saxena and Hudak, 1978). Traditional crack opening measurement methods (Marsh et al., 1991) (ex. clip-on gauge, back face strain gauge, push rod gauge, potential drop, and ultrasonic method) require significant amount of work for instrumentation. Here we proposed a cost-effective approach for quantifying the crack opening using computer vision-based feature tracking.

Figure 56a illustrates the methodology for quantifying crack opening. A similar strategy was also proposed by Sutton et al. (1999) using a far-field microscope. Briefly, the fatigue crack is first localized by the proposed crack detection algorithm as shown in Figure 56a. Based on the location of the fatigue crack, a pair of windows with size of 60 pixels × 60 pixels is deployed at location *a* along both sides of the crack path. Then, using the existing tracking results of all feature points in Figure 55b, each window's movement can be estimated as the average movement of all feature points within the window. Next, by subtracting the movement of the top windows from that of the bottom window, the relative movement between the window pair (i.e. crack opening) can be obtained. Using the same process, another crack opening measurement can be taken by moving the pair of windows to location *b*. Table 5 lists the global coordinates of each window pair.

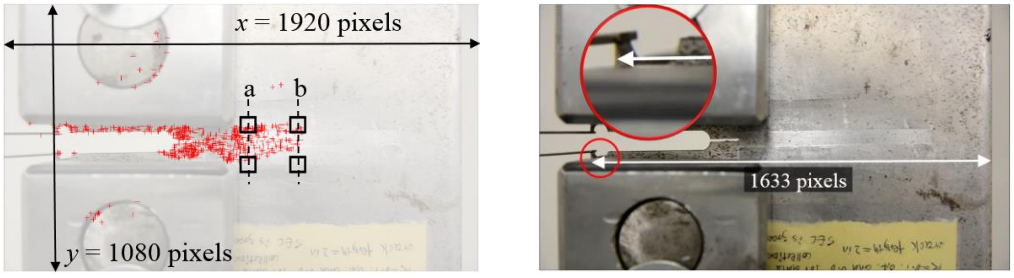

(a) (b)

Figure 56. (a) The methodology for crack opening measurement; and (b) the distance between the front face and back face of the C(T) specimen in terms of pixels

Table 5. Description of the windows in Figure 56a

Window locations		**Coordinates (unit: pixels)**	
		Window's top-left corner	**Window's bottom-right corner**
Location *a*	Top	$x = 960, y = 460$	$x = 1120, y = 520$
	Bottom	$x = 960, y = 620$	$x = 1120, y = 680$
Location *b*	Top	$x = 1160, y = 460$	$x = 1220, y = 520$
	Bottom	$x = 1160, y = 620$	$x = 1220, y = 680$

Figure 57 shows the raw measurements of crack openings at location *a* and *b* during the entire loading event. Both measurements show similar responses under the applied load but the peak-to-peak amplitudes are decreased at the location closer to the crack tip. Notice that the crack opening measurements are shown in pixels. To convert measurements from pixels to length unit (e.g. mm), one approach is using the knowledge about the real world dimensions of the monitored scene. Similar approaches have been adopted by many vision-based motion monitoring approaches (Park et al., 2010; Wahbeh et al., 2003). For this particular test, a scaling factor is computed based on the distance between front face and back face (both denoted in Figure 53b) of the C(T) specimen, which is measured as 158.8 mm (Figure 53e) and 1633 pixels in the video (Figure 56b), leading to a scaling factor of 0.0972 mm/pixel. Using this scaling factor, crack opening measurements can be easily converted to mm, as shown in the vertical axes on the right-hand-side in Figure 57.

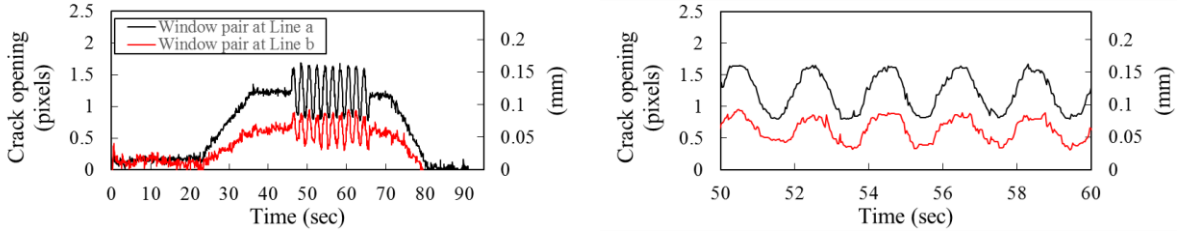

Figure 57. (a) Vision-based crack opening measurements at location a and location b on the specimen; and (b) the detailed measurements between 50 to 60 sec.

Lastly, Figure 58 shows a comparison between crack opening measurements at the front face of the specimen based on the proposed vision-based approach and the ground truth. The vision-based measurement is taken from the relative movement between a pair of windows at the front face (Figure 58a); while the ground truth is obtained by the clip-on gauge mounted at the same location. Excellent agreement can be found in Figure 58b and c, indicating the accuracy of the proposed method for quantifying crack opening in sub-millimeter level.

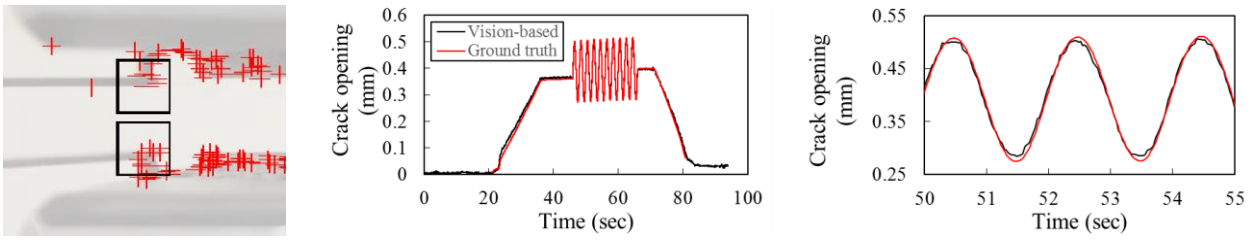

(a) (b) (c)

Figure 58. (a) A pair of windows with size of 60 pixels × 60 pixels is deployed at the front face of the specimen; (b) A comparison of crack openings at the front face of the specimen: vision-based approach vs. ground truth measured by the clip-on gauge; and (b) a detailed view of the measurements between 50 to 55 sec.

6.3.2 Validation for out-of-plane fatigue crack

This section further investigates the proposed crack detection approach on out-of-plane fatigue cracks based on a skewed girder-to-cross-frame connection. The purpose of this test is to examine the robustness of the proposed approach in a more realistic structural configuration. The test model and test setup are first introduced, followed by crack detection results and discussions.

6.3.2.1 Test configuration

A skewed bridge girder to cross frame connection was adopted for this test, which was a typical structural connection in many steel highway bridges in the United States (Hartman et al., 2010; Hassel et al., 2016). As shown in Figure 59a, the bottom flange of the steel girder was mounted on the floor, simulating the constraint from the bridge deck. At the mid-span of the girder, a cross frame was connected to the girder web via a stiffener plate. Fillet welds were applied along both sides of the stiffener (Figure 59b). Due to the lack of consideration of fatigue resistance, a common issue for such type of bridges designed before 1985 in the United States, the stiffener was only welded to the girder web while the top and bottom of the stiffener were free to move (i.e. a gap existed between the stiffener and the bottom flange as shown in Figure 59c). At the far end of the cross frame, a closed-loop servo-hydraulic uniaxial actuator applied fatigue loads in

the vertical direction (Figure 59a). Geometric dimensions and discussion on the fatigue mechanism of this test model can be found in Yu et al. (2017).

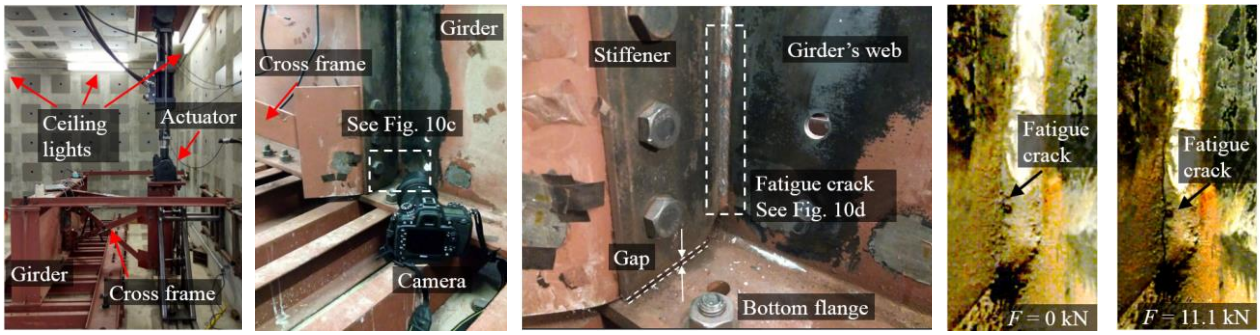

(a) (b) (c) (d) (e)

Figure 59. (a) Test model setup; (b) the girder to cross frame connection and camera setup; (c) detailed look of the crack prone region; (d) blow-up detail of fatigue crack when the applied load *F* is 0 kN; and (e) blow-up detail of fatigue crack when the applied load *F* is 11.1 kN. (The image brightness in Figure 59d and e is enhanced 100% for demonstration purpose)

Prior to the test in this study, the connection model had been applied with 2.7 million load cycles with the load range 0 kN to 11.1 kN, causing an out-of-plane fatigue crack along the vertical weld toe between the stiffener and the web (Figure 59c). The fatigue crack was about 70 mm in length along only one side of the stiffener (i.e. does not penetrate the thickness of the stiffener). Figure 59d and 10e demonstrates the detail of fatigue crack when the applied load was 0 kN and 11.1 kN, respectively.

No special light sources were adopted in this test. As shown in Figure 59a, regular ceiling lights were used when the video clip was taken. The same camera in section 6.3.1 was used and the setup is shown in Figure 59b. The distance between the lens and the fatigue crack is about 15 cm. The video was taken while repetitive fatigue load cycles (0 kN to 11.1 kN) were applied to the test model at a loading rate of 0.5 Hz.

6.3.2.2 Crack detection

During the fatigue load cycles, a 6-sec video stream was taken. The resolution of the video stream was 1920 pixels × 1080 pixels and the frame rate was 29.97 fps. Then, the video stream

was processed under the proposed crack detection algorithm described in section 6.2. Figure 60a shows the initial frame and the selected ROI of the video stream. Compared with the C(T) test, the lighting was weaker in this test, leading to a darker scene in the video stream. Nevertheless, a total of 3736 feature points were detected by the Shi-Tomasi feature point detection algorithm (Figure 60b).

Figure 60c shows crack identification results using r = 60 pixels, Γ = 0.35, where r is the radius of the LCR and Γ is the cut-off coefficient of variation (see section 6.2.2). As shown in the figure, the out-of-plane fatigue crack has been successfully detected as a point cloud of highlighted feature points between the stiffener and the web, which is consistent with the location of the fatigue crack shown in Figure 59d.

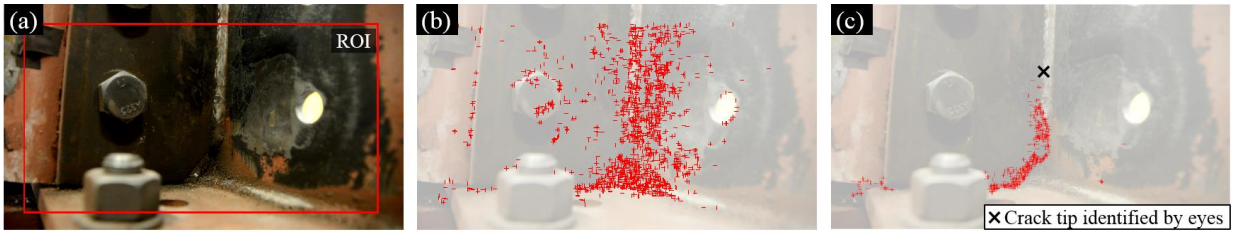

Figure 60. (a) The ROI is shown as red box in the initial frame of the video stream; (b) all feature points are detected by Shi-Tomasi algorithm; and (c) crack detection result. Brightness of images in (b) and (c) are enhanced for demonstration purpose.

In addition to the correct detection of fatigue crack, some false positive detection results are also found. As shown in Figure 61, the majority of false positive detection results occur along the bottom edge of the stiffener. This is because the bottom of the stiffener rotates during the test, creating discontinuities in the motion of the scene within its adjacent areas.

(a) (b)

Figure 61. (a) Truth crack detection vs. false positive detection; and (b) the detail of Figure 61a.

6.3.3 Discussion on testing results

This section discusses two important parameters r and Γ in the proposed method and how these thresholds affect the crack detection results. Then it is followed by a comparative study between the proposed approach and edge detection-based methods. Finally, the computational cost and limitations of the proposed approach are discussed.

6.3.3.1 Parametric study for r and Γ

As described in section 6.2.2, cut-off threshold of the coefficient of variation Γ and radius of the LCR r are two important parameters of the proposed approach. A parametric study is presented here to illustrate how these two parameters affect crack detection results.

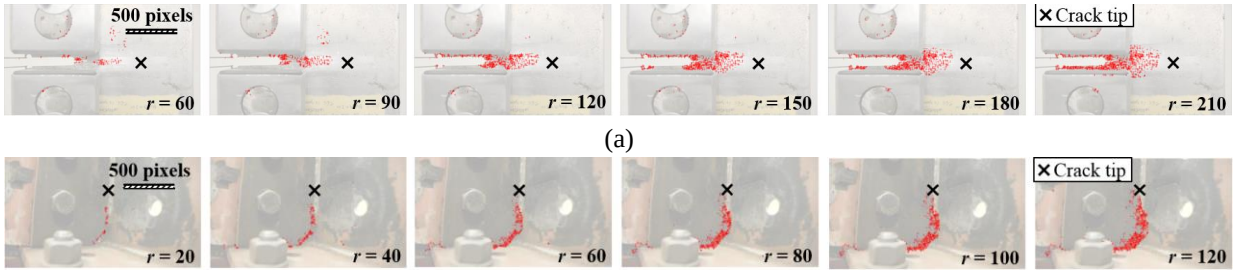

Figure 62. Comparison of crack detection results under different r: (a) in-plane fatigue crack detection with Γ = 0.20 and r = 60, 90, 120, 150, 180, 210 pixels; and (b) out-of-plane fatigue crack detection with Γ = 0.35 and r = 20, 40, 60, 80, 100, 120 pixels.

Figure 62 shows the crack detection results under different r values for the two experimental tests, in which Γ is fixed at 0.20 for the in-plane fatigue test and 0.35 for the out-of-

plane fatigue test. As shown in the figure, increasing the radius r of the LCR leads to more robust crack detection results since more feature points are contained in each LCR. However, the accurate location of the fatigue crack may be difficult to be localized since the highlighted feature points occupy a wider area around to the crack path. On the other hand, a smaller r yields more accurate crack detection result since it can narrow down the location of the fatigue crack by showing less highlighted feature points; however, the detection result may become less robust due to insufficient feature points detected.

Figure 63 illustrates crack detection results under different Γ values for the two experimental tests, in which r is fixed at 120 pixels for the in-plane fatigue test and 60 pixels for the out-of-plane fatigue test. As shown in the figure, increasing Γ leads to a more stringent detection criterion as only LCRs with significant differential movement pattern can be detected as crack path, while small discontinuities may be neglected. As a result, less highlighted feature points were obtained and the detected point cloud became shorter (see the first column of Figure 63). On the other hand, a lower Γ leads to longer detected length of the point cloud. However, if Γ is too small, the tradeoff is false positive results may appear or the accuracy of crack path may decrease since more LCRs can satisfy the less stringent criterion (see the last column of Figure 63);

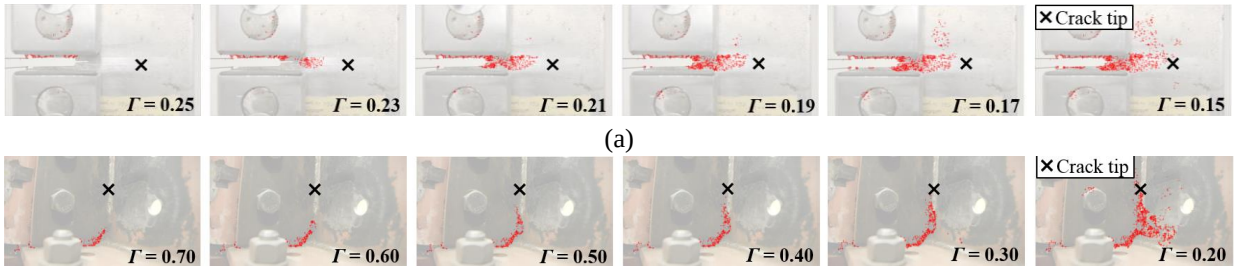

Figure 63. Comparison of crack detection results under different Γ: (a) in-plane fatigue crack detection with r = 120 pixels and Γ = 0.25, 0.23, 0.21, 0.19, 0.17, and 0.15; and (b) out-of-plane fatigue crack detection with r = 60 pixels and Γ = 0.70, 0.60, 0.50, 0.40, 0.30, and 0.20.

In summary, both r and Γ affect the performance of the proposed crack detection method by changing the shape features (i.e. length and width) of the detected point cloud. Tuning these two parameter would be necessary to achieve optimal crack detection. The above results also demonstrate the difficulty of accurately identifying the crack tip. This is because the crack opening around the crack tip is extremely small, leading to a small discontinuity in the surface motion. Detecting such a small discontinuity is beyond the capacity of the proposed approach which is based on a consumer-grade digital camera. As shown in the last column of Figure 63, the detected point cloud can cover the crack tip if a very low cut-off threshold Γ is applied, but false positive detection results may appear in non-cracked regions as well. This is because both the detected non-cracked region (false positive results) and the crack tip have similar level of differential movements identified by the proposed crack detection algorithm. Lastly, it should be noted that the optimal ranges of r and Γ vary with different applications. Examples of factors include the distance between the lens and the monitored surface, the magnitude of movement of the monitored structure, and the magnitude of the crack opening (i.e. the stiffness of the crack-prone region).

6.3.3.2 Comparative study

Figure 64 and Figure 65 compare the proposed approach against some edge detection methods for crack detection. Here Sobel (Sobel and Feldman, 1968) and Canny (Canny, 1986) edge detectors are selected for their well-known performances in edge detection. Unlike the proposed method which is based on video streams, edge detection methods are based on static images. Two static images were taken from recorded videos of in-plane and out-of-plane tests, where the specimens were under the maximum applied load in order to generate the maximum crack opening.

For the in-plane fatigue test, Sobel (Figure 64b) and Canny (Figure 64c) edge detectors can capture the fatigue crack. However, the truth fatigue crack is also surrounded by many crack-like edges including the boundary of clevises and the sticky note, as well as other texture on the surface. Isolation of the true crack would require further processing. In the out-of-plane fatigue test, even though both edge detectors demonstrate their ability to identify edge features from the images (Figure 65b and 16c), none of them represents the truth fatigue crack as the crack feature is hidden within the complex textures.

On the other hand, the proposed approach is based on tracking the dynamic motion of the specimen surface in a video stream, leading to more robust detection results (Figure 64d and Figure 65d), even though the detected surface is covered by other crack-like edges, contaminated by complex textures, or under insufficient light environment.

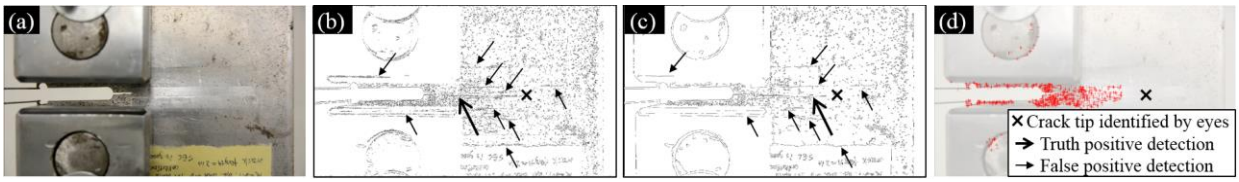

Figure 64. Comparison of the proposed approach with two edge detectors for in-plane fatigue crack detection: (a) input image; (b) Sobel edge detector; (c) Canny edge detector; and (d) the proposed approach

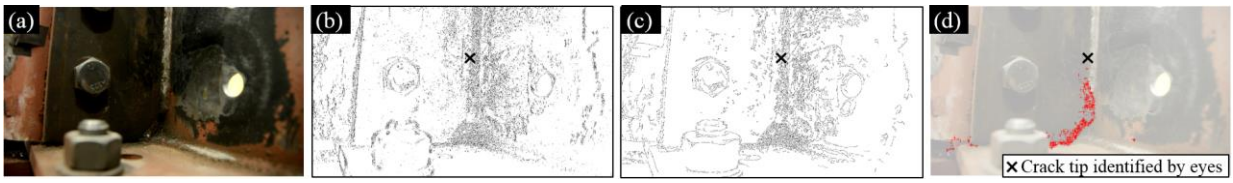

Figure 65. Comparison of proposed approach with two edge detectors for out-of-plane fatigue crack detection: (a) input image; (b) Sobel edge detector; (c) Canny edge detector; and (d) the proposed approach

6.3.3.3 Computational cost

The proposed approach demonstrates its high efficiency in terms of computational cost. For the 6-sec video stream under 1920 pixels × 1080 pixels resolution adopted in both experimental tests, the processing time is about 1 min on a desktop computer (16 GB RAM, 3.1GHz CPU). Such a

performance show great potential for implementing this approach for near-real-time fatigue crack monitoring.

6.3.3.4 Limitations

The main limitation of our approach is that the camera needs to be stabilized during the video acquisition, a common requirement existing in many video-based motion tracking approaches (Yoon et al., 2016). The performance of the feature tracking can be affected if the video stream is taken by a non-stabilized camera (e.g. hand-hold mode). Additional compensation strategies are needed if the proposed approach is to be implemented based on Unmanned Aerial Vehicles (UAVs) for automated bridge inspection in the future. In addition, to obtain the accurate crack opening in a real world length unit, the camera lens needs to be parallel to the monitored surface and at least one physical dimension of an object from the monitored structure needs to be known as a priori for computing the scaling factor. Lastly, accurately identifying the crack tip remains a challenge due to the small movement of crack opening around the crack tip. One alternative solution is to estimate the crack tip using the crack opening measurement and the applied load, which has been widely adopted in fatigue tests of standard specimens (ASTM, 2015).

6.4 Conclusions

This chapter presents a vision-based approach for automated fatigue crack detection and quantification from a video stream. The proposed approach is based on tracking the surface motion of the cracked specimen under repetitive fatigue load and localizing the crack by identifying differential movement patterns on the surface in the video stream. The effectiveness of the proposed approach has been successfully validated through two experimental tests: 1) a C(T) specimen with an in-plane fatigue crack; and 2) a skewed girder to cross frame connection with a distortion-induced out-of-plane fatigue crack. Both test results indicate that the proposed

approach can robustly identify the fatigue crack, despite the insufficient light condition and complex textures of the monitored surface. Furthermore, a cost-effective approach has been established to accurately quantify the crack opening using the feature tracking technology. Such a measurement is a critical element for fatigue crack evaluation. Future study will focus on implementing the proposed algorithm on autonomous platforms such as UAVs for the automated structural inspection.

Chapter 7: Vision-Based Fatigue Crack Detection using Image Overlapping

This chapter is modified based on the following journal manuscript:

Kong, X. and Li, J., (2018). Non-contact fatigue crack detection in civil infrastructure through image overlapping and crack breathing sensing. In preparation.

7.1 Overview

In this chapter, we propose an image overlapping approach to detect fatigue cracks in metallic structures. Compared with edge detection-based crack detection methods, the proposed approach yields more robust detection results even the true fatigue crack is surrounded by other non-crack edges. Compared with machine learning-based crack detection methods, our approach does not require prior knowledge about the damage status of the monitored structure for training the classifier. Compared with DIC-based crack detection technologies, this approach demonstrates significant flexibilities and potential for field applications, as it is solely based on a consumer-grade digital camera and does not require special lighting or surface treatment. Compared with our previous crack detection method through video feature tracking (Kong et al., 2018b; 2018c), the image overlapping-based approach shows higher precision for crack localization. More importantly, instead of relying on a fixed camera, image collection in this study can be performed through a hand-held camera under different camera poses. The unfixed camera feature in the proposed approach shows great potential to be integrated with the unmanned aerial vehicles (UAVs) for achieving autonomous fatigue crack inspection of civil infrastructure.

The rest of this chapter is structured as follows: Section 7.2 reviews related work in the literature and highlights our contributions; Section 7.3 demonstrates the proposed methodology with explanations of technical details; Section 7.4 describes the details of two experimental

setups; Section 7.5 presents the experimental results; Section 7.6 investigates the robustness of the proposed approach against different amounts of crack opening; Section 7.7 compares the difference of the proposed approach with traditional edge detection-based crack detection methods; and Section 7.8 concludes the study.

7.2 Methodology

Figure 66 illustrates the overall methodology of the proposed approach, with some technical details discussed in the rest of this section. All vision algorithms are based on intensity images and are implemented through the MATLAB Computer Vision System Toolbox (MathWorks, 2017). As a demonstration, suppose a steel plate is subject to a fatigue crack under a repetitive fatigue load F, as shown in Figure 66a. The steel plate is under a lower fatigue load F_1 at the first image collection, while the load increases to F_2 thereafter. Typical non-crack edges (e.g. dust, rust, or corrosion marks) are also illustrated. The fatigue load F would induce breathing behavior to the fatigue crack. Specifically, the opening of the fatigue crack changes under different levels of fatigue loading, as demonstrated as different line thicknesses in Figure 66a.

To begin, a hand-held camera is first applied to take two input images of the steel plate under fatigue load F, denoted Image 1 and Image 2, such that different amounts of crack openings can be captured by these two images. As the camera poses of these two images may be different due to the unfixed camera, directly overlapping two images to uncover the fatigue crack may not yield satisfactory result.

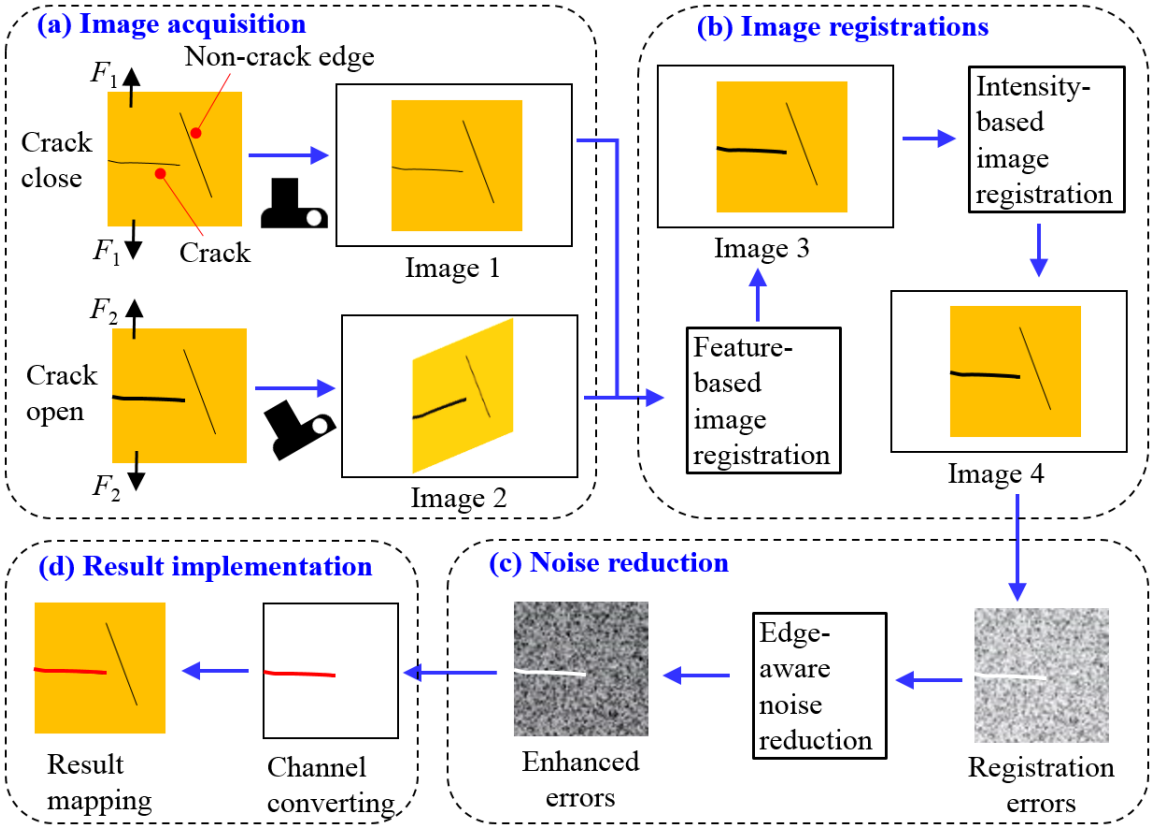

Figure 66. Overview of the methodology for crack detection: (a) image acquisition; (b) image registrations; (c) noise reduction; and (d) result implementation. F_1 and F_2 are the applied fatigue load ($F_1 < F_2$).

To achieve robust crack detection, two image registration processes are adopted in a successive manner, denoted the feature-based and intensity-based image registrations in Figure 66b, respectively. Successive application of the two image registration processes allows the misalignment between the two images gradually reduced. At the end, Image 2 can be ultimately registered to a new image (Image 4) which shares the same coordinate system with Image 1.

Next, the difference between Image 1 and 4 is directly compared by computing the registration errors, as shown in Figure 66c. In this study, the registration error is defined as the absolute intensity difference between two images. In particular, the pixels with exactly matched intensities of exactly matched pixels are illustrated as 0 (black) in the registration errors; while intensities of unmatched pixels are in the region of 1 to 255 (grey to white), depending on the level of discrepancy. The differential opening of the crack between Image 1 and 4 provokes

significantly higher intensities (i.e. a white line) in the registration error, providing an intuitive picture for fatigue crack detection. On the other hand, the non-crack edges (e.g. dust, rust, or corrosion mark) remain the same between Image 1 and 4, hence would be eliminated in the registration errors.

Since processing error and noise are inevitable in above procedures, the registration errors are enhanced through an edge-aware noise reduction algorithm, as shown in Figure 66c. The algorithm can effectively eliminate the noise texture in the background while still preserve the edge features in the registration errors. After noise reduction, the results are converted from black-white color spectrum to a white-red spectrum and further overlapped on Image 1 to visualize the location of detected fatigue crack (Figure 66d).

7.2.1 Image acquisition

A consumer-grade digital camera is required for image acquisition. In this study, a Nikon D7100 camera and a Sigma 17-50 mm lens with the auto shooting mode are adopted unless stated otherwise. A typical distance of 20 cm is applied between the camera and the monitored structure, although a larger distance could be feasible if a higher resolution camera is applied. The camera is held by hands during image acquisitions. Two images should be captured for monitored structure under the repetitive fatigue load without obstruction. Ambient lighting conditions are generally acceptable. Camera calibration is not required in this study.

7.2.2 Feature-based image registration

The purpose of feature-based image registration is to align two images taken from different camera poses to the same coordinate system through rigid-body transformation. Figure 67 demonstrates this process using two images of a concrete girder. Two input images (denoted Image A and B) are first collected under different camera poses, as shown in Figure 67a and b.

Then, Shi-Tomasi features (Shi, 1994) are extracted in Image A. The Shi-Tomasi features are based on the unique intensity change at a localized region in both horizontal and vertical directions, as illustrated in Figure 67c to e. Next, the Kanade-Lucas-Tomasi (KLT) tracker (Tomasi et al., 1991; Lucas et al., 1981) is adopted to find matched Shi-Tomasi features (i.e. correspondences) between the two input images. The initial matched features are shown in Figure 67f and g, where red circles are the features in Image A and green crosses are features in Image B. Utilizing the matched features, the maximum likelihood estimation sample consensus (MLESAC) algorithm (Torr and Zisserman, 2000) is performed to estimate a projective geometric transformation matrix, which describes the geometric distortion between Image A and B. Based on the transformation matrix, Image B can be registered to a new image (Image C in Figure 67h) so that Image C and A share the same coordinate system. This alignment can also be confirmed through the matched features between Image C and A, as shown in Figure 67i and j.

The feature-based image registration in this study is flexible in terms of implementation. For instance, instead of Shi-Tomasi features adopted in the proposed approach, other types of features could also serve as correspondences for feature matching. Previous work (Kong and Li, 2018) has investigated features from accelerated segment test (FAST) (Rosten and Drummond, 2015), Harris-Stephens (Harris and Stephens, 1998), Binary robust invariant scalable keypoints (BRISK) (Leutenegger and Siegwart, 2011), and speeded up robust features (SURF) (Bay et al., 2006), and concluded that all these features had sufficient capabilities to detect scale invariant features for aligning two input images. A more comprehensive comparison of most common types of features for feature-based image registration can be found in Tareen and Saleem (2018). In addition, the tracking algorithm is not tied to a particular type of features. Besides Shi-Tomasi features and the KLT tracker adopted in this study, other combinations can also be utilized.

Examples include Harris-Stephens feature associated with KLT tracker proposed by Yoon et al. (2016), and SIFT features associated with descriptor vectors-based tracker proposed by Khuc and Catbas (2017).

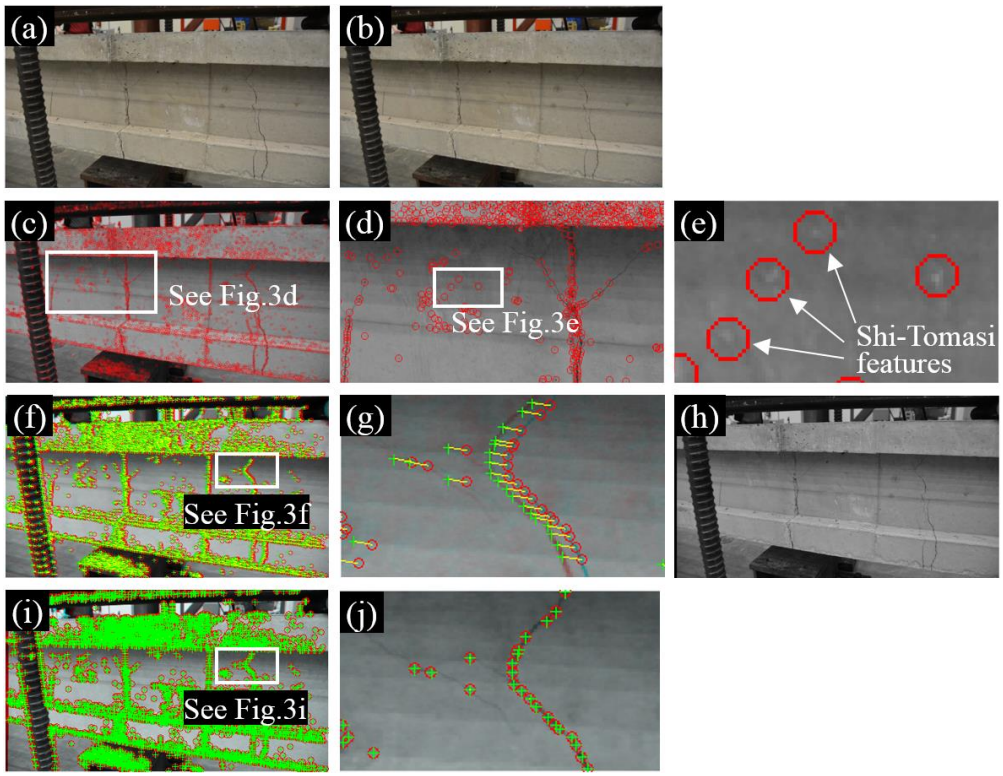

Figure 67. Demonstration of feature-based image registration: (a) input Image A; (b) input Image B; (c) to (e) Shi-Tomasi features in Image A; (f) and (g) the matched Shi-Tomasi features between Image A and B; (h) Image C; (i) and (j) the matched features between Image A and C.

7.2.3 Intensity-based image registration

Unlike rigid-body transformation through feature-based image registration, intensity-based image registration is a non-rigid image transformation procedure. To explain, suppose two images of a human hand, denoted Image A and B, are collected under different wrist rotations, as shown in Figure 68a and b. These two images are collected by a smartphone camera (4th generation Moto G Play) and then downsized to 816 pixels by 612 pixels. Now we want to register Image B to a new image that matches the intensity distribution of Image A. As illustrated in Figure 68b, in order to complete the registration process, the hand in Image B should be subject

to a combined movement of rotation and translation. Feature-based image registration is unable to solve this problem as the hand has a non-rigid geometric distortion between Image A and B. Instead, intensity-based image registration is performed to register Image B to Image C (Figure 68c) such that the hand posture in Image C matches that in Image A. In the registration procedure, the displacement field that aligns Image A to Image B can be also generated. Figure 68d and e show the displacement fields in both x and y directions. The two directions are denoted in Figure 68a. Intensity-based image registration has been widely applied in the medical imaging (Oliveira and Tavares, 2014). The demon-based image registration algorithm (Thirion, 1998; Vercauteren et al., 2009] is adopted in this study, while other image registration algorithms could also be applicable.

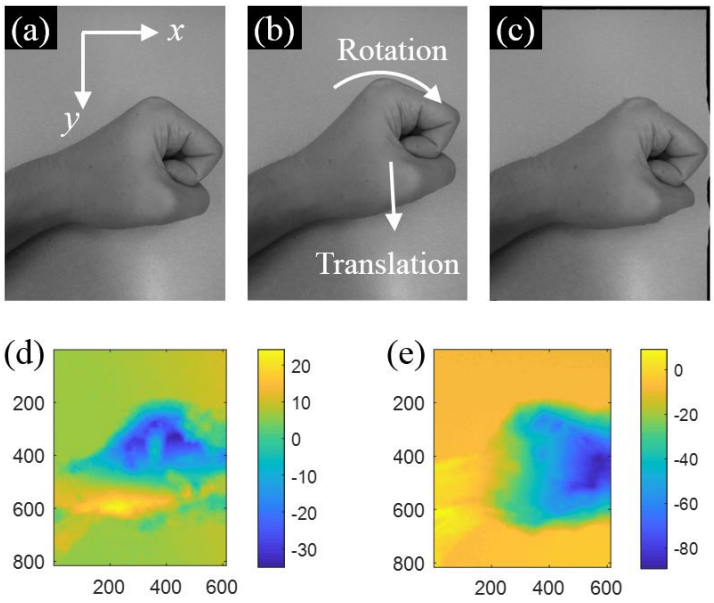

Figure 68. Demonstration of intensity-based image registration: (a) input Image A; (b) input Image B; (c) newly-registered Image C; (d) displacement field in *x* direction; and (e) displacement field in *y* direction. Horizontal and vertical axes in Figure 68d and e are 2D pixel dimensions of the image, while the unit of the color bars is pixel.

It should be noticed that feature-based image registration can effectively aligns two input images into the same coordinate system based on correspondences. However, small misalignments are commonly associated with feature-based image registration (Zitova and

Flusser, 2003). The intensity-based image registration, on the other hand, is able to adjust small misalignments but may have difficulties to handle significant misalignments. By adopting these two image registration processes in a successive manner, the misalignments between two input images can be effective reduced in two steps.

7.2.4 Edge-aware noise reduction

The purpose of edge-aware noise reduction is to reduce the noise content of a digital image while preserving the edge features. Figure 69 shows a comparison between edge-aware noise reduction and the traditional filtering method. The image of a prestressed concrete girder described in Section 7.2.2 is adopted for this investigation. The input image (Figure 69a) contains a scene with complex textures. For illustration purpose, these textures are categorized as edge features (e.g. concrete surface cracks and boundary of the reinforced bar) and background noise (e.g. surface marks on the concrete surface). To remove the background noise, two approaches are conducted including a 2D Gaussian filter with a standard deviation σ of 1, 5, and 10, as shown in Figure 69b to d, and the edge-aware noise reduction method (Paris et al., 2011; Aubry et al., 2014) with a detail smoothing factor α of 1.5, 3, and 5, as shown in Figure 69e to g. A higher factor α leads to more severe smoothing effect in the background noise. As demonstrated in this comparison, the traditional 2D Gaussian filter effectively reduced the noise level of the input image by blurring the textures. As a tradeoff, the edge features (e.g. the surface cracks and reinforced bar) would be contaminated as well. On the other hand, the edge-aware noise reduction method can remove the noise content without eroding the edge features, hence is selected as the method for removing the noise content of registration errors in the proposed approach.

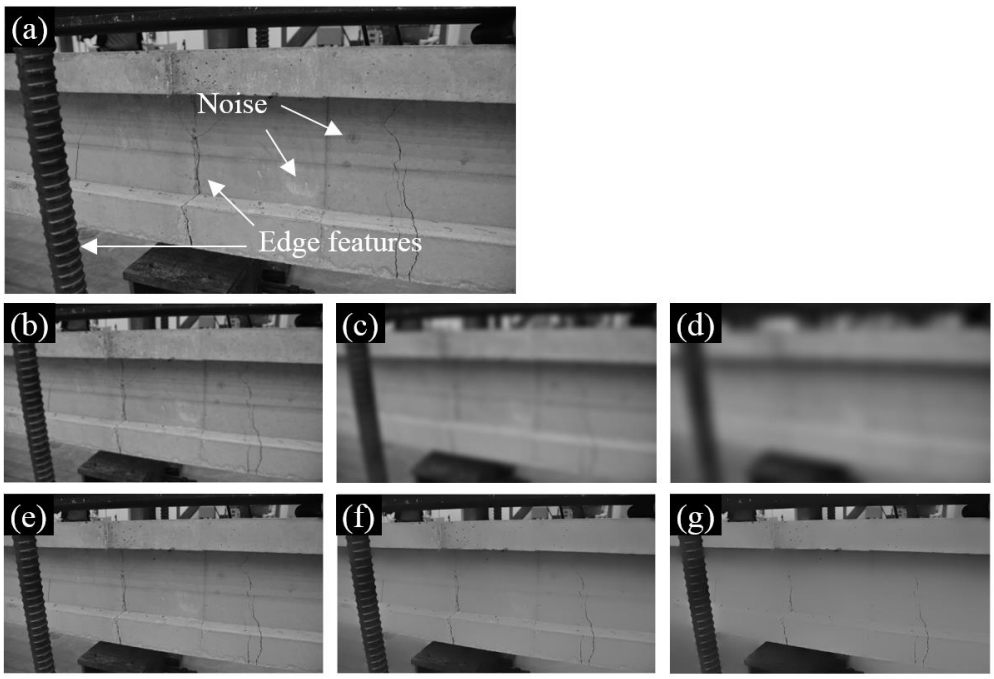

Figure 69. Demonstration of edge-aware noise reduction: (a) input image of a concrete girder; (b) to (d) noise reduction through the 2D Gaussian filter under σ = 1, 5, and 10; (e) to (g) noise reduction through the edge-aware noise reduction under α = 1.5, 3, and 5.

7.3. Experimental details

7.3.1 Compact specimen

The first test setup is a compact, C(T), specimen fabricated by A36 steel for the experimental investigation. The specimen is a single edge-notched steel plate loaded in tension force through two clevises, as shown in Figure 70. The specimen was 6.4 mm in thickness and its detailed dimensions can be found in Kong et al. (2017). Prior to the experiment, the specimen had been fatigue loaded and an existing fatigue crack was found on the surface of the specimen with a length of 53.3 mm (Figure 70b). A closed-loop servo-hydraulic uniaxial load frame was adopted for applying the fatigue load. The fatigue load cycles were a 0.5 Hz harmonic signal with a range of 3.0 kN to 6.5 kN. A more detailed discussion about loading protocol design can be found in Kong et al. (2017). To measure the opening of the crack, a clip-on displacement gauge (Epsilon

3541-0030-150T-ST) was installed at the front face the C(T) specimen, as shown in Figure 70b. Regular indoor lighting condition was applied during the image collection.

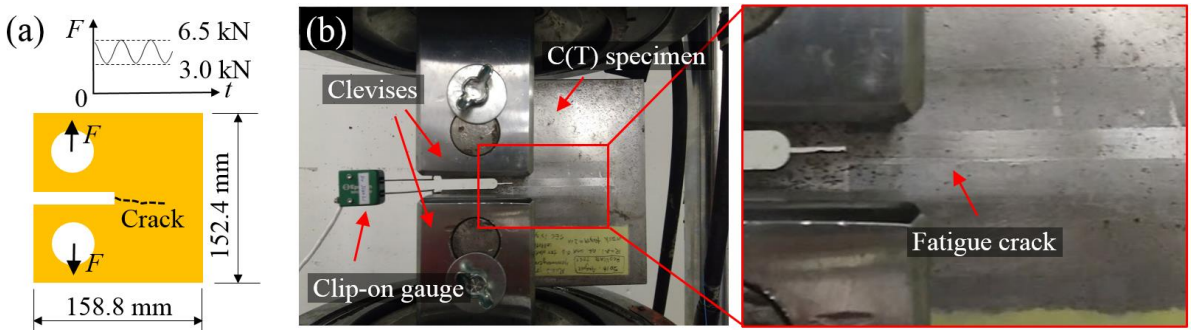

Figure 70. (a) Schematic of the test setup; and (b) photo of the test setup. *F* is the applied fatigue load cycles; *t* is time.

7.3.2 Bridge girder to cross frame specimen

The second test setup is a bridge girder to cross-frame connection specimen. The design of the test specimen was to simulate the typical structural layout of fatigue susceptible regions of steel girder bridges built prior to the mid-1980s in the United States. Figure 71a shows a typical steel girder bridge in the field where the cross-frames were mainly used to provide lateral support to the longitudinal girders during construction. The repetitive traffic load caused by passing vehicles would induce a differential vertical movement between two adjacent girders, causing out-of-plane movement at the fatigue-susceptible region denoted in Figure 71b. As a result, fatigue cracks are commonly found in this region. A more detailed discussion about the mechanism of distortion-induced fatigue cracks can be found in (Jajich and Schultz, 2013).

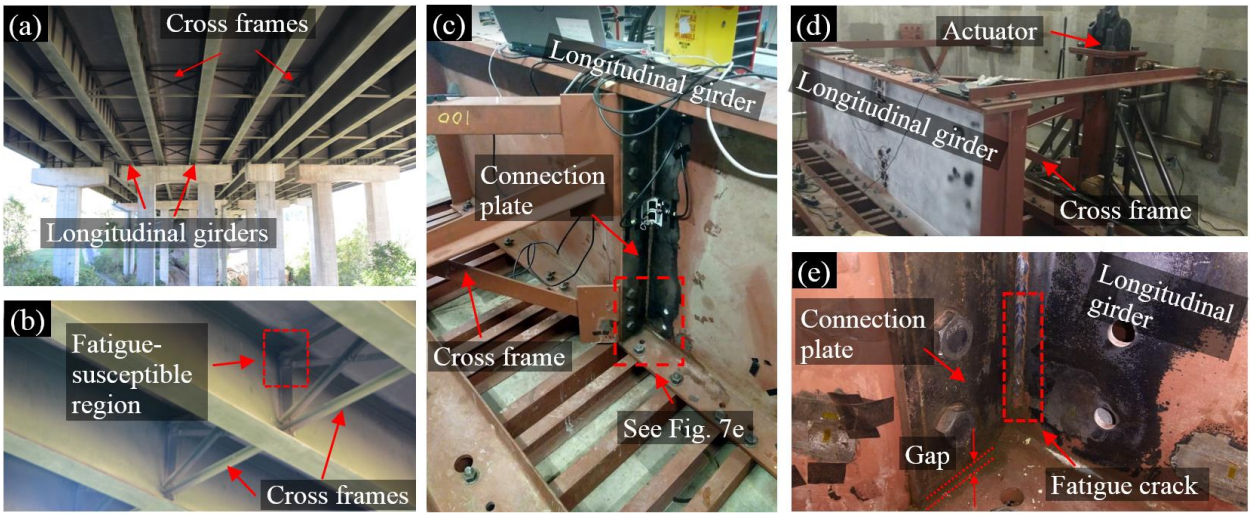

Figure 71. (a) A typical steel girder bridge in the field; (b) fatigue-susceptible region at the girder to cross-frame connection; (c) exterior view of the large-scale girder to cross-frame connection; and (d) interior view of the test specimen.

Figure 71c shows the setup of the test specimen. The bridge girder was mounted upside-down to the lab floor in order to simulate the constraint of the bridge deck. A cross frame was installed to the girder through a connection plate. The connection plate was fillet welded to the web of the girder with a gap left between the bottom of the connection plate and the bottom flange (Figure 71e). On the far end of the cross frame, an actuator was attached to apply vertical fatigue load, as shown in Figure 71d. Prior to the experimental test, the specimen had been fatigue loaded with 2.7 million cycles, leading to an existing vertical fatigue crack between the girder web and the connection plate (Figure 71e). During the test, the fatigue load cycles were a 0.5 Hz harmonic signal with a range of 0 kN to 11.1 kN. A detailed description of the test specimen can be found in Yu et al. (2017).

7.4. Experimental results

7.4.1 Crack detection result of the C(T) specimen

The experimental results of the C(T) specimen are shown in Figure 72 and Figure 73. Figure 72 demonstrates the major steps of the image processing procedure, while Figure 73 offers close-up results at three typical image patches. As shown in Figure 72a, Patch 1 is at the boundary of the

C(T) specimen with a region of 50 pixels by 50 pixels; Patch 2 covers the fatigue crack with a region of 50 pixels by 50 pixels; Patch 3 contains the gap between the clevis and the rod with a region of 100 pixels by 100 pixels. Notice that all three image patches contain edge-like features, but only Patch 2 represents the true fatigue crack.

Our proposed approach begins with image acquisition. Two input images (Image 1 and 2 in Figure 72a and b) were first collected by the aforementioned hand-held digital camera when the specimen was under fatigue load cycles. The breathing crack under fatigue load induces a slightly larger crack opening at Image 2, while other surface textures on the C(T) specimen remain unchanged. This can be also confirmed in Figure 73a and b, where only the crack at Patch 2 become thicker but other textures in Patch 1 and 3 are same.

Figure 72c shows the initial intensity comparison of the two input images. Black color (0 intensity) represents exactly matched pixels and grey color (intensity from 1 to 255) represents unmatched pixels. Because the two input images were taken by a hand-held camera, the camera poses of these two input images are not the same, hence a geometric distortion exists between the two input images. As shown in Figure 73a and b, surface textures of the C(T) specimen in all patches are subjected to a rigid-body movements. Directly overlapping the two input images (Figure 72c and Figure 73c) to uncover the fatigue crack would be challenging.

Next, Image 2 was rigidly registered to Image 3 through feature-based image registration such that Image 3 and 1 share the same coordinate system. Figure 72d shows the newly-registered Image 3. The misalignments between Image 1 and 3 are significantly reduced. This also can be confirmed by comparing image patches in Figure 73a and d. However, some misalignments still exist in the registration errors between Image 1 and 3 (Figure 72e), especially around the boundary of the clevis pins (Patch 3 in Figure 73e).

To reduce registration errors, Image 3 is further registered to Image 4 through intensity-based image registration. During this process, Image 3 is non-rigidly stretched in order to match the intensity distribution of Image 1. Results of the newly-registered Image 4 can be found in Figure 72f and Figure 73f, and the registration errors between Image 1 and 4 are shown in Figure 72g and Figure 73g. As can be seen in above figures, the breathing fatigue crack provokes significant registration errors due to the differential crack opening between the two input images. On the other hand, other surface textures of the C(T) specimen do not induce errors as these features remain the same.

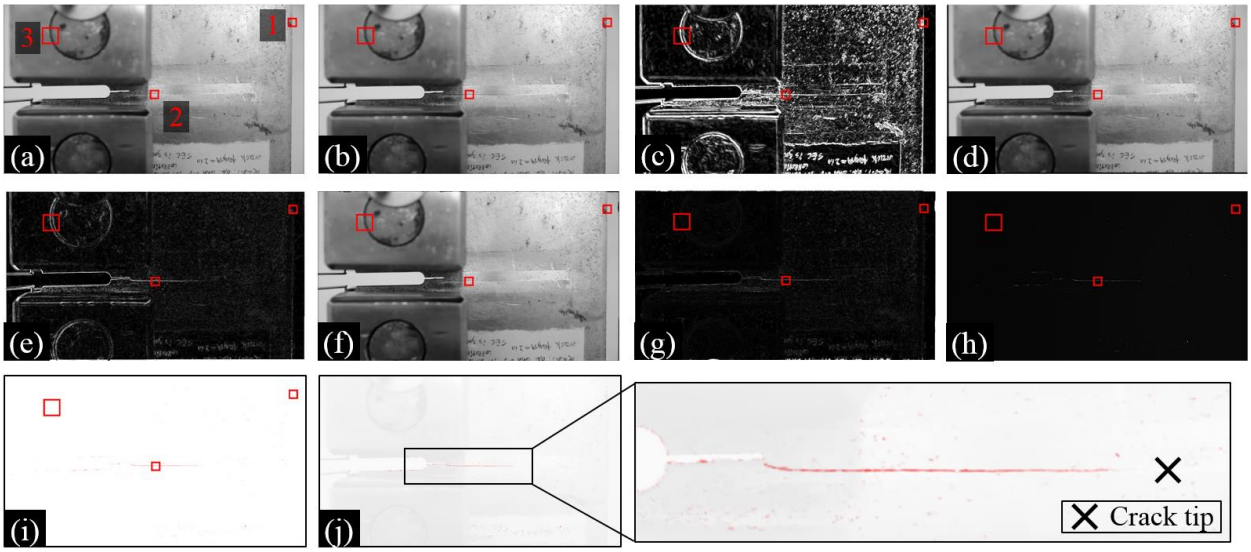

Figure 72. Experimental results of the C(T) specimen: (a) input image 1 when the crack closed; (b) input image 2 when the crack opened; (c) initial intensity comparison between Image 1 and 2; (d) Image 3 after feature-based image registration; (e) registration errors between Image 1 and 3; (f) Image 4 after intensity-based image registration; (g) registration errors between Image 1 and 4; (h) enhanced errors after edge-aware noise reduction; (i) results after channel converting; and (j) final fatigue crack detection result.

Finally, edge-aware noise reduction is applied to the registration errors in order to remove the background noise while still preserving the edge features. Results of the enhanced registration errors are shown in Figure 72h and Figure 73h. These results are further converted into a white-red spectrum (Figure 72i and Figure 73i). The final fatigue crack detection result is shown in Figure 72j where the tip of the crack is marked as black cross identified by human eyes.

An important observation from the above experimental results is that our proposed approach can produce reliable crack detection result even the true fatigue crack is surrounded by other non-crack edges. For instance, the non-crack edges in Patch 1 and 3, which are the boundary of the C(T) specimen and gap between the clevis and pin, can be recognized by our approach as non-crack features hence are eliminated in the crack detection results. Distinguishing these non-crack edges from the true fatigue crack could be challenging for traditional edge detection-based crack detection methods.

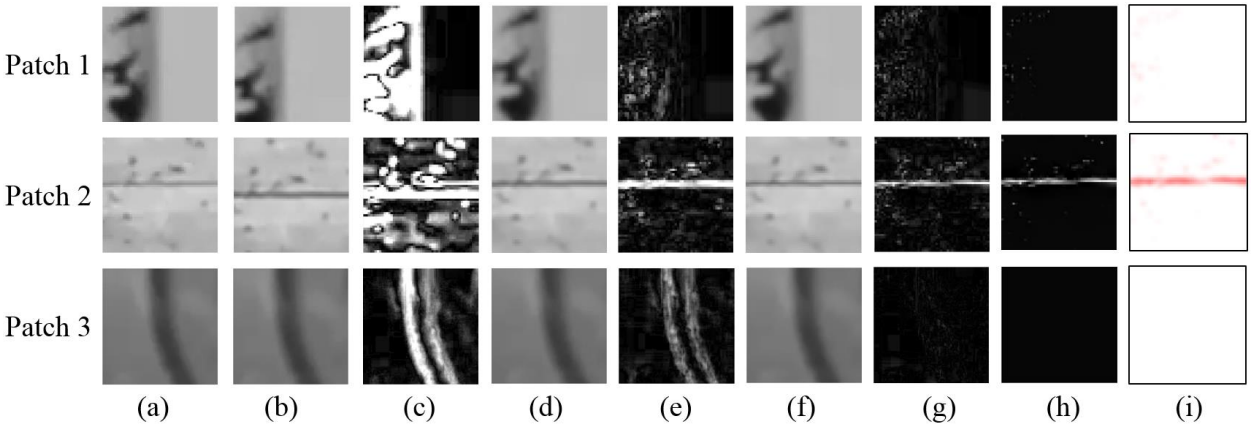

Figure 73. Close-up results of Figure 72 at three image patches. Locations of the patches are defined in Figure 72a. (a) to (i) correspond to (a) to (i) in Figure 72.

7.4.2 Crack detection result of the bridge girder specimen

Two input images of the fatigue-susceptible region (denoted in Figure 71e) were collected when the specimen was under fatigue load. Figure 74 and Figure 75 illustrate the experimental results. Three typical image patches are selected in Figure 74a to offer close-up views of the results. Particularly, Patch 1 is a 100 pixels by 100 pixels region that covers a steel bolt on the connection plate; Patch 2 is a 50 pixels by 50 pixels region over the fatigue crack; Patch 3 is a 50 pixels by 50 pixels region on the web of the steel girder. Notice that all three image patches contain edge-like features, but only Patch 2 represents the true fatigue crack.

As shown in Figure 74c and Figure 75c, the two input images (Image 1 and 2) are subjected to geometric distortion, leading to misalignments in the intensity comparison. These misalignments can be gradually reduced through applying the feature-based image registration (Figure 74e and Figure 75e), intensity-based image registration (Figure 74g and Figure 75g), and edge-aware noise reduction (Figure 74h and Figure 75h). The final crack detection result is shown in Figure 74j where the tip of the crack is marked as black cross identified by human eyes. Some false-positive detection results can be found between the connection plate and the bottom flange. This is due to the relative free rotation between these two structural components, creating differential features in the two input images. Nevertheless, utilizing prior knowledge of the structural configuration, the false-positive results associated with the gap region can be eliminated from the crack detection results.

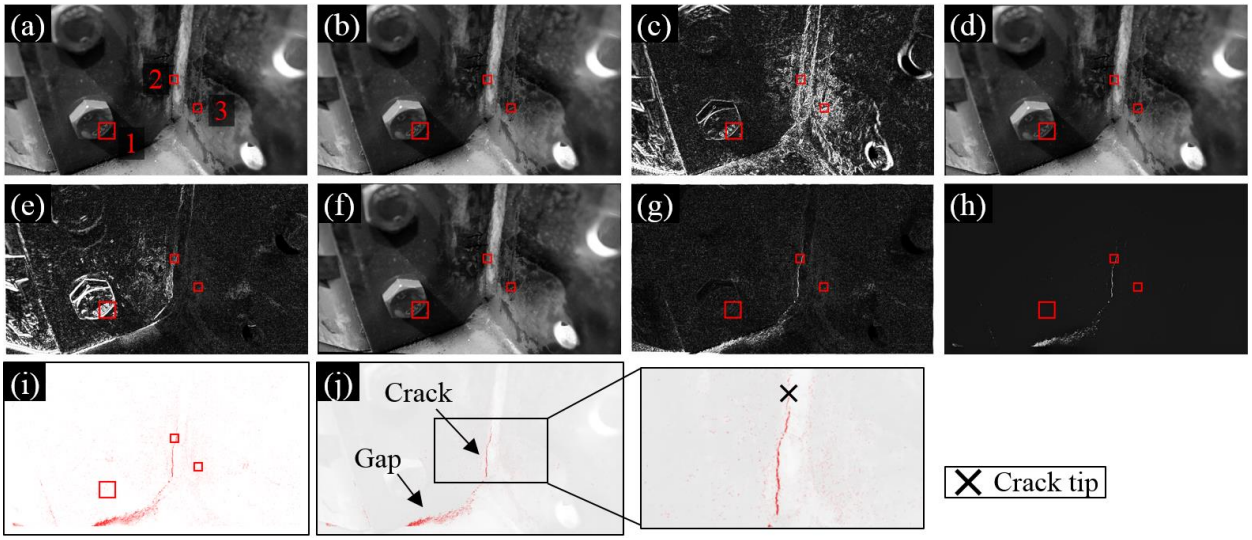

Figure 74. Experimental results of the bridge girder specimen: (a) input image 1 when the crack closed; (b) input image 2 when the crack opened; (c) initial intensity comparison between Image 1 and 2; (d) Image 3 after feature-based image registration; (e) registration errors between Image 1 and 3; (f) Image 4 after intensity-based image registration; (g) registration errors between Image 1 and 4; (h) enhanced errors after edge-aware noise reduction; (i) results after channel converting; and (j) final fatigue crack detection result.

As shown in Figure 75a, many edge-like features exist in the three image patches. In particular, Patch 2 contains multiple edge-like features, while only one of them represents the true fatigue crack. The experimental results validate that the proposed approach can effectively

distinguish the true fatigue crack from other non-crack edges, hence leading to more robust performance than traditional crack detection methods that are based on edge detection techniques.

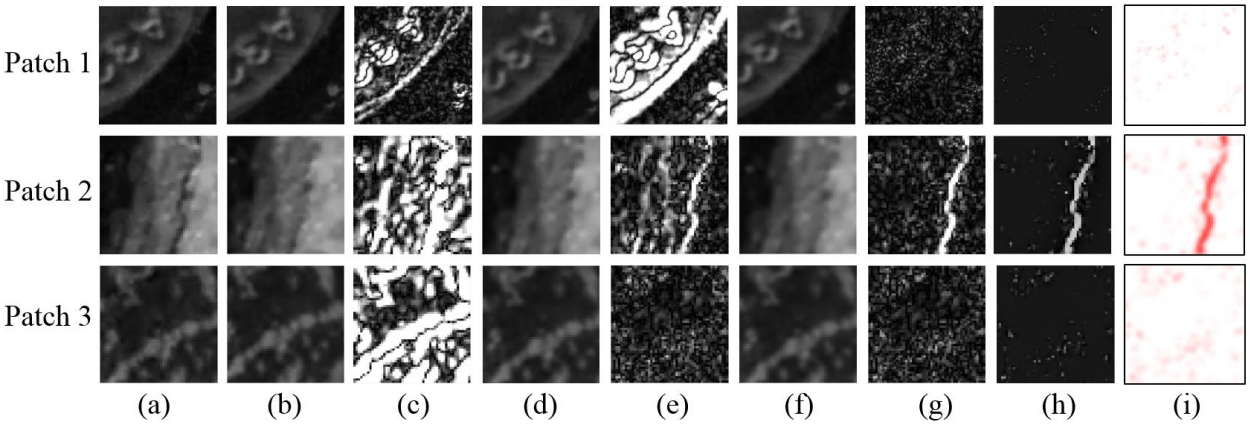

Figure 75. Close-up results of Figure 74 at three image patches. Locations of the patches are defined in Figure 74a. (a) to (i) correspond to (a) to (i) in Figure 74.

7.5. Robustness evaluation

One critical research question in this study is the performance of the proposed approach when the input images capture only partial opening of the breathing crack. Results presented in Section 7.4 are based controlled laboratory settings. More specifically, sine the fatigue load was known as being applied as a 0.5 Hz harmonic cycles, the two input images were collected at the approximate moments when the crack reached its maximum and minimum openings identified by human eyes, meaning the full opening of the crack was utilized in the algorithm. For detecting fatigue cracks in steel bridges in the field, the fatigue load (i.e. passing vehicles) is not known as *a priori*, hence the two input images cannot guarantee to capture the minimum and maximum crack openings, respectively. The motivation of this section is to investigate the performance of the proposed approach when only partial opening of the breathing crack is captured by the input images.

7.5.1 Method

Figure 76 illustrates the method for the robustness evaluation. The C(T) specimen described in Section 7.4.1 was adopted for this investigation. A 2-sec video stream of the C(T) specimen was collected by the aforementioned camera using hand-held mode at a rate of 30 fps (Figure 76a). Subsequently, the opening of the crack at the left edge of the specimen was tracked, as shown in Figure 76b. As a brief explanation of the tracking procedure, two small image windows with 50 pixels by 50 pixels were deployed at the each side of the notch, denoted top and bottom windows, respectively. Shi-Tomasi (1994) features were then extracted within each window throughout the 2-sec video. The vertical movements of these feature points can be tracked through the KLT tracker (Tomasi and Kanade, 1991; Lucas and Takeo, 1981) in terms of pixels. The average vertical movement among all feature points within each window was computed, denoted *y_top* and *y_bottom*, to represent the movement of top and bottom windows, respectively. Finally, by subtracting *y_top* and *y_bottom*, the crack opening at the front face of the specimen can be obtained. Based on the tracked crack opening response, a series of frames were selected within one full crack breathing cycle, denoted as f_i, f_j, and f_k in Figure 76c. The corresponding video frames at f_i, f_j, and f_k were then retrieved from the collected video stream (Figure 76d). The combinations of each two video frames in all selected frames (e.g. f_i and f_j, or f_i and f_k) would form pairs of two input images that only partially captured the opening of the breathing crack. Utilizing the proposed crack detection approach, the performances of these selected cases can be evaluated (Figure 76e).

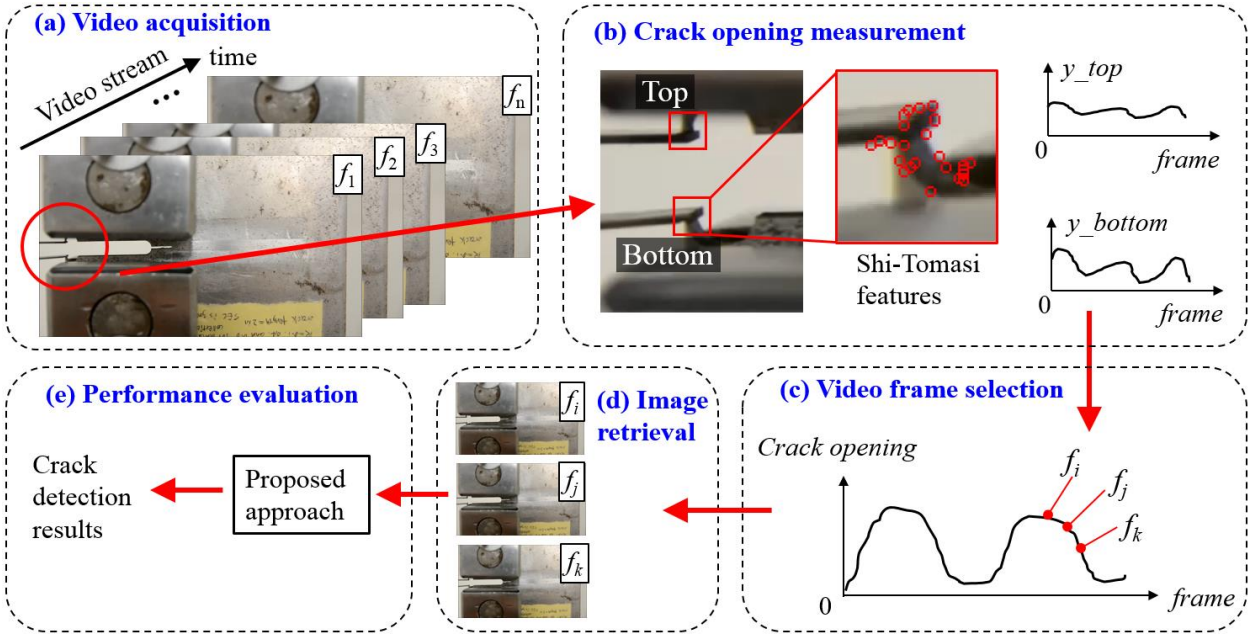

Figure 76. Methodology of the robustness analysis: (a) video acquisition; (b) crack opening measurement; (c) video frame selection; (d) image retrieval; and (e) performance evaluation. *f* represents video frame; *y_top* and *y_bottom* are the average vertical movements of the feature points in terms of pixels.

7.5.2 Experimental procedure

Figure 77a illustrates the ground truth measurement of the crack opening at the left edge of the C(T) specimen obtained by a clip-on displacement gauge (see Figure 70b). The crack opening is consists of 0.5 Hz harmonic cycles with a peak-to-peak amplitude of 0.233 mm. Utilizing the crack opening tracking methodology described in Section 7.5.1, the camera-based crack opening measurement at the same location of the specimen is shown in Figure 77b in terms of pixels. Despite slight noise content, a harmonic signal is also obtained. The crack opening reaches its maximum at around the 25th frame, while reduces to its minimum at around the 55th frame. Hence, the duration of a half cycle is about 30 frames (1 sec), which agrees well with the clip-on gauge measurement (Figure 77a).

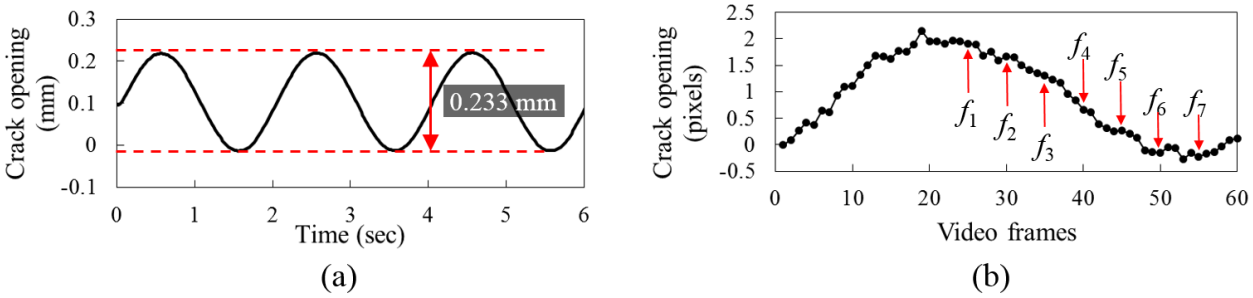

Figure 77. Crack opening measurement by (a) clip-on gauge; and (b) camera. The two measurements are not synchronized.

Utilizing the results in Figure 77b, 7 video frames are selected at the 25th, 30th, 35th, 40th, 45th, 50th, and 55th frames, denoted as frame f_1 to f_7 in Figure 77b. The corresponding video frames are shown in Figure 78, with close-up images presented in Figure 79 and Figure 80. Patch 1 is a 500 pixels by 100 pixels region covering majority of the fatigue crack; Patch 2 is a 50 pixel by 50 pixel localized region within Patch 1. As can be found in Figure 79 and Figure 80, the thickness of the crack gradually decreases from frame f_1 to f_7. In addition, due to the hand-held mode of the camera, video frames are affected by rigid-body movements as shown in Figure 80.

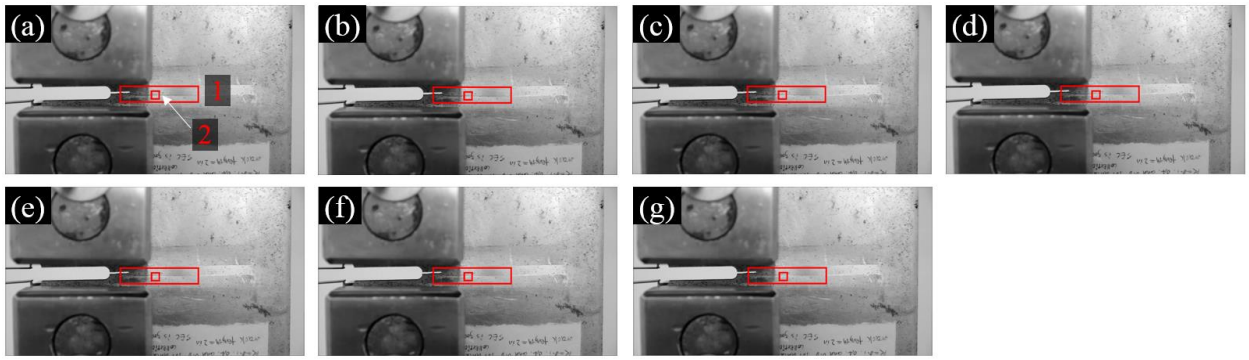

Figure 78. (a) to (g): frame f_1 to f_7 retrieved from the collected video stream.

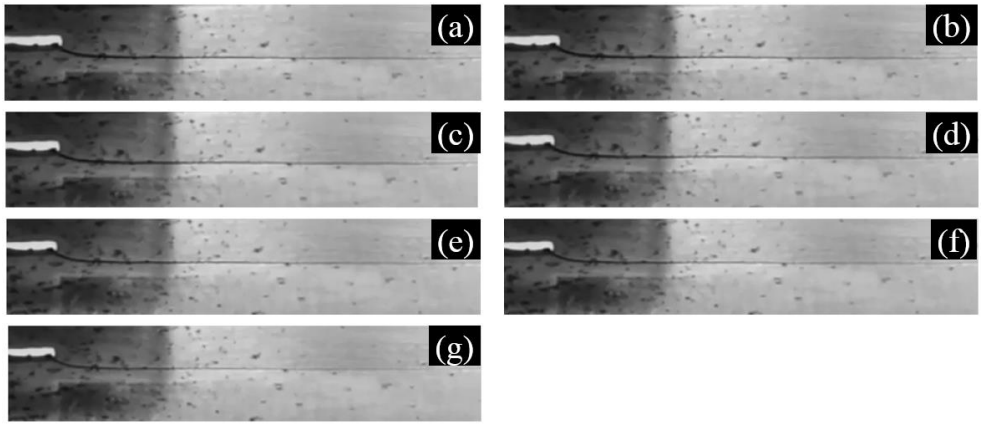

Figure 79. Close-up views of the video frames in Figure 78. Locations of the image patches are defined as Patch 1 in Figure 78a. (a) to (g) correspond to (a) to (g) in Figure 78.

Figure 80. Close-up views of the video frames in Figure 78. Locations of the image patches are defined as Patch 2 in Figure 78a. (a) to (g) correspond to (a) to (g) in Figure 78.

7.5.3 Results

Table 6 summaries the test matrix in this investigation, where frame f_1 is treated as the reference frame and paired with frame f_2 to f_7 to form six pairs of input images for analysis. As a result, 6 test cases are established, denoted Test 1 to Test 6 in the table. Test 1 (f_1 and f_2) only captures a very limited cracking opening, while Test 6 (f_1 and f_7) captures the full response of the breathing crack, i.e. a peak-to-peak amplitude of 0.233 mm at the left edge of the specimen.

Table 6. Test matrix for robustness evaluation

Test case	Selected input video frames	Results
Test 1	f_1 and f_2	Figure 81a and Figure 82a
Test 2	f_1 and f_3	Figure 81b and Figure 82b
Test 3	f_1 and f_4	Figure 81c and Figure 82c
Test 4	f_1 and f_5	Figure 81d and Figure 82d
Test 5	f_1 and f_6	Figure 81e and Figure 82e
Test 6	f_1 and f_7	Figure 81f and Figure 82f

Figure 81 shows the crack detection results of Patch 1 (denoted in Figure 78a) after applying the proposed approach with close-up views (i.e. Patch 2) illustrated in Figure 82. As can be seen in the figures, the intensities of the crack features become higher from Test 1 to Test 6. The result indicates capturing a larger crack opening in the two input images yields better crack detection quality. Nevertheless, despite larger noise content, the proposed approach still identified the fatigue crack even two input images capture only a very limited opening of the breathing crack such as in Test 1.

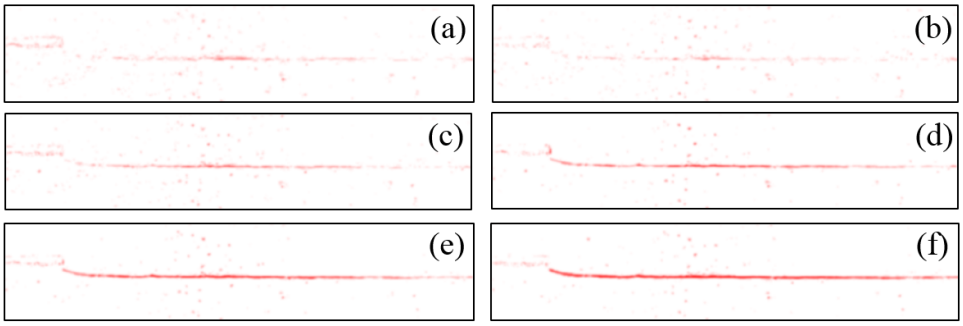

Figure 81. Crack detection results of all six test cases. (a) to (f) refer to Test 1 to Test 6 in the table. The location of the image patch is defined as Patch 1 in Figure 78a.

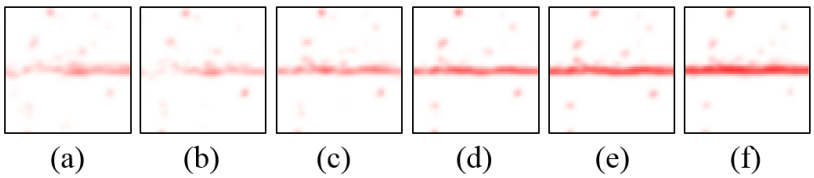

Figure 82. Close-up view of crack detection results of all six test cases. (a) to (f) refer to Test 1 to Test 6 in the table. The location of the image patch is defined as Patch 2 in Figure 78a.

7.6 Comparative evaluation

A comparative evaluation was performed in this section to demonstrate the fundamental difference of the proposed approach with traditional edge detection-based crack detection methods. For illustration purpose, Canny edge detector (1987) was adopted using the bridge test setup. Figure 83a shows the input image for edge detection and Figure 83b shows the detection results. As can be seen in the figure, many edge features are identified by the Canny edge detector, while the true fatigue is submerged in these edge features in this case. Distinguishing

the true fatigue crack from many non-crack edges could be challenging and may require further processing. On the other hand, the proposed approach can robustly identify the fatigue crack as shown in Figure 83c.

It should be noticed that the nature of the proposed approach is based on sensing breathing cracks. To ensure the success of the proposed approach, the monitored structure must be under a repetitive fatigue load during image collections. However, this requirement could be easily fulfilled in field applications, as most civil structures which suffer from fatigue cracks are likely continuing to carry the fatigue loading under their operational life.

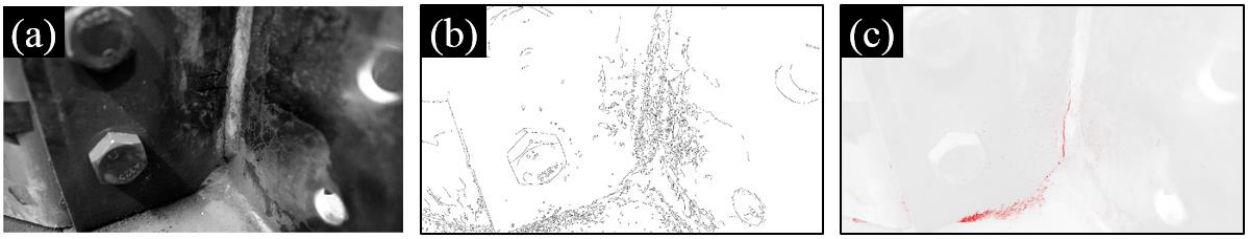

Figure 83. Results of the comparative study where (a) the input image for edge detection; (b) Canny edge detection result; and (c) result of the proposed method.

7.7 Conclusions

This chapter presented a non-contact vision-based fatigue crack detection methodology based on image overlapping. The proposed approach starts with the collection of two input images of the monitored structure under repetitive fatigue load, followed by fatigue crack identification through comparison, enhancement, and visualization of differential image features caused by crack breathing. The performance of the proposed approach has been experimentally validated through two laboratory tests including a small-scale steel C(T) specimen and a large-scale bridge girder to cross-frame connection. The tests indicate that proposed approach can successfully detect the fatigue cracks, even the true cracks were surrounded by other non-crack edges (e.g. structural boundary, bolt marks, and complex surface textures). In addition, a robustness evaluation has been performed to investigate the performance of the proposed approach under

different crack openings. Results indicated the approach was still able to identify the crack when the two input images captured only a very limited crack opening, showing great potential and flexibility of the proposed approach for field implementation under unknown fatigue loading. Future work will focus on integrating the proposed approach with UAVs to achieve autonomous fatigue inspection of civil infrastructure.

Chapter 8 Conclusions and Future Work

8.1 Conclusions

This dissertation investigated fatigue crack detection of steel highway bridges through advanced structural health monitoring technologies. In particular, two sensing approaches have been proposed including 1) a large-area strain sensing skin in form of soft elastomeric capacitor (SEC); and 2) non-contact vision-based crack detection methods. The dissertation begins with a literature review to discuss the existing fatigue damage inspection practice in steel highway bridges in the United States and the current challenges for fatigue inspection. The state-of-the-art fatigue crack sensing technologies in the past decades and their limitations were also reviewed.

Thereafter, discussion was focused on the SEC technology for fatigue crack sensing. The investigation spans from the theoretical sensing principle to the practical bridge engineering applications, which included the following three aspects: 1) numerically simulating the response of the SEC under fatigue cracking; 2) developing and validating a long-term, robust, SEC-based crack monitoring algorithm through small scale specimens; and 3) large-scale validation for sensing large fatigue susceptible region through a SEC array.

In terms of numerical simulation, a computational approach for numerically predicting the response of the SEC has been established. Results validated that the proposed approach can accurately simulate the capacitance response of the SEC under fatigue cracking. The established approach directly links the signal of the sensor to fatigue crack geometry, which will be very useful for infrastructure operators and managers in carrying out condition-based maintenance procedures.

In the development of the crack monitoring algorithm, a novel sensing algorithm has been developed through frequency analysis, which enabled a robust fatigue crack monitoring

methodology that is insensitive to long-term signal drifts and different fatigue load characteristics. The proposed crack monitoring methodology has been validated through a series of small scale C(T) specimens. Results indicated the proposed method can robustly identify the fatigue crack growth under a variety of loading characteristics. Development of this crack monitoring method has led to more reliable fatigue monitoring over the long term.

In the large-scale experimental validation, a large-scale bridge girder to cross frame connection model was adopted for the investigation. An SEC array, coupled with a data visualization method for spatially representing the fatigue damage, has been proposed to sense the fatigue damage over a large structural surface. Experimental results validated the proposed data visualization method can effectively identify the fatigue crack growth. The findings of this research study have served as the fundamental basis for the field applications of the SEC technology on steel bridges.

Next, the focus of discussion was placed on vision-based non-contact fatigue crack detection methods. Two vision-based approaches have been established in this dissertation including: 1) a video feature tracking-based fatigue sensing method; and 2) an image overlapping fatigue crack detection method.

In video feature tracking-based fatigue crack detection, a computer vision-based sensing strategy has been established using a consumer-grade digital camera. This development further allows the computer to efficiently identify fatigue cracks through a video stream and quantify crack opening with sub-millimeter accuracy. The effectiveness of this approach has been verified through laboratory fatigue tests of a small-scale steel plate and large-scale bridge connection. The proposed approach can robustly identify the crack when the crack is surrounded by crack-

like edges, covered by dust, rust, and corrosion, or visually invisible to human eyes under crack closure.

In image overlapping-based fatigue crack detection, two input images of the monitored structure under repetitive fatigue load were first collected. Then the fatigue crack was identified through comparison, enhancement, and visualization of differential image features caused by crack breathing. The performance of the proposed approach has been experimentally validated through two laboratory tests. The tests indicated that proposed approach can successfully detect the fatigue cracks.

8.2 Future work

Future work of the SEC-based fatigue crack detection will be placed on integrating the SEC with a newly-developed capacitance data acquisition board, and a wireless sensing platform to achieve wireless fatigue monitoring of steel bridges. The data acquisition system for collecting measurements of the SEC so far is based on an off-the-shelf capacitance board (ACAM Pcap02). To make the SEC technology wireless, a dedicated data acquisition board is needed for making it compatible with the wireless sensing platform. A pilot study has been performed by the Jeong et al. (2018), showing preliminary laboratory results of the newly-developed capacitance board. For the wireless sensing platform, Xnode (Zhu et al. 2018) developed by the University of Illinois Urbana-Champaign will be adopted to transfer the collected capacitance data to the base station. Finally, a field validation of the integrated monitoring solution will be carried out on a highway bridge for long-term monitoring fatigue cracks.

For the vision-based non-contact fatigue sensing technologies, the presented research work has been performed in laboratory setups. Future work will be placed on field validation in steel bridges of the proposed methods using UAVs. In the video feature tracking-based fatigue

sensing method, a challenge in field validation is to compensate the movement of the camera during video acquisition. A pilot study (Kong et al., 2018g) has been conducted through the usage of the geometric transformation such that different video frames from a handheld camera can be automatically aligned into the same coordinate system.

Reference

Abdelbarr, M., Chen, Y. L., Jahanshahi, M. R., Masri, S. F., Shen, W. M., & Qidwai, U. A. (2017). 3D dynamic displacement-field measurement for structural health monitoring using inexpensive RGB-D based sensor. *Smart Materials and Structures*, 26(12), 125016.

Abdel-Qader, I., Abudayyeh, O., & Kelly, M. E. (2003). Analysis of edge-detection techniques for crack identification in bridges. *Journal of Computing in Civil Engineering*, 17(4), 255-263.

Alavi, A. H., Hasni, H., Jiao, P., Borchani, W., & Lajnef, N. (2017). Fatigue cracking detection in steel bridge girders through a self-powered sensing concept. *Journal of Constructional Steel Research*, 128, 19-38.

American Society of Civil Engineers (ASCE). (2017). Infrastructure Report Card – Bridges, https://www.infrastructurereportcard.org/wp-content/uploads/2017/01/Bridges-Final.pdf

ASTM International. (2015). *Standard test method for measurement of fracture toughness*. ASTM International.

Aubry, M., Paris, S., Hasinoff, S. W., Kautz, J., & Durand, F. (2014). Fast local Laplacian filters: Theory and applications. *ACM Transactions on Graphics (TOG)*, 33(5), 167.

Bao Y, Kunnath SK, El-Tawil S, Lew HS (2008) Macromodel-based simulation of progressive collapse: RC frame structures *Journal of Structural Engineering*. 134 1079-91

Bay, H., Tuytelaars, T., & Van Gool, L. (2006, May). Surf: Speeded up robust features. *In European conference on computer vision* (pp. 404-417). Springer Berlin Heidelberg.

Bennett, C., Matamoros, A., Barrett-Gonzalez, R., & Rolfe, S. (2014). Enhancement of Welded Steel Bridge Girders Susceptible to Distortion-Induced Fatigue. *Final Report for Transportation Pooled-Fund Study TPF-5(189)*, June, 2014.

Biezma, M. V., & Schanack, F. (2007). Collapse of steel bridges. *Journal of Performance of Constructed Facilities*, 21(5), 398-405.

Blunt, D. M., & Keller, J. A. (2006). Detection of a fatigue crack in a UH-60A planet gear carrier using vibration analysis. *Mechanical Systems and Signal Processing*, 20(8), 2095-2111.

Cai, L., Song, L., Luan, P., Zhang, Q., Zhang, N., Gao, Q. & Zhou, W. (2013). Super-stretchable, transparent carbon nanotube-based capacitive strain sensors for human motion detection. *Scientific reports*, 3, 3048.

Canny, J. (1986). A computational approach to edge detection. *IEEE Transactions on pattern analysis and machine intelligence*, (6), 679-698.

Cha, Y. J., Choi, W., & Buyukozturk, O. (2017). Deep learning-based crack damage detection using convolutional neural network. *Computer-Aided Civil and Infrastructure Engineering*, 32(3), 2013-2014.

Cha, Y. J., Choi, W., Suh, G., Mahmoudkhani, S., & Büyüköztürk, O. (2017). Autonomous Structural Visual Inspection Using Region-Based Deep Learning for Detecting Multiple Damage Types. *Computer-Aided Civil and Infrastructure Engineering*, In press

Chen, F. C., & Jahanshahi, M. R. (2017). NB-CNN: Deep Learning-based Crack Detection Using Convolutional Neural Network and Naïve Bayes Data Fusion. *IEEE Transactions on Industrial Electronics*.

Chen, F. C., Jahanshahi, M. R., Wu, R. T., & Joffe, C. (2017). A texture-Based Video Processing Methodology Using Bayesian Data Fusion for Autonomous Crack Detection on Metallic Surfaces. *Computer-Aided Civil and Infrastructure Engineering*, 32(4), 271-287.

Chen, J. G., Davis, A., Wadhwa, N., Durand, F., Freeman, W. T., & Büyüköztürk, O. (2016). Video Camera–Based Vibration Measurement for Civil Infrastructure Applications. *Journal of Infrastructure Systems*, 12 (3), B4016013.

Chen, J. G., Wadhwa, N., Cha, Y. J., Durand, F., Freeman, W. T., & Buyukozturk, O. (2015). Modal identification of simple structures with high-speed video using motion magnification. *Journal of Sound and Vibration*, 345, 58-71.

Chondros, T. G., Dimarogonas, A. D., & Yao, J. (2001). Vibration of a beam with a breathing crack. *Journal of Sound and vibration*, 239 (1), 57-67.

Coifman, B., Beymer, D., McLauchlan, P., & Malik, J. (1998). A real-time computer vision system for vehicle tracking and traffic surveillance. *Transportation Research Part C: Emerging Technologies*, 6(4), 271-288.

Connor, R. J., & Fisher, J. W. (2006). Identifying effective and ineffective retrofits for distortion fatigue cracking in steel bridges using field instrumentation. *Journal of Bridge Engineering*, 11(6), 745-752.

Dai H, Thostenson ET, and Schumacher T. (2015) Processing and Characterization of a Novel Distributed Strain Sensor Using Carbon Nanotube-Based Nonwoven Composites. *Sensors*. 15 17728-47

Dey, P. P., Chandra, S., and Gangopadhaya, S. (2006). Speed distribution curves under mixed traffic conditions. *Journal of Transportation Engineering*, 132(6), 475-481.

Dias-da-Costa, D., Valença, J., Júlio, E., & Araújo, H. (2016). Crack propagation monitoring using an image deformation approach. *Structural Control and Health Monitoring*.

Downey, A., Laflamme, S., & Ubertini, F. (2016). Reconstruction of in-plane strain maps using hybrid dense sensor network composed of sensing skin. *Measurement Science and Technology*, 27(12), 124016.

El-Hakim, S. F., Beraldin, J. A., Picard, M., & Godin, G. (2004). Detailed 3D reconstruction of large-scale heritage sites with integrated techniques. *IEEE Computer Graphics and Applications*, 24(3), 21-29.

Escobar-Wolf, R., Oommen, T., Brooks, C. N., Dobson, R. J., & Ahlborn, T. M. (2017). Unmanned Aerial Vehicle (UAV)-Based Assessment of Concrete Bridge Deck Delamination Using Thermal and Visible Camera Sensors: A Preliminary Analysis. *Research in Nondestructive Evaluation*, 1-16.

Federal Highway Administration (FHWA). (2004). National bridge inspection standards, *Federal Register*, 69 (239).

Feng, D., & Feng, M. Q. (2017). Experimental validation of cost-effective vision-based structural health monitoring. *Mechanical Systems and Signal Processing*, 88, 199-211.

Feng, D., & Feng, M. Q. (2016). Vision-based multipoint displacement measurement for structural health monitoring. *Structural Control and Health Monitoring*, 23(5), 876-890.

Feng, M. Q., Fukuda, Y., Feng, D., & Mizuta, M. (2015). Nontarget vision sensor for remote measurement of bridge dynamic response. *Journal of Bridge Engineering*, 20(12), 04015023.

Fisher, JW (1984) Fatigue and Fracture in Steel Bridges. Case studies (Hoboken, NJ: Wiley-Interscience)

Ghahremani, K., Sadhu, A., Walbridge, S., & Narasimhan, S. (2013). Fatigue testing and structural health monitoring of retrofitted web stiffeners on steel highway bridges. *Transportation Research Record: Journal of the Transportation Research Board*, (2360), 27-35.

Glisic, B, and Inaudi, D. (2011). Development of method for in-service crack detection based on distributed fiber optic sensors. *Structural Health Monitoring*. 1475921711414233.

Glišić, B., Yao, Y., Tung, S. T. E., Wagner, S., Sturm, J. C., & Verma, N. (2016). Strain Sensing Sheets for Structural Health Monitoring Based on Large-Area Electronics and Integrated Circuits. *Proceedings of the IEEE,* 104(8), 1513-1528.

Gupta, S., & Ray, A. (2007). Real-time fatigue life estimation in mechanical structures. *Measurement Science and Technology*, 18(7), 1947.

Haghani, R., Al-Emrani, M., & Heshmati, M. (2012). Fatigue-prone details in steel bridges. *Buildings*, 2(4), 456-476.

Haight F.A. and Mosher W.W. (1962). A practical method of improving the accuracy of vehicular speed distribution measurements, HRR 341, *Highway Research Board*, Washington, D.C., pp. 92116

Harris, C., & Stephens, M. (1988, August). A combined corner and edge detector. *In Alvey vision conference* 15 (50), pp. 10-5244.

Hartman, A., Hassel, H., Adams, C., Bennett, C., Matamoros, A., & Rolfe, S. (2010). Effects of cross-frame placement and skew on distortion-induced fatigue in steel bridges. *Transportation Research Record: Journal of the Transportation Research Board*, (2200), 62-68.

Hassel, H. L., Bennett, C. R., Matamoros, A. B., & Rolfe, S. T. (2012). Parametric analysis of cross-frame layout on distortion-induced fatigue in skewed steel bridges. *Journal of Bridge Engineering*, 18(7), 601-611.

Holusha, J. and Chang, K. (2007). Engineers see dangers in aging infrastructure. New York Times, August 2, 2007. http://www.nytimes.com/2007/08/02/us/01cnd-engineer.html

Hutt, T., & Cawley, P. (2009). Feasibility of digital image correlation for detection of cracks at fastener holes. *NDT & E International*, 42(2), 141-149.

Ihn, JB, and Chang, FK. (2004). Detection and monitoring of hidden fatigue crack growth using a built-in piezoelectric sensor/actuator network: I. Diagnostics. *Smart materials and structures*. 13: 609

Iyer, S., & Sinha, S. K. (2006). Segmentation of pipe images for crack detection in buried sewers. *Computer-Aided Civil and Infrastructure Engineering*, 21(6), 395-410.

Jahanshahi, M. R., & Masri, S. F. (2012). Adaptive vision-based crack detection using 3D scene reconstruction for condition assessment of structures. *Automation in Construction*, 22, 567-576.

Jajich, D., & Schultz, A. E. (2003). Measurement and analysis of distortion-induced fatigue in multigirder steel bridges. *Journal of Bridge Engineering*, 8(2), 84-91.

Jeong, J. H., Xu, J., Jo, H., Li, J., Kong, X., Collins, W., Bennett, C. & Laflamme, S. (2018, March). Capacitance-based wireless strain sensor development. *In Sensors and Smart Structures Technologies for Civil, Mechanical, and Aerospace Systems 2018* (Vol. 10598, p. 105980S). International Society for Optics and Photonics.

Kalal, Z., Mikolajczyk, K., & Matas, J. (2010, August). Forward-backward error: Automatic detection of tracking failures. *In Pattern recognition (ICPR), 2010 20th international* conference on (pp. 2756-2759). IEEE.

Kang, I., Schulz, M. J., Kim, J. H., Shanov, V., & Shi, D. (2006). A carbon nanotube strain sensor for structural health monitoring. *Smart materials and structures*, 15(3), 737.

Kharroub, S., Laflamme, S., Song, C., Qiao, D., Phares, B., and Li, J., (2015) Smart sensing skin for detection and localization of fatigue cracks *Smart Materials and Structures*. 24 065004

Khuc, T., & Catbas, F. N. (2017). Computer vision-based displacement and vibration monitoring without using physical target on structures. *Structure and Infrastructure Engineering*, 13(4), 505-516.

Khuc, T., & Catbas, F. N. (2017). Structural Identification Using Computer Vision–Based Bridge Health Monitoring. *Journal of Structural Engineering*, , 144(2), 04017202.

Kim, H., Lee, J., Ahn, E., Cho, S., Shin, M., & Sim, S. H. (2017). Concrete Crack Identification Using a UAV Incorporating Hybrid Image Processing. *Sensors*, 17(9), 2052.

Kong X, Shi T, Cheng S (2014). A numerical simulation method for steel structure collapsing under rare earthquake base on the material damage and failure law. *China Civil Engineering Journal*. 47 38-44

Kong, X., & Li, J. (2018a). Image registration-based bolt loosening detection of steel joints. *Sensors*, 18(4), 1000.

Kong, X., & Li, J. (2018b). Vision-Based Fatigue Crack Detection of Steel Structures Using Video Feature Tracking. *Computer-Aided Civil and Infrastructure Engineering*. In press.

Kong, X., & Li, J. (2018c, March). Automated fatigue crack identification through motion tracking in a video stream. *In Sensors and Smart Structures Technologies for Civil, Mechanical, and Aerospace Systems 2018* (Vol. 10598, p. 105980V). International Society for Optics and Photonics.

Kong, X., & Li, J. (2018d, March). An image-based feature tracking approach for bolt loosening detection in steel connections. *In Sensors and Smart Structures Technologies for Civil, Mechanical, and Aerospace Systems 2018* (Vol. 10598, p. 105980U). International Society for Optics and Photonics.

Kong, X., Li, J., Collins, W., Bennett, C., Jo, H., Jeong, J. H., & Laflamme, S. (2018e, March). Dense capacitive sensor array for monitoring distortion-induced fatigue cracks in steel bridges. *In Sensors and Smart Structures Technologies for Civil, Mechanical, and Aerospace Systems 2018* (Vol. 10598, p. 105980Q). International Society for Optics and Photonics.

Kong, X., Li, J., Bennett, C, Collins, W., Laflamme, S. and Jo, H. (2018f). Thin-film sensor for fatigue crack sensing in steel bridges under varying crack propagation rate and random traffic load, *ASCE Journal of Aerospace Engineering*, Accepted.

Kong, X., Taher, S. and Li, J. (2018g). UAV-based Fatigue Damage Sensing for Steel Bridges through Image Geometric Transformation. *The 7th World Conference on Structural Control and Monitoring (7WCSCM)*, Qingdao, China.

Kong, X., Li, J., Bennett, C., Collins, W., & Laflamme, S. (2016a). Numerical simulation and experimental validation of a large-area capacitive strain sensor for fatigue crack monitoring. *Measurement Science and Technology*, 27(12), 124009.

Kong, X., Li, J., Bennett, C., Collins, W., and Laflamme, S., (2016b). Model calibration for a soft elastomeric capacitor sensor considering slippage under fatigue cracks. *SPIE Smart Structures and Materials + Nondestructive Evaluation and Health Monitoring* International Society for Optics and Photonics pp.98032P

Kong, X., Li, J., Collins, W., Bennett, C., Laflamme, S., & Jo, H. (2017a). A large-area strain sensing technology for monitoring fatigue cracks in steel bridges. *Smart Materials and Structures*, 26(8).

Kong, X., Li, J., Collins, W., Bennett, C., Laflamme, S., & Jo, H. (2017b, April). A robust signal processing method for quantitative high-cycle fatigue crack monitoring using soft elastomeric capacitor sensors. *In Sensors and Smart Structures Technologies for Civil, Mechanical, and Aerospace Systems 2017* (Vol. 10168, p. 101680B). International Society for Optics and Photonics.

Kong, X., Li, J., Laflamme, S., and Bennett, C. (2015a). Fatigue Crack Monitoring using Large-area, Flexible Capacitive Strain Sensors. *The 6th International Conference on Advances in Experimental Structural Engineering (6AESE) and 11th International Workshop on Advanced Smart Materials and Smart Structures Technology (11ANCRiSST).* University of Illinois at Urbana-Champaign

Kong, X., Li, J., Laflamme, S., Bennett, C., & Matamoros, A. (2015b, April). Characterization of a soft elastomeric capacitive strain sensor for fatigue crack monitoring. *In SPIE Smart Structures and Materials+ Nondestructive Evaluation and Health Monitoring (pp. 94353I-94353I).* International Society for Optics and Photonics.

Laflamme S, Kollosche M, Connor JJ, and Kofod G (2012). Robust flexible capacitive surface sensor for structural health monitoring applications *Journal of Engineering Mechanics*. 139 879-85.

Laflamme S, Saleem HS, Vasan BK, Geiger RL, Chen D, Kessler MR, and Rajan K (2013). Soft elastomeric capacitor network for strain sensing over large surfaces *IEEE/ASME Transactions on Mechatronics.* 18 1647-54

Laflamme S, Ubertini F, Saleem H, D'Alessandro A, Downey A, Ceylan H, and Materazzi AL (2014). Dynamic characterization of a soft elastomeric capacitor for structural health monitoring *Journal of Structural Engineering*. 141 04014186

Laflamme, S., Kollosche, M., Connor, J. J., & Kofod, G. (2012). Robust flexible capacitive surface sensor for structural health monitoring applications. *Journal of Engineering Mechanics*, 139(7), 879-885.

Leutenegger, S., Chli, M., & Siegwart, R. Y. (November 2011). BRISK: Binary robust invariant scalable keypoints. In Computer Vision (ICCV), *2011 IEEE International Conference* on (pp. 2548-2555). IEEE.

Loh KJ, Kim J, Lynch JP, Kam NW, and Kotov NA (2007) Multifunctional layer-by-layer carbon nanotube–polyelectrolyte thin films for strain and corrosion sensing *Smart Materials and Structures*. 16 429.

Lowe, D. G. (2004). Distinctive image features from scale-invariant keypoints. *International Journal of Computer Vision*, 60(2), 91-110.

Lu, Q., Harvey, J., Le, T., Lea, J., Quinley, R., Redo, D., and Avis, J. (2002). Truck traffic analysis using weigh-in-motion (WIM) data in California. Report produced under the auspices of the California Partnered Pavement Research Program for the California *Department of Transportation Pavement Research Center, Institute of Transportation Studies*, University of California, Berkeley.

Lucas, Bruce D. and Takeo Kanade. (April, 1981). An Iterative Image Registration Technique with an Application to Stereo Vision, *Proceedings of the 7th International Joint Conference on Artificial Intelligence*, pp. 674–679.

Man, S. H., & Chang, C. C. (2016). Design and performance tests of a LED‐based two‐dimensional wireless crack propagation sensor. *Structural Control and Health Monitoring*, 23(4), 668-683.

Marsh, K. J., Smith, R. A., & Ritchie, R. O. (1991). Fatigue crack measurement: techniques and applications. *Engineering Materials Advisory Services Ltd*..

MATLAB and Computer Vision Toolbox Release 2016a, The MathWorks, Inc., Natick, Massachusetts, United States.

MATLAB and Computer Vision Toolbox Release 2017b; The MathWorks, Inc.: Natick, MA, USA.

McLean, J. R. (1978) "Observed speed distributions and rural road traffic operations". *Proceeding of 9th Australian Road Research Board Conference,* Australian Road Research Board, Vermont South, Victoria, Australia, 235–244

Mohammad I, and Huang H (2010). Monitoring fatigue crack growth and opening using antenna sensors *Smart Materials and Structures*. 19 055023

Mokhtari, S., Wu, L., & Yun, H. B. (2017). Statistical Selection and Interpretation of Imagery Features for Computer Vision-Based Pavement Crack–Detection Systems. *Journal of Performance of Constructed* Facilities, 31(5), 04017054.

Movahhedy M, Gadala MS, Altintas Y (2000). Simulation of the orthogonal metal cutting process using an arbitrary Lagrangian–Eulerian finite-element method *Journal of Materials Processing Technology*. 103 267-75

Newman, J. J. (1984). A crack opening stress equation for fatigue crack growth. *International Journal of Fracture*, 24(4), R131-R135.

Nishikawa, T., Yoshida, J., Sugiyama, T., & Fujino, Y. (2012). Concrete crack detection by multiple sequential image filtering. *Computer-Aided Civil and Infrastructure Engineering*, 27(1), 29-47.

Oliveira, F. P., & Tavares, J. M. R. (2014). Medical image registration: a review. *Computer Methods in Biomechanics And Biomedical Engineering*, 17(2), 73-93.

Ong, W. H., Chiu, W. K., Kuen, T., & Kodikara, J. (2017). Determination of the State of Strain of Large Floating Covers Using Unmanned Aerial Vehicle (UAV) Aided Photogrammetry. *Sensors*, 17(8), 1731.

Paris, S., Hasinoff, S. W., & Kautz, J. (2011). Local Laplacian filters: Edge-aware image processing with a Laplacian pyramid. *ACM Trans. Graph.*, 30(4), 68-1.

Park, J. W., Lee, J. J., Jung, H. J., & Myung, H. (2010). Vision-based displacement measurement method for high-rise building structures using partitioning approach. *NDT & E International*, 43(7), 642-647.

Patel, T. H., & Darpe, A. K. (2008). Influence of crack breathing model on nonlinear dynamics of a cracked rotor. *Journal of Sound and Vibration*, 311(3-5), 953-972.

Phares, B. M., Rolander, D. D., Graybeal, B. A., & Washer, G. A. (2001). Reliability of visual bridge inspection. *Public Roads*, 64(5).

POLÁK, J., & ZEZULKA, P. (2005). Short crack growth and fatigue life in austenitic-ferritic duplex stainless steel. *Fatigue & Fracture of Engineering Materials & Structures*, 28(10), 923-935.

Roberts, T., & Talebzadeh, M. (2003). Acoustic emission monitoring of fatigue crack propagation. *Journal of Constructional Steel Research*, 59(6), 695-712.

Rosten, E., & Drummond, T. (2005, October). Fusing points and lines for high performance tracking. *In Tenth IEEE International Conference on Computer Vision (ICCV'05)* Volume 1 (Vol. 2, pp. 1508-1515). IEEE.

Rupil, J., Roux, S., Hild, F., & Vincent, L. (2011). Fatigue microcrack detection with digital image correlation. *The Journal of Strain Analysis for Engineering Design*, 46(6), 492-509.

Saleem H, Downey A, Laflamme S, Kollosche M, and Ubertini F. (2015). Investigation of Dynamic Properties of a Novel Capacitive-based Sensing Skin for Nondestructive Testing *Materials Evaluation*. 73 1384-91

Saxena, A., & Hudak, S. J. (1978). Review and extension of compliance information for common crack growth specimens. *International Journal of Fracture*, 14(5), 453-468.

Shi, J. (1994, June). Good features to track. In Computer Vision and Pattern Recognition, 1994. Proceedings *CVPR'94., 1994 IEEE Computer Society Conference* on (pp. 593-600). IEEE.

Simonsen BC and Törnqvist R (2004). Experimental and numerical modelling of ductile crack propagation in large-scale shell structures *Marine Structures*. 17 1-27

Simulia DS 2013 ABAQUS 6.13 User's Manual Dassault Systems Providence RI

Sinha, S. N., Frahm, J. M., Pollefeys, M., & Genc, Y. (2006, May). GPU-based video feature tracking and matching. *In EDGE, Workshop on Edge Computing Using New Commodity* Architectures (Vol. 278, p. 4321).

Sobel, I., & Feldman, G. (1968). A 3x3 isotropic gradient operator for image processing. A talk at the Stanford Artificial Project in, 271-272.

Song JH, Wang H, Belytschko T 2008 A comparative study on finite element methods for dynamic fracture *Computational Mechanics*. 42 239-50

Staszewski, W. J., Lee, B. C., & Traynor, R. (2007). Fatigue crack detection in metallic structures with Lamb waves and 3D laser vibrometry. *Measurement Science and Technology*, 18(3), 727.

Sutton, M. A., Zhao, W., McNeill, S. R., Helm, J. D., Piascik, R. S., & Riddell, W. T. (1999). Local crack closure measurements: Development of a measurement system using computer vision and a far-field microscope. *In Advances in fatigue crack closure measurement and analysis: second volume*. ASTM International.

Ta, D. N., Chen, W. C., Gelfand, N., & Pulli, K. (2009, June). Surftrac: Efficient tracking and continuous object recognition using local feature descriptors. In Computer Vision and Pattern Recognition, 2009. *CVPR 2009. IEEE Conference* on (pp. 2937-2944). IEEE.

Tareen, S. A. K., & Saleem, Z. (2018, March). A comparative analysis of SIFT, SURF, KAZE, AKAZE, ORB, and BRISK. *In Computing, Mathematics and Engineering Technologies (iCoMET), 2018 International Conference* on (pp. 1-10). IEEE.

Thirion, J. P. (1998). Image matching as a diffusion process: an analogy with Maxwell's demons. *Medical Image Analysis*, 2(3), 243-260.

Tikka J, Hedman R, and Silijander A (2003). Strain gauge capabilities in crack detection *4th International Workshop on Structural Health Monit*oring. 15-17

Tomasi, Carlo and Takeo Kanade. (April, 1991). Detection and Tracking of Point Features, Computer Science Department, Carnegie Mellon University,

Torr, P. H., & Zisserman, A. (2000) MLESAC: A new robust estimator with application to estimating image geometry. *Computer Vision and Image Understanding*, 78(1), 138-156.

Ubertini, F., Laflamme, S., Ceylan, H., Materazzi, A. L., Cerni, G., Saleem, H. & Corradini, A. (2014). Novel nanocomposite technologies for dynamic monitoring of structures: a comparison between cement-based embeddable and soft elastomeric surface sensors. *Smart Materials and Structures*, 23(4), 045023.

Vanlanduit, S., Vanherzeele, J., Longo, R., & Guillaume, P. (2009). A digital image correlation method for fatigue test experiments. *Optics and Lasers in Engineering*, 47(3), 371-378.

Vercauteren, T., Pennec, X., Perchant, A., & Ayache, N. (2009). Diffeomorphic demons: Efficient non-parametric image registration. *NeuroImage*, 45(1), S61-S72.

Vrouwenvelder, A. C. W. M. and Waarts, P. H. (1993). "Traffic loads on bridges". *Structural Engineering International*, 3(3), 169-177.

Wahbeh, A. M., Caffrey, J. P., & Masri, S. F. (2003). A vision-based approach for the direct measurement of displacements in vibrating systems. *Smart Materials and Structures*, 12(5), 785.

Xu, Y., & Brownjohn, J. M. (2017). Review of machine-vision based methodologies for displacement measurement in civil structures. *Journal of Civil Structural Health Monitoring*, 1-20.

Xu, Y., Bao, Y., Chen, J., Zuo, W., & Li, H. (2018). Surface fatigue crack identification in steel box girder of bridges by a deep fusion convolutional neural network based on consumer-grade camera images. *Structural Health Monitoring*, 1475921718764873.

Xu, Y., Li, S., Zhang, D., Jin, Y., Zhang, F., Li, N., & Li, H. (2017). Identification framework for cracks on a steel structure surface by a restricted Boltzmann machines algorithm based on consumer-grade camera images. *Structural Control and Health Monitoring*.

Yamaguchi, T., Nakamura, S., Saegusa, R., & Hashimoto, S. (2008). Image-Based Crack Detection for Real Concrete Surfaces. *IEEJ Transactions on Electrical and Electronic Engineering*, 3(1), 128-135.

Yang, Y., Dorn, C., Mancini, T., Talken, Z., Kenyon, G., Farrar, C., & Mascareñas, D. (2017). Blind identification of full-field vibration modes from video measurements with phase-based video motion magnification. *Mechanical Systems and Signal Processing*, 85, 567-590.

Yao Y, Tung ST, and Glisic B (2014). Crack detection and characterization techniques—An overview *Structural Control and Health Monitoring*. 21 1387-413

Yeum, C. M., & Dyke, S. J. (2015). Vision‐Based Automated Crack Detection for Bridge Inspection. *Computer‐Aided Civil and Infrastructure Engineering*, 30(10), 759-770.

Yeum, C. M., Dyke, S. J., & Ramirez, J. (2018). Visual data classification in post-event building reconnaissance. *Engineering Structures*, 155, 16-24.

Yi X, Cho C, Cooper J, Wang Y, Tentzeris MM, & Leon RT (2013). Passive wireless antenna sensor for strain and crack sensing - electromagnetic modeling, simulation, and testing *Smart Materials and Structures*. 22 085009

Yoon, H., Elanwar, H., Choi, H., Golparvar‐Fard, M., & Spencer, B. F. (2016). Target‐free approach for vision‐based structural system identification using consumer‐grade cameras. *Structural Control and Health Monitoring*.

Yoon, H., Hoskere, V., Park, J. W., & Spencer, B. F. (2017). Cross-correlation-based structural system identification using unmanned aerial vehicles. *Sensors*, 17(9), 2075.

Yu, D., Bennett, C., & Matamoros, (2017). A. Retrofitting Distortion-Induced Fatigue in Skewed Girders to Cross-Frame Connections. *In Structures Congress 2017*(pp. 149-161).

Yu, J., Ziehl, P., Matta, F., & Pollock, A. (2013). Acoustic emission detection of fatigue damage in cruciform welded joints. *Journal of Constructional Steel Research*, 86, 85-91.

Zhang, A., Wang, K.C., Li, B., Yang, E., Dai, X., Peng, Y., Fei, Y., Liu, Y., Li, J.Q. and Chen, C., (2017). Automated Pixel‐Level Pavement Crack Detection on 3D Asphalt Surfaces Using a Deep‐Learning Network. *Computer‐Aided Civil and Infrastructure Engineering*..

Zhao Z, and Haldar A. (1996). Bridge fatigue damage evaluation and updating using non-destructive inspections. *Engineering fracture mechanics*. 53(5), 775-88.

Zhao, Y., & Roddis, W. M. K. (2004). Fatigue Prone Steel Bridge Details: Investigation and Recommended Repairs, K-TRAN: KU-99-2, Final Report. Kansas Department of Transportation, Topeka, KS.

Zhu, L., Fu, Y., Chow, R., Spencer, B. F., Park, J. W., & Mechitov, K. (2018). Development of a High-Sensitivity Wireless Accelerometer for Structural Health Monitoring. *Sensors*, 18(1), 262.

Zitova, B., & Flusser, J. (2003). Image registration methods: a survey. *Image and vision computing*, 21(11), 977-1000.

Zoghlami, I., Faugeras, O., & Deriche, R. (1997, June). Using geometric corners to build a 2D mosaic from a set of images. In Computer Vision and Pattern Recognition, 1997. Proceedings., *1997 IEEE Computer Society Conference* on (pp. 420-425). IEEE.